Universitat Autònoma de Barcelona

Electrolytes And Interfaces In Calcium And Magnesium Rechargeable Batteries

Juan David Forero Saboya

Electrolytes And Interfaces In Calcium And Magnesium Rechargeable Batteries

Juan David Forero Saboya

Barcelona, 2022

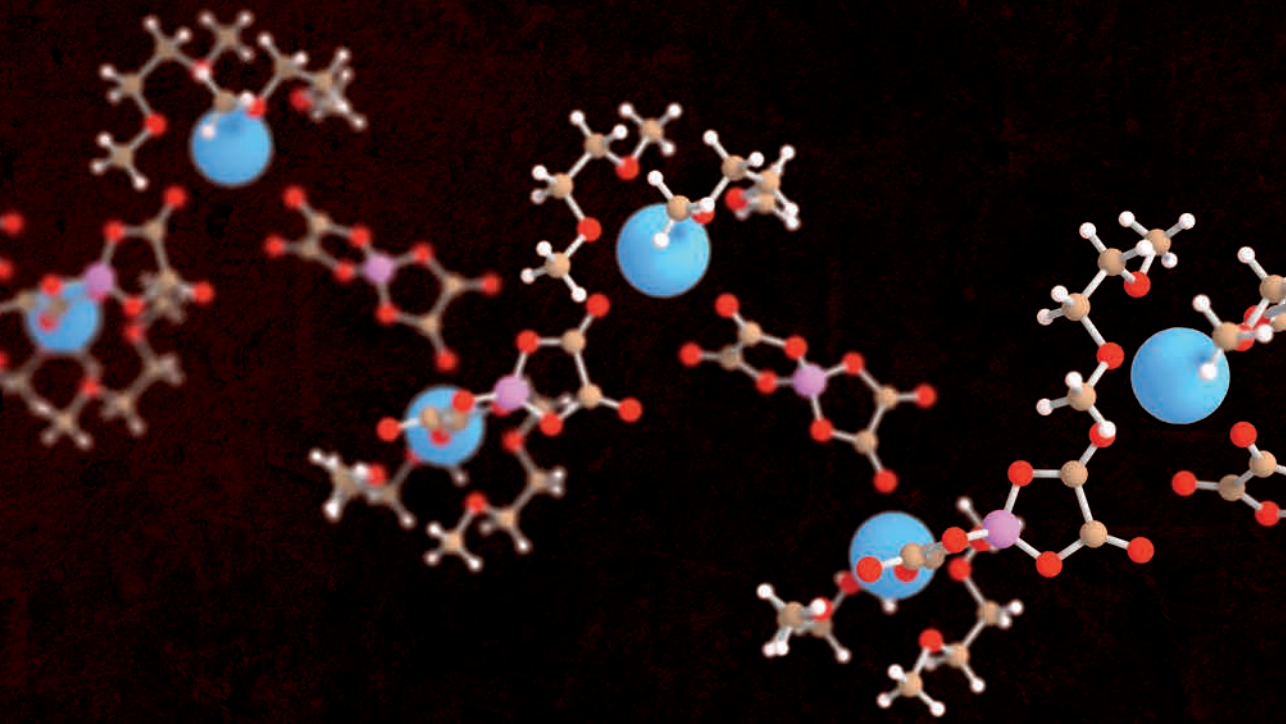

Electrolytes and Interfaces in Calcium and Magnesium Rechargeable Batteries
Juan D. Forero-Saboya

PhD Thesis 2022
Institut de Ciència de Materials de Barcelona (ICMAB-CSIC)
Universitat Autònoma de Barcelona
08193 Bellaterra - Barcelona
Spain

Cover: Crystal structure of solvated $Ca(BOB)_2(DME)_2$.
See more on Figure 2.13

Typeset in LaTeX
Printed by Llar Digital
12001 Castellón, Spain 2022

Universitat Autònoma de Barcelona

UNIVERSITAT AUTÒNOMA DE BARCELONA

FACULTAT DE CIÈNCIES

PROGRAMA DE DOCTORAT EN CIÈNCIA DE MATERIALS

PhD thesis

ELECTROLYTES AND INTERFACES IN CALCIUM AND MAGNESIUM RECHARGEABLE BATTERIES

Juan David Forero Saboya

Barcelona, Espanya 2022

UNIVERSITAT AUTÒNOMA DE BARCELONA

FACULTAT DE CIÈNCIES

Programa de Doctorat en Ciència de Materials

ELECTROLYTES AND INTERFACES IN CALCIUM AND MAGNESIUM RECHARGEABLE BATTERIES

Memòria de tesi presentada per Juan David Forero Saboya per optar al títol de doctor per la Universitat Autònoma de Barcelona. El treball presentat s'ha dut a terme al Institut de Ciència de Materials de Barcelona (ICMAB-CSIC)

Director
Alexandre Ponrouch
Institut de Ciència de Materials de Barcelona (ICMAB-CSIC)

Doctorand
Juan David Forero Saboya
Institut de Ciència de Materials de Barcelona (ICMAB-CSIC)

Director
Patrik Johansson
Chalmers Tekniska Högskola

Tutor
José Antonio Ayllon Esteve
Universitat Autònoma de Barcelona

Barcelona, Espanya 2022

Electrolytes and Interfaces in Calcium and Magnesium Rechargeable Batteries

Juan David Forero Saboya
Universitat Autònoma de Barcelona
Institut de Ciència de Materials de Barcelona (ICMAB-CSIC)

Abstract

The development of next-generation batteries (post Li) will have a great impact in the upcoming years of transition from fossil fuels to renewable sources of energy. Among the many next-generation battery concepts, the ones based on divalent metals as negative electrodes stand out (particularly Ca and Mg), given their combination of low standard redox potential and high natural abundance. Development of Ca and Mg metal batteries have been historically hampered, as only a few organic electrolytes allow reversible electroplating/stripping of the metal, which is required for a continuous and stable operation of the metallic negative electrode.

In this thesis, some efforts on the optimization of organic electrolytes for Ca metal plating are presented, with parallels to Mg application. The electrolyte formulation, which is based on a mixture of salt, solvent, and additives, is studied in this work from three complementary points of view: preparation of calcium salts, physicochemical properties of the obtained electrolytes, and evaluation of their electrochemical performance, which includes also the possible reductive decomposition of the electrolyte and the formation of a passivation layer on the electrode. Although they are separated in different chapters, these are not isolated parameters, and their interactions are discussed across this document. Particularly, the cation solvation appears as a physical parameter of critical importance from the three points of view: being influenced by salt and solvent choice, it is responsible for the macroscopic properties (as ionic conductivity and ionicity), and affects, in turn, the dynamics of electroplating, and the nature of the passivation layer formed. Therefore, some insights in the cation solvation-shell manipulation are presented as a route to optimize the operation of a Ca metal as the negative electrode.

Additionally, a study on the passivation layers formed on metallic calcium electrodes is presented, as function of the electrolyte formulation. The borate-based passivation layer, which is produced *in situ* by anion or additive decomposition, was shown to promote calcium plating in contrast to a carbonate-based passivation layer, which appeared to be fully blocking for Ca^{2+} cations.

Further studies will determine a more precise composition of the borate-based layer and will pave the way for artificially generated passivation layers to be used in future calcium batteries.

Electrolitos e Interfases para Baterias Recargables de Calcio y Magnesio
Juan David Forero Saboya
Universitat Autònoma de Barcelona
Institut de Ciència de Materials de Barcelona (ICMAB-CSIC)

Resumen

El desarrollo de una nueva generación de baterías (post Li) tendrá, en los próximos años, un impacto importante en la transición de combustibles fósiles a nuevas fuentes de energía renovables. De los diferentes conceptos de baterías de próxima generación, destacan los que utilizan metales divalentes como electrodos negativos (especialmente Ca y Mg), dada su combinación de bajo potencial estándar de reducción y su gran abundancia. El desarrollo de baterías de Ca y Mg metal se ha visto históricamente obstaculizado debido a la limitada opción de electrolitos orgánicos que permitan la deposición y disolución reversible del metal, una condición necesaria para un funcionamiento continuo y estable del electrodo metálico.

En esta tesis se presentan algunos esfuerzos en la optimización de electrolitos orgánicos para la electrodeposición de Ca, con ciertos paralelos a la aplicación en el caso de Mg. La formulación del electrolito, que se basa en una mezcla de sal, disolvente y aditivos, se estudia en este trabajo desde tres puntos de vista complementarios: la preparación de las sales de calcio, las propiedades fisicoquímicas de los electrolitos obtenidos y la evaluación de su rendimiento electroquímico, que incluye también la posible descomposición del electrolito por reducción y la formación de una capa de pasivación en el electrodo. Aunque los tres puntos de vista están separados en diferentes capítulos, no están realmente aislados, y sus interacciones se discuten a lo largo de este documento. En particular, la solvatación del catión aparece como un parámetro físico de vital importancia que afecta los tres puntos de vista: está influenciada por la sal y el disolvente, es responsable de las propiedades macroscópicas (como conductividad iónica e ionicidad), y afecta, a su vez, la dinámica de electrodeposición y a la naturaleza de la capa de pasivación formada. Por lo tanto, en esta tesis se presentan algunos detalles enfocados en la manipulación de la esfera de solvatación del catión, como una vía para optimizar el funcionamiento de un electrodo de Ca metálico.

Además, se presenta aquí un estudio sobre las capas de pasivación formadas en electrodos metálicos de calcio, en función de la formulación del electrolito. Se ha demostrado que la capa de pasivación a base de borato, que se produce

in situ por descomposición de aniones o aditivos, favorece la electrodeposición de calcio, en contraste con una capa de pasivación a base de carbonato, que parece bloquear totalmente los cationes de calcio. Estudios futuros elucidarán de manera más precisa la composición de esta capa basada en boratos, y allanarán el camino para la utilización de capas de pasivación generadas artificialmente en futuras baterías de calcio.

Acknowledgements

This project was supported financially by the European Union's Horizon 2020 research and innovation programme through the H2020-MSCA-COFUND-2016 (DOC-FAM, grant agreement Nº 754397).

Science nowadays is a collective endeavour. As the world becomes more globalized and the knowledge more specialized, collaboration between experts around the globe becomes essential to answer the modern scientific questions. This thesis is a clear example of this, and could not have been completed without the help of many people to whom I would like to express my deepest gratitude.

To Alex, thank you for receiving me in your lab and teaching me so much during these years. More than a boss, you have been a mentor, a guide, and a pole directing this research. I appreciate enormously our scientific discussions and the encouragement to pursue my scientific ideas. It has been an honour to be a part of your team.

To Patrik, you will always have my deepest admiration. Knowing that you had my back had given me the courage to keep moving and trust my own strength.

To Alex's team v.1.0: Romain and Elena, and v.2.0: Charlotte and Damien, it has been a pleasure to share lab with you. You have helped to give shape to a newly created group at the ICMAB, and in the process have imprinted on me values of teamwork and collaboration that will always remain.

To Rémi, Carine, Ibraheem, and Piero, who have contributed to this work hugely in data acquisition and analysis. Thank you for being always available to help us and to take part on this (some people would say) crazy idea of calcium batteries. To Piotr, who has also been a part of this research and with whom I had many scientific discussions that gave shape to this thesis.

In Slovenia I was a child split between two households, to the guys at Institut Jožef Stefan: Matic's and Mirela's teams, thank you for renewing my passion in chemistry, and for make me remember why I chose this path so many years ago. To the team at Kemijski inštitut: Robert, Jan, and Tjaša; thank you for hosting me and teaching me openly and without restrain everything you could. From my time in Slovenia I learn the value of cooperation, which, after

all, is the basis of scientific enterprises.

To the group at the Solid-State Chemistry department (current and past members), although I cannot mention you all, I do not forget you. My life at the ICMAB these four years have been amazing thanks to you. Long live the calçots, the "Anís del Mono" and the coffee breaks taking the sun!

To my family, who always have my back and to whom I owe everything I am. This scientific journey started thanks to you, when I was a kid and took apart every toy I got my hands on, wondering how it worked. Thank you for supporting me and encouraging this curiosity that has grown to become a Ph.D. degree.

To you, who are reading these lines. Because you, probably, have been part of my life and have helped to give shape to this thesis in one way or the other.

Infinitas gracias, thank you, graciès, merci, hvala, tack.

Agradecimientos

Este proyecto ha contado con financiación del programa de investigación e innovación Horizonte 2020 de la Unión Europea a través del programa H2020-MSCA-COFUND-2016 (DOC-FAM, acuerdo nº 754397).

La ciencia, hoy en dia, es una empresa colectiva. En un mundo cada vez mas globalizado, pero con conocimientos mas especializados, la colaboración entre expertos de distintos grupos es imprescindible para responder a las preguntas científicas modernas. Esta tesis es un ejemplo claro de ello, y no podría haberse realizado sin la ayuda de muchas personas a las que me gustaría expresar mi más profunda gratitud.

A Alex, gracias por acogerme en tu laboratorio y enseñarme tanto durante estos años. Más que un jefe, has sido un mentor, un guía y un polo en esta investigación. Aprecio enormemente nuestras conversaciones científicas y el estímulo para perseguir mis ideas. Ha sido un honor formar parte de tu equipo.

A Patrik, siempre tendrás mi más profunda admiración. Saber que me apoyas me ha dado valor para seguir adelante y confiar en mis propias

fuerzas.

Al equipo de Alex v.1.0: Romain y Elena, y v.2.0: Charlotte y Damien. Ha sido un placer compartir laboratorio con ustedes. Han contribuido a dar forma a un nuevo grupo en el ICMAB, y en el proceso, me han dado valores de trabajo en equipo y colaboración que siempre tendré conmigo.

A Rémi, Carine, Ibraheem y Piero, que han contribuido enormemente a este trabajo en la adquisición y análisis de datos. Gracias por estar siempre disponibles para ayudarnos y participar en esta (algunos dirían) loca idea de baterías de calcio. A Piotr, que también ha formado parte de esta investigación y con quien he tenido muchas conversaciones que han dado forma a las ideas de esta tesis.

En Eslovenia fuí un niño dividido entre dos hogares. A la gente del Instituto Jožef Stefan: Matic, Mirela y sus grupos, gracias por renovar mi pasión por la química y por hacerme recordar por qué elegí este camino hace tantos años. A la gente del Kemijski inštitut: Robert, Jan y Tjaša; gracias por acogerme y enseñarme abiertamente y sin recelo todo lo que han podido. De mi estancia en Eslovenia aprendí el valor de la cooperación, que, al fin y al cabo, es la base de las ciencia de hoy.

Al grupo de Química del Estado Sólido (actuales y pasados), aunque no puedo mencionarlos a todos, no los olvido. Mi vida en el ICMAB estos cuatro años ha sido increíble gracias a ustedes. ¡Vivan los calçots, el "Anís del Mono" y los cafés en el solet!

A mi familia, que siempre me ha apoyado y a la que debo todo lo que soy. Este viaje comenzó gracias a ustedes, cuando era pequeño y desarmaba todos los juguetes que caían en mis manos, preguntándome cómo funcionaban. Gracias por apoyarme y cultivar esa curiosidad, que ha crecido hasta convertirse en un título de doctor.

A ti, que estás leyendo estas líneas, porque probablemente has formado parte de mi vida y has ayudado a dar forma a esta tesis, de una manera u otra.

Infinitas gracias, thank you, graciès, merci, hvala, tack.

Juan David Forero Saboya, Barcelona, March 2022

Contents

List of Figures

List of Tables

Acronyms and Symbols

Acronyms

aHF	anhydrous hydrogen fluoride
BOB	*bis*(oxalate)borate
CE	Counter electrode
CIP	contact ion pair
DE	diethylether
DMC	Dimethylcarbonate
DME	Dimethoxyethane; monoglyme
DMF	N,N-dimethylformamide
EC	Ethylenecarbonate
EELS	Electron energy loss spectroscopy
EIS	Electrochemical impedance spectroscopy
ESI	Electrospray Ionization
ESW	Electrochemical stability window
Fc	Ferrocene
FEC	Fluoroethylene carbonate
FEP	Fluorinated ethylene propylene
FOD	6,6,7,7,8,8,8,-heptafluoro-2,2-dimethyl-3,5-octanedionate
FTIR	Fourier-transform Infrared Spectroscopy
γBL	*gamma*-Butyrolactone

G1	Dimethoxyethane; monoglyme
G2	Diethyleneglycol dimethylether; diglyme
G3	Triethyleneglycol dimethylether; triglyme
Hfip	Hexafluoroisopropyl
ICP-MS	Inductively Coupled Plasma - Mass Spectrometry
ICP-OES	Inductively Coupled Plasma - Atomic Emission Spectroscopy
KF	Karl-Fischer
LEDC	Lithium ethylenedicarbonate
LIB	Lithium-ion battery
LMC	Lithium methylcarbonate
LSV	Linear Sweep Voltammetry
MS	Mass Spectrometry
NMR	Nuclear Magnetic Resonance
OCV	Open circuit voltage
PC	Propylenecarbonate
PEO	poly(ethyleneoxide)
PTFE	Polytetrafluoroethylene; Teflon
RA	Raman Activity
RE	Reference electrode
RT	Room temperature
SEI	Solid-Electrolyte Interphase
SHE	Standard hydrogen electrode
SS	Stainless steel
SSIP	solvent-separated ion pair
TEM	Transmition electron microscopy
Tf	Triflate
TFAB	*tetrakis*(trifluoroacetoxy)borate
TFSI	*bis*(trifluoromethylsulfonyl)imide
TGA	Thermogravimetric Analysis

THF	Tetrahydrofuran
TMHD	2,2,6,6-tetramethyl-3,5-heptanedionate
VTF	Vogel-Tamman-Fulcher
WCA	Weakly coordinating anion
WE	Working electrode
XPS	X-ray photoelectron spectroscopy
XRD	X-ray Diffraction

Symbols

α	Fractional Walden's rule exponent
β	Volumetric expansion coefficient of a solution
δ	bond deformation vibration
ε_r	Solvent's relative permittivity or dielectric constant
η	Dynamic viscosity
η_E	Total overpotential during battery operation
λ	incident wavelength
ν	bond stretching vibration
ρ	Density
ρ^*	Density of the solution at a reference temperature T*
ρ_0	Density of the pure solvent
σ	Ionic conductivity
Λ_{eq}	equivalent molar ionic conductivity
A	Pre-exponential factor for Vogel fitting of conductivity
B	Pre-exponential factor for Vogel fitting of viscosity
C'	Fractional Walden's rule constant
c_i	salt concentration in mol L^{-1}
e_0	elemental charge

E_η	Activation energy for viscosity
E_σ	Activation energy for conductivity
F	Faraday constant
k_B	Boltzmann constant
$M_{W,i}$	molar mass of compound i
T	temperature
T^*	Reference temperature for the calculation of the density
$T_{0,\eta}$	Vogel temperature for viscosity
$T_{0,\sigma}$	Vogel temperature for conductivity
$\widetilde{V}_i$	Apparent molar volume of the salt in a solution

1

Introduction

By 2050, electricity will be the main energy carrier, according to the International Renewable Energy Agency (IRENA), increasing from a 21% share of the total energy consumption in 2018 to over 50% in 2050 [1]. This increase is the result of an intense electrification of the end-uses, such as heating and transportation, but also to the anticipated rise of new energy-demanding applications such as sensors, communication relays, and information processors, which are part of the Internet of Things (IoT) [2]. The ever-increasing presence of electricity in our daily lives, together with the transition from fossil fuels to renewable sources, constitute the core of the energy revolution that will reshape our society in the upcoming years.

Energy storage devices, particularly batteries, will play a significant role in this transformation. They are beneficial in many ways, as they, for example, can sustain and accelerate the deployment of intermittent energy sources, provide flexibility by correcting frequency and voltage changes across the electric grid, cover a temporary lack of supply, etc [3].

Since their first commercialization, lithium-ion batteries (LIBs) dominate the market of portable electronics and have been extensively employed in electric vehicles [4]. Nowadays LIBs are starting to gain terrain in stationary applications given the recent reduction of cost and the increased production capacity worldwide [5, 6]. However, LIBs rely on non-abundant materials which may produce a future increase in their price, and eventually a shortage of raw materials. Given the vast battery market emerging at the moment, and although LIBs will probably continue to be the dominant battery technology in the near future, it is important to develop next-generation batteries based on more abundant elements to power the many energy applications to come.

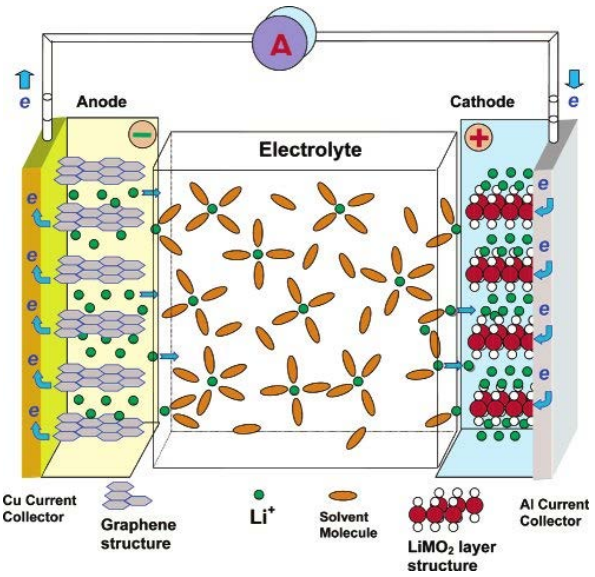

Figure 1.1: Working scheme of a LIB. In this scheme, graphite is working as negative electrode and $LiMO_2$ as positive electrode (with M a transition metal as Co or Mn) Reprinted with permission from Ref. [7]. Copyright 2004 American Chemical Society.

1.1 Principle of operation of lithium-ion batteries

Like any other battery cell, LIB cells are composed of a negative and a positive electrode (usually referred to as the anode and the cathode, respectively), electronically separated by an electrolyte. In the case of commercial LIBs, the electrodes are based on host materials in which lithium cations can be reversibly intercalated/deintercalated (Figure 1.1). Upon discharge, the lithium cations stored in the negative electrode (graphite is used in current commercial cells) are released into the electrolyte, together with the equivalent amount of electrons that are transferred to the external circuit. Simultaneously, the host material at the positive electrode, which can be CoO_2, MnO_2 or others, is reduced by the electrons coming from the external circuit and intercalates lithium cations in the crystal structure to compensate the charge.

The process of discharge is summarized, then, by the following equations, occurring at potentials E_- and E_+, respectively:

$$LiC_{6(s)} \longrightarrow C_{6(s)} + Li^+ + e^- \tag{1.1}$$

$$MO_{2(s)} + Li^+ + e^- \longrightarrow LiMO_{2(s)} \tag{1.2}$$

With MO_2 being a transition metal oxide as CoO_2 or MnO_2. Upon charge,

an opposite bias is applied to the cell, reversing the flow of electrons and so the reverse reactions occur at the electrodes.

Although the theoretical open circut voltage (OCV) between electrodes can be calculated thermodynamically from E_+ and E_-, the real output voltage during discharge is influenced by a combination of many dynamic factors arising from the movement of charged species (electrons and Li^+ cations) inside the electrode materials, across the electrolyte and through the electrode | electrolyte interfaces. A general term encompassing all these energy inefficiencies can be denoted η_E, as an overall *overpotential* of the cell, obtaining an output voltage: $E = E_+ - E_- - \eta_E$. Among others, η_E is related with the conductivity of Li^+ cations in the electrolyte, the energy barrier for cation desolvation at the electrode | electrolyte interface, etc.

Complementarily, the capacity of an electrode material is determined by the maximum amount of electrons that can be stored, and can be calculated by:

$$Q_{theo}\,[mAh\,g^{-1}] = \frac{nF}{3.6\,M_W} \tag{1.3}$$

Where n is the moles of electrons accepted or released per mol of material during charge/discharge (*e.g.* $n = 1/6$ for graphite, according to Equation 1.1), F is the Faraday constant and M_W is the molecular weight of the compound. The theoretical capacity of a graphite negative electrode is then ~372 mAh g^{-1}. However, the capacity of a battery cell is lower than the capacity of the pure materials, as some *inactive* components are necessary, like electrode binders, conductive additives, current collectors, electrolyte, etc.

The total energy density of a battery cell is calculated as the product of the output voltage of the cell by its capacity. Therefore, foreseeable strategies to improve the energy density are: *i)* use of high capacity electrode materials, *ii)* use of high redox potential positive electrode materials, and *iii)* use of low redox potential negative electrode materials.

1.2 Formation of the solid-electrolyte interphase - (SEI)

In LIBs the electrolyte is often unstable at the working potentials of the negative electrodes (typically < -2.0 V *vs.* SHE). Therefore, different components of the electrolyte are prone to decompose at the surface producing soluble, gaseous or solid products. In the ideal case, the solid decomposition

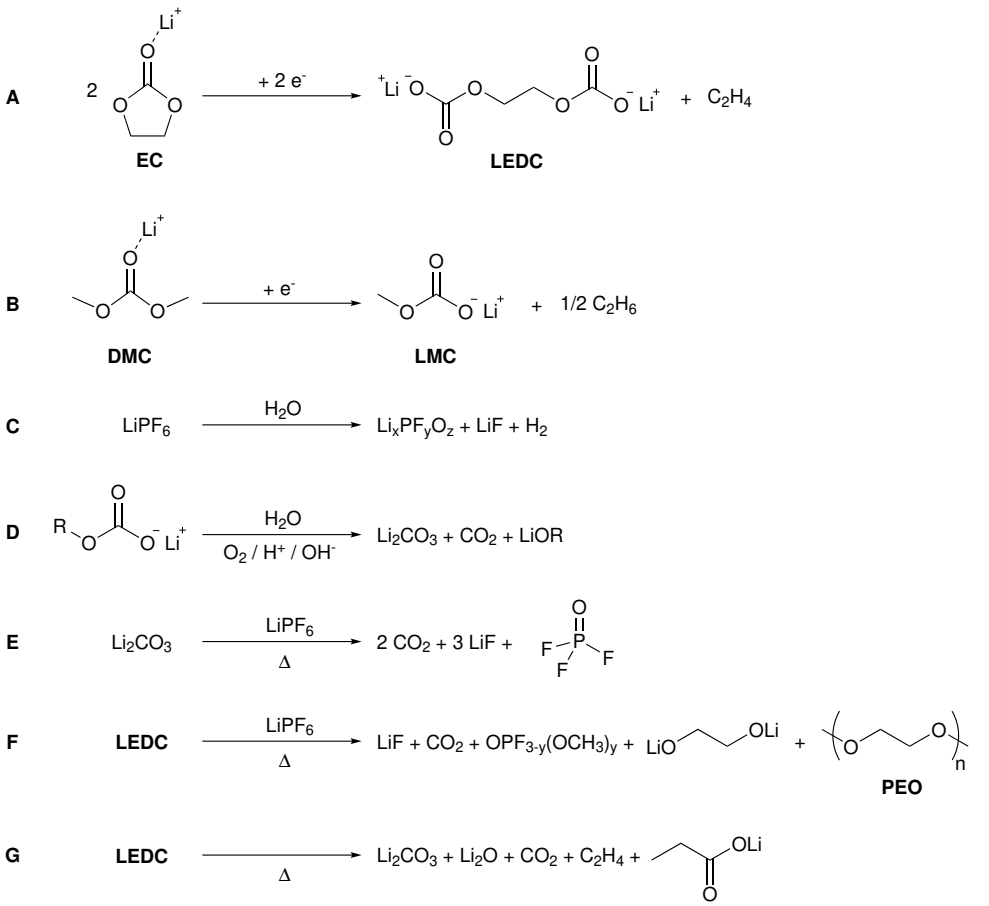

Figure 1.2: Some of the reactions occurring at the surface of the negative electrode of a LIB.

products will entirely cover the surface of the electrode forming a layer with high ionic and low electronic conductivities. This surface layer is denoted the solid-electrolyte interphase (SEI). Several models exist currently to describe the SEI formation and evolution, which additionally varies depending on the negative electrode used and the cycling conditions [8–10]. An overview of the SEI formation over graphite negative electrodes is presented here.

The benchmark electrolyte used in LIBs is composed of $LiPF_6$ dissolved in a mixture of cyclic and linear carbonate solvents, most commonly ethylene carbonate (EC), propylene carbonate (PC), dimethyl carbonate (DMC), or ethyl methyl carbonate (EMC). A combination of microscopic and spectroscopic studies have identified lithium alkyl carbonates as the main organic

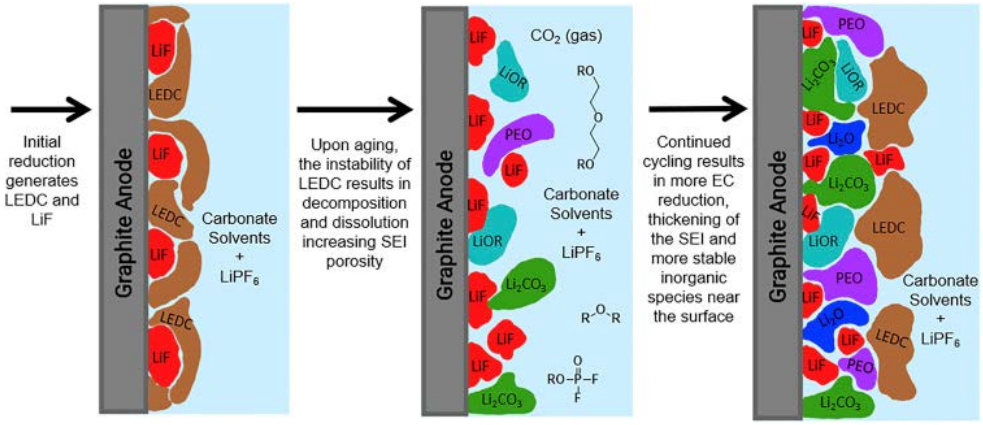

Figure 1.3: Scheme of initial growth and evolution of the SEI layer over the negative electrode of a LIB. Reprinted with permission from Ref. [15]. Copyright 2019 Elsevier Inc.

component of the SEI layer produced during the first cycles (Reactions A and B in Figure 1.2), with the evolution of the respective gases confirmed by mass spectrometry [11, 12]. In turn, the PF_6^- anion can be readily decomposed by any trace of water in the electrolyte, producing $Li_xPF_yO_z$ and LiF, the latter being the main inorganic component of the SEI during its first stage of formation (Reaction C in Figure 1.2).

The SEI layer formed at the beginning of cycling is, nonetheless, not static, and the different components evolve during time or cycling. For example, the LEDC and other alkyl carbonates can be further decomposed producing the fully inorganic lithium carbonate (Li_2CO_3), or react with the salt to produce LiF, CO_2, and poly(ethylene oxide) (Reactions D to G in Figure 1.2). During this process, the initial organic rich layer evolves into a more inorganic-rich and more porous layer. The increased porosity allows further electrolyte reaction and thus more LEDC is formed covering the surface again.

Upon time this process leaves a mixed organic-inorganic SEI, in which the outermost part is more polymeric in character and semipermeable to the solvent, while the innermost part is inorganic and only allows for bare lithium ion migration (Figure 1.3). Although the growth of the SEI is more prominent in the first cycles, it is a continuous process which increases the impedance of the electrode and contributes to the overall ageing of the battery [13, 14].

In order to improve the properties of the SEI layer, i.e. improve its ionic conductivity, decrease its thickness, or enhance its mechanical stability, several

SEI-forming additives can be included in the electrolyte formulation. The most prominent ones are vinylene carbonate (VC) and fluoroethylene carbonate (FEC). The reduction potential of both additives is higher than the original components of the electrolyte, and thus, are preferentially decomposed at the surface of the negative electrode, modifying the SEI formation pathway described before. In both cases a thinner SEI is obtained, with a lower concentration of lithium alkyl carbonates (as LEDC or LMC shown in Figure 1.2) and with the presence of some polymeric structures denoted poly(VC) and poly(FEC) [16, 17]. Additionally, the reduction of the FEC additive results in a higher content of LiF, which is regarded as a beneficial component of the lithium SEI [18].

1.3 Alternative battery chemistries - case of Ca and Mg batteries

As mentioned before, the capacity of a graphite negative electrode used currently in LIBs, is only about 372 mAh g^{-1}, given by the low amount of lithium that can be intercalated into the structure. In order to increase the capacity of the anode, other host materials are being explored. This is the case of silicon, for instance, which forms an alloy with Li. Stoichiometries such as $Li_{21}Si_5$, corresponding to a theoretical capacity of 4008 mAh g^{-1} can be achieved [19]. The use of silicon anodes in commercial cells has been hampered, however, by its huge volumetric expansion during lithiation, leading to an eventual pulverization of the silicon particles, loss of the electrical contact, and a strong capacity fade [20].

Alternatively, lithium metal can be used as negative electrode in lithium batteries, in which case they are denoted lithium metal batteries (LMBs) rather than LIBs. Given its high theoretical capacity (around 3860 mAh g^{-1}) and low redox potential, lithium metal is considered the *Holy Grail* of lithium battery negative electrodes. Compared to intercalation electrodes, the use of a lithium metal significantly changes the mechanism of charge storage. Instead of storing lithium as cations in a host crystal structure, the charge/discharge of a metal anode implies the lithium plating/stripping on each cycle: $Li_{(s)} \rightleftharpoons Li^+ + e^-$. However, Li metal is prone to uneven deposition during plating, producing dendrites (as seen in Figure 1.4) which cause some important safety hazards [21]. The Li dendrites formed upon cycling, can reach the opposite electrode and cause short-circuits, possibly initiating a thermal runaway and

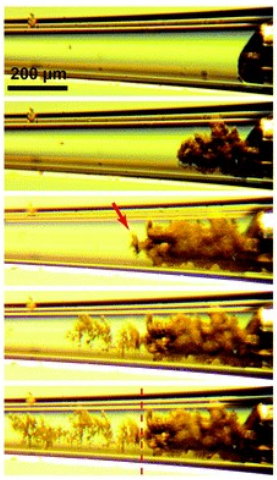

Figure 1.4: Direct observation of Li metal dendrites during electrodeposition. Figure reprinted from ref. [23] under the terms of the CC-BY-NC licence.

explosion of the cell. Although the development of solid-state electrolytes for LMBs is expected to overcome this issue, recent evidence suggest that Li dendrites can be formed even in these materials [22].

Aside from lithium, other electropositive metals could be used as anodes for secondary batteries. Some figures of merit for Na, Ca and Mg metals are presented in Figure 1.5 and compared to lithium and graphite anodes. Alkali-earth metals, like Ca or Mg, benefit from high volumetric and gravimetric capacities as they store 2 e^- per cation. Both, Ca and Mg, are much more abundant than lithium in the earth crust, which may result in a cheaper and more sustainable technology.

As a result, Mg-based batteries have been extensively studied since the 90′s, with the first proof of concept Mg-metal battery reported in the year 2000 [25]. The reported cells employ a magnesium metallic anode, coupled with $Mg_xMo_3S_4$ as cathode, and use a $Mg(AlCl_2BuEt)_2$ in tetrahydrofuran (THF) electrolyte. The cell presented a modest output voltage of about 1.0–1.3 V (compared to the nearly 4 V for commercial LIBs). Further technological development has been restricted by limitations in electrolyte stability [26] and lack of high-voltage, operational cathode materials [27]. In the case of calcium, its low redox potential, only 170 mV above Li^+/Li (and near the intercalation potential of Li^+ in graphite, Figure 1.5c) suggests that a future calcium metal battery (CMB) would be able to compete with currently commercial LIBs in terms of energy density [28]. However, as in the case of magnesium, nowadays there are only a few examples of reversible intercalation of calcium cations in inorganic hosts, limiting the options for cathode materials [29, 30].

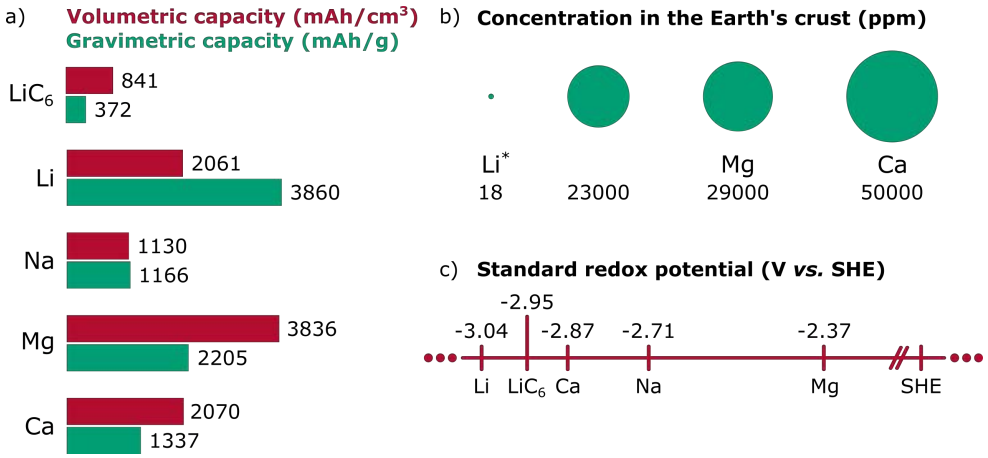

Figure 1.5: Figures of merit for different negative electrodes for batteries. a) Approximate volumetric and gravimetric capacities, **b)** relative concentration in the Earth's crust (* the area plotted for Li is 10x bigger than the real), data taken from Ref. [24], and **c)** standard redox potential of the respective M^{n+}/M couple.

The challenges associated with the development of calcium and magnesium intercalation cathodes stem from the high charge density of the cations (Figure 1.6). Given the higher charge of Ca^{2+} and Mg^{2+}, they interact more tightly with the anion frame of the crystal structure, resulting in higher migration barriers [31, 32]. This high barrier derives in a very sluggish diffusion of ions through the solid or even in the complete inactivity of the cathode [33]. Additionally, also the strong interaction between cation and solvent in the electrolyte results in slow interfacial processes at the cathode surface, and even some solvent co-intercalation has been observed [34]. Recent efforts combining computational screening of materials together with experimental evaluation of suitable candidates may provide an interesting avenue into the discovery of suitable high-voltage cathodes for divalent batteries [35].

Alternatively, organic cathodes may provide a faster charge and discharge kinetics as the transport of cations is sustained mainly in the liquid phase,

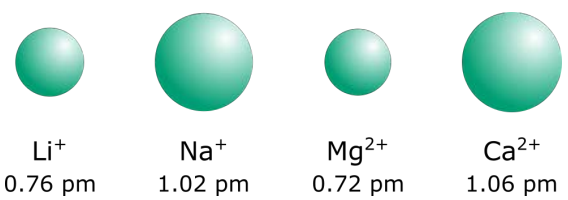

Figure 1.6: Comparative ionic radii of cations. Values obtained from Ref. [36]

and complete cation desolvation may not be necessary [37]. Mg^{2+} positive electrodes based in a heterogeneous enolization reaction ($C{=}O \rightleftharpoons C{-}O^{-}$) have been reported [38], and recently it has been shown that they can operate at very high cycling rates [39].

1.4 The negative electrode | electrolyte interface in divalent metal batteries

Not only the cathode development poses a problem in the further advance of calcium and magnesium metal batteries. As it has been pointed out before, the development of electrolytes allowing for reversible metal plating/stripping is crucial for the realization of these concepts. Here, a very brief overview of the past and current trends in electrolyte formulation for Mg and Ca batteries will be presented, with a particular interest in their impact on interfacial processes.

1.4.1 Electrolytes allowing for Mg plating

Electrodeposition of Mg from Grignard solutions was reported as early as 1927 [40]. However, practical electrolytes for use in Mg batteries were reported later, based on chloroaluminate complexes, formed by the mixture of R_xMgCl_{2-x} and R'_yAlCl_{3-y} (R, $R' = -CH_3, -CH_2CH_3$, or $-C_6H_5$) in THF or other ether solvents [41]. In these solutions, a ligand exchange occurs between the two metal centres, and a variety of chloro-magnesium cations (*e.g.* $[MgCl]^+$,$[Mg_2Cl_3]^+$) and organoaluminate anions (*e.g.* $[R_4Al]^-$,$[R_2ClAl{-}Cl{-}AlClR_2]^-$) are formed, with the exact proportion being dependent on the R groups and the Mg:Al:R:Cl ratios [42, 43]. The formulation further evolved to a rather simple mixture of $MgCl_2$ and $AlCl_3$ in the same solvent, although in this case the electrodeposition of Mg showed little efficiency in the first plating/stripping cycles (and thus required so-called conditioning cycles) [44].

Some mechanistic studies have been published dealing with the electroplating of Mg metal from this electrolyte. It is believed that the dimeric $[Mg_2(\mu\text{-}Cl)_3(THF)_6]^+$ present in the electrolyte disproportionates in the vicinity of the electrode, forming $[MgCl(THF)_5]^+$ ion pairs which adsorb to the surface (Figure 1.7). Then, conventional nucleation and growth can occur, with the cation being stripped, at least partially, of its solvation shell in order to facilitate its adsorption. The last step involves the charge transfer from the electrode, the formation of Mg^0 and the growth of the solid metal. Evidence

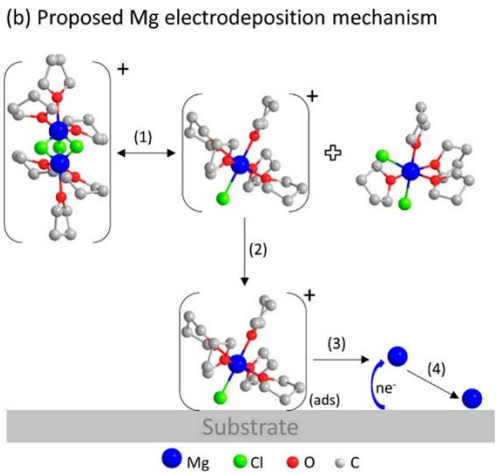

Figure 1.7: Proposed mechanism for Mg plating from a magnesium chloroaluminate solution. Reprinted with permission from Ref [46]. Copyright 2018 American Chemical Society.

of adsorption of the ion pair was gathered by X-ray absorption near-edge spectroscopy (XANES) [45], and the existence of a chemical step prior to the charge transfer agrees well with electrochemical impedance spectroscopy (EIS) and cyclic voltammetry (CV) results [46, 47].

The removal of the last few solvent molecules and the Cl^- ligand from the Mg complex have been suggested as the most energetically costly [48]. However, if the distance to the surface is short enough, electron transfer can occur before Mg−Cl dissociation. In this case, the interaction energy between anion and cation diminishes and the desolvation energy barrier is surpassed [48, 49].

Despite the good plating/stripping cyclability and the low overpotential observed for this reaction in the magnesium chloroaluminate electrolytes, the presence of Cl^- causes corrosion of the metallic casing of batteries, and the ether solvents used display very limited oxidative stability [26]. These two drawbacks notably limit the development of commercial Mg-metal batteries and push towards alternative electrolytes.

One potential electrolyte candidate is $Mg(BH_4)_2$ dissolved in THF or *1,2*-dimethoxyethane (monoglyme or G1). Similar to the case of Cl^-, the BH_4^- anion interacts strongly with Mg^{2+}, producing $[Mg\text{-}BH_4]^+$ ion pairs or $[Mg\text{-}(BH_4)_2]^0$ triplets. The formation of such ionic clusters decreases the total amount of charge carriers in the electrolyte and therefore reduces its ionic conductivity; < 0.03 mS cm^{-1} in THF [50]. Additionally, the speciation

of the Mg complexes appears to have a high impact on the kinetics of the electrodeposition reaction, as was observed by adding different amounts of $LiBH_4$ [51]. Although DFT calculations suggest that the $[Mg{-}BH_4]^+$ is electrochemically stable at the Mg metal potentials [52], experimental evidence shows the presence of some boron hydride phase forming concomitant with the Mg plating, probably due to BH_4^- decomposition [51].

Weakly coordinating anions (WCAs) are preferable for both, calcium and magnesium electrolytes, in order to decrease the cation-anion interactions in solution. This is the case of the carba-closo-dodecaborate anion $[CB_{11}H_{12}]^-$, which Mg salt was reported for Mg electroplating using either triglyme or a G1/diglyme (G2) mixture as solvents [39, 53]. The solvent is able to dissociate entirely the salt, producing $[Mg(G2)(G1)_2]^{2+}$ complexes in solution with no interaction with the anion. Moreover, the electrolyte was found to be completely stable during Mg plating/stripping without anion or solvent decomposition observed in the XPS spectra of the deposited Mg [54].

Although the surface of the magnesium electrode seems to remain passivation-free in electrolytes based on magnesium chloro-aluminates, or in $Mg(CB_{11}H_{12})_2$, this is not always the case as the low redox potential of the magnesium metal may promote the decomposition of the electrolyte components. For example, a piece of metallic Mg immersed in a solution of $Mg(TFSI)_2$ (magnesium *bis*(trifluoromethane)sulfonimide) in G1 exhibits the formation of a thin solid surface layer with evident presence of fluorine (detected by XPS) arriving from anion decomposition [55]. This situation can be avoided if some $MgCl_2$ or $Mg(BH_4)_2$ is added to the solution, as the more coordinating anions will displace the TFSI in the Mg^{2+} solvation shell and prevent its approximation to the electrode during the plating [56, 57]. These studies exemplify the strong relationship existing between the solvation structure of the cation and its electroactivity and will be expanded upon in the next section.

Lastly, electrolytes employing $Mg[B(hfip)_4]_2$ (magnesium *tetrakis*(hexafluoroisopropyloxy)borate, Figure 1.8) in G1 or THF have shown high oxidative stability, high ionic conductivity, and good efficiency of Mg deposition, making them some of the most promising electrolytes for Mg-metal batteries [58]. Analysis of the electrode surface after Mg deposition indicates that this anion can decompose forming MgF_2, MgO, $MgCO_3$, and some unidentified boron compounds [59]. These results are in agreement with DFT calculations showing the decomposition pathways of alkoxyborate anions in Mg-containing electrolytes during plating [60].

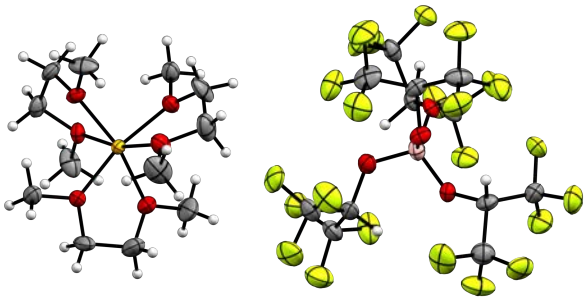

Figure 1.8: Molecular structure of cation and anion in the crystalline $Mg(G1)_3[B(hfip)_4]_2$. Redrawn from CIF file reported in Ref. [58]. Mg in orange, C in grey, O in red, B in pink, F in light green, and H in white.

1.4.2 Electrolytes allowing for Ca plating

Electroplating of Ca metal from organic electrolytes has been investigated to a much lesser extent due to the restricted choice of electrolytes solutions allowing the reversible reaction to occur. This is the result of the highly reductive potential of calcium metal, which will promote the decomposition of most electrolytes forming surface passivation layers which in most cases prevent Ca^{2+} migration [61].

The first successful calcium plating was reported in 2016 using $Ca(BF_4)_2$ in a mixture of ethylene carbonate (EC) and propylene carbonate (PC) as electrolyte at elevated temperature ($T > 75$ °C) [62]. Although needing high temperature to allow for plating/stripping, the use of carbonate solvents allowed the use of this electrolyte together with high voltage positive electrodes. A detailed study of the surface layer formed in the negative electrode using this electrolyte is presented in this thesis (see Chapter 4), showing the beneficial effect of a boron-containing surface layer, derived from anion decomposition.

More recent studies reporting Ca plating are derived from analogous Mg cases. For example, a $Ca(BH_4)_2$ in THF electrolyte allows for calcium plating and stripping with high coulombic efficiency (CE ~96%) with a surface layer composed mainly of CaH_2 [63]. The use of $Ca(BH_4)_2$, however, is limited to THF or other ether solvents not susceptible to reduction. These solvents, however, present a limited stability upon oxidation as was demonstrated for Mg. A study of Ca plating over Au or Pt electrodes from this electrolyte showed that a chemical step precedes the calcium metal deposition. This chemical step was attributed to the dehydrogenation reaction of THF or BH_4^-, form-

ing the CaH_2 [64]. A similar hydride-rich surface layer was observed in the $Ca(CB_{11}H_{12})_2$ electrolyte, in contrast to the magnesium case which remain passivation-free in the analogous electrolyte [65].

Ca plating was demonstrated also in a $Ca[B(hfip)_4]_2$ electrolyte, where the deposited calcium was found to be covered by CaF_2 coming from anion decomposition [66, 67]. Surprisingly, other decomposition products like a boron-containing phase for example, are seldom mentioned. This electrolyte formulation is currently the most promising for room-temperature Ca plating, although a deeper understanding of the SEI layer formed is needed.

1.5 Relationship between solvation shell and electroplating of divalent metals

Due to the high charge density of the divalent cations, they tend to bind more strongly to the ligands in their solvation shells, a fact that undoubtedly influences the kinetics of electroplating. Recently the relationship between the solvation structure of Ca^{2+} and Mg^{2+} and the operation of the respective metal electrode is attracting more and more attention. DFT calculations have shown that, starting from a fully solvated Mg^{2+} cation, the desolvation of the first coordination site is the rate-limiting step, after which the cation readily accepts 1 e^- ($Mg^{2+} \longrightarrow Mg^+$), then loses the rest of the solvation shell and gets fully reduced ($Mg^+ \longrightarrow Mg_{(s)}$) [49]. The single-charged cation Mg^+ is unstable, and promotes the decomposition of the solvating molecules, which explains why the passivation layer in most cases seems to be directed by the solvation shell of the cation. This mechanism, however, does not apply once the passivation layer is fully formed, as the cation needs to be completely naked to cross it and reach the surface. In this case, the desolvation of the last solvent molecule and the cation migration through the passivation layer are expected to limit the entire plating process. This analysis is also true for calcium plating. For example, it was observed that plating from a $Ca[B(hfip)_4]_2$ electrolyte can be completely hindered by using a strongly coordinating solvent, like triglyme [68].

Further solvation shell engineering can be performed by including a second anion in the electrolyte. This strategy has been employed, for example, to allow reversible Mg plating from a $Mg(TFSI)_2$ solution in diglyme after the addition of $MgCl_2$ or $Mg(BH_4)_2$ co-salt [57]. The anion of the co-salt is in these cases expected to bind more strongly to the cation than the TFSI anion,

avoiding its decomposition on the surface. A similar case study was reported recently for $Ca(TFSI)_2$ + $Ca(BH_4)_2$ in THF electrolytes [69].

The desired tailoring of the solvation shell can also be accomplished by incorporation of a suitable electrolyte additive, as reported recently [70]. Different methoxy ethyl-amines (*e.g.* ethylenediamine) were added, and their participation in the cation complexation demonstrated. Moreover, the solvation shell displays favourable characteristics, promoting a fast rearrangement at both cathode and anode interfaces and thus promoting fast reaction kinetics. The high cathodic stability limit of the amines guarantee their stability against calcium and magnesium metal electrodes, but their anodic stability needs to be carefully monitored as they are reported to undergo polymerization and formation of surface films upon oxidation [71, 72].

Further discussions on cation solvation and surface layer formation will be presented in Chapter 4.

1.6 Scope and objectives of this thesis

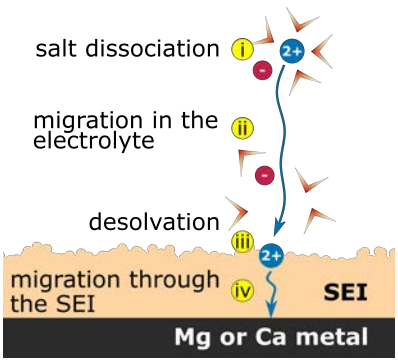

Figure 1.9: Scheme of the different processes occurring during Ca or Mg plating.

To summarize, the electrolyte formulation plays an important role in the conception of magnesium and calcium metal batteries. Not only the individual properties of solvent, salt and additives need to be considered, but also the interactions between them, particularly through the solvation of the cations. In order to optimize the electrolyte formulation for divalent metal plating, different processes need to be tailored (Figure 1.9) [73]:

- A high degree of cation-anion dissociation is needed to produce high number of charge carriers and decrease the ohmic losses in the cell.

- A high mobility of the charge carriers, which will influence the mass transport and the concentration polarization.
- Moderate desolvation energy of the cation at the interface between SEI and electrolyte.
- High mobility of the naked ion across the SEI.
- Low activation energy for electron-transfer and metal nucleation and growth.

In the three chapters comprising the body of this thesis, different aspects of the electrolyte formulation will be discussed, always with the aim of optimizing these five critical points. The ocerall objective of the thesis is to advance Ca plating kinetics, while using an electrolyte with a wide enough electrochemical stability window to allow for benchmarking of high voltage positive electrodes.

2

Salts

Traditionally, salts based on weakly coordinating anions are employed in LIBs given their high solubility in organic solvents, and thus, the high ionic conductivity of the resulting electrolyte. This is even more important when employing divalent cations, as their higher charge density makes them more susceptible to interactions with anions in solution. In addition, the use of metals with low redox-potential, such as calcium and magnesium, as anodes of next-generation batteries requires electrolytes with water contents below ppm-levels, to avoid the formation of oxides or hydroxides on their surface.

However, compared to lithium, there is a low availability of calcium and magnesium salts of sufficient purity in the market, posing a significant challenge in the study of these systems. In this chapter some efforts in the production of several calcium salts are presented, either from the commercially available hydrates ($Ca(BF_4)_2 \cdot xH_2O$, for example) or from anhydrous synthesis routes. A structural and spectroscopic characterization was performed by means of powder and single-crystal X-ray diffraction (XRD), nuclear magnetic resonance (NMR) and infrared (IR) spectroscopies, and mass spectrometry when necessary.

2.1 Drying of commercial $Ca(BF_4)_2 \cdot xH_2O$

Calcium tetrafluoroborate is commonly prepared in water and sold commercially only as a hydrate ($Ca(BF_4)_2 \cdot xH_2O$) [74]. Its use in battery electrolytes requires a drying protocol, which is not necessarily straightforward, as will be discussed in this Section.

Three methods were employed to quantify the amount of water in commercial $Ca(BF_4)_2 \cdot xH_2O$. Thermogravimetric analysis (TGA) of the salt shows an initial weight loss of 16.7% with an onset at 50 °C, which is attributed to

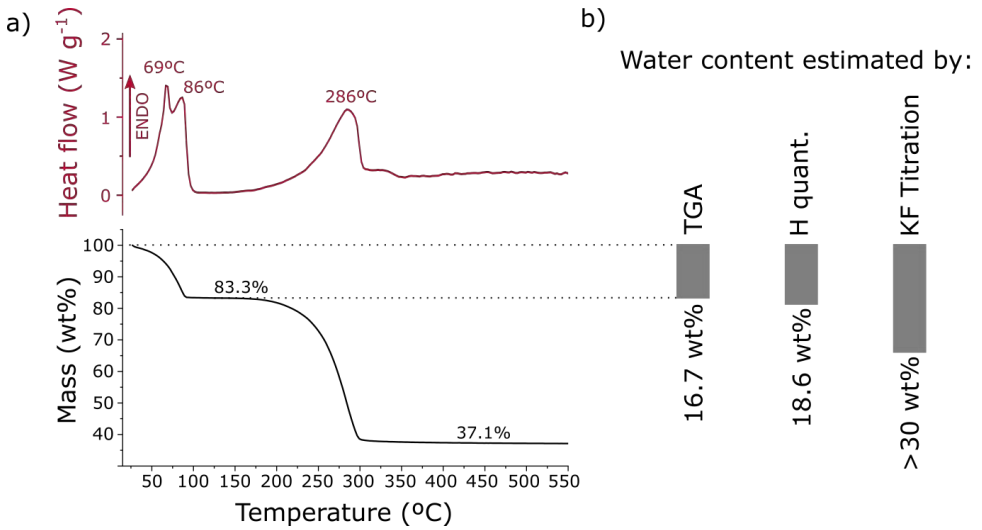

Figure 2.1: Thermal analysis of commercial $Ca(BF_4)_2 \cdot xH_2O$. a) Differential scanning calorimetry (upper panel) and Thermogravimetric analysis (lower panel) of the commercial salt, recorded at 5 °C/min. **b)** water content estimation by three different methods.

a water loss (Figure 2.1a, grey trace). Curiously, in this temperature range two peaks are observed in the scanning calorimetry curve (Figure 2.1a, red trace), which are the result of two endothermic reactions occurring at this temperature range. The presence of two different reactions can be explained by the evaporation of water molecules from two different environments (*e.g.* surface *vs.* crystalline water) or to another non-identified reaction occurring concomitant to the water evaporation.

A second weight loss, of 46.2%, is observed starting at 210 °C, which can be attributed to salt decomposition into some volatile species, although the recorded temperature is slightly lower than the reported decomposition temperature of $Ca(BF_4)_2$ into BF_3 and CaF_2 (280–285 °C) [75]. The previous estimation used a slightly faster heating rate than the TGA presented here (9 °C/min vs. 5 °C/min respectively), which may explain the small differences observed. However, it is also possible that the presence of some remaining water after the first weight loss would promote the decomposition of the anion at lower temperatures. This hypothesis will be discussed deeper further down.

The second method to determine the water content was based on elemental quantification of hydrogen by combustion (see Chapter 6 – Experimental methods). A total amount of 2.07 wt.% of H was obtained, which would

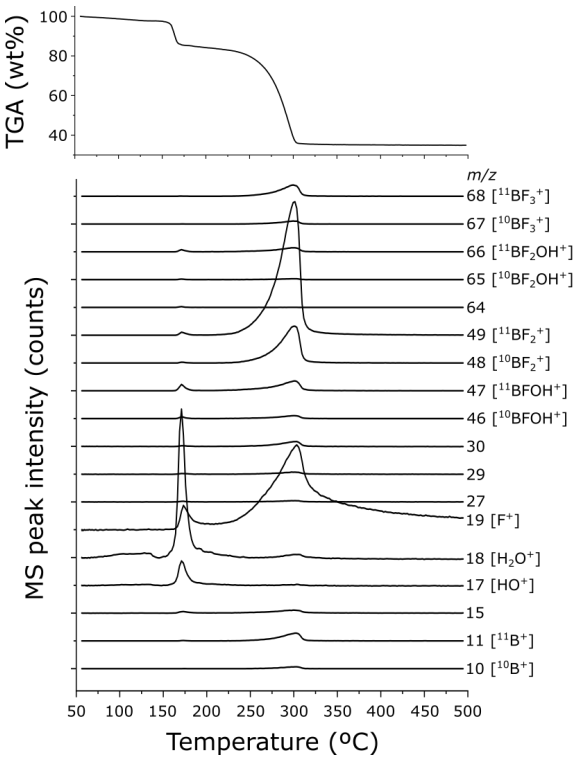

Figure 2.2: TGA-MS of the commercial $Ca(BF_4)_2 \cdot xH_2O$ Upper panel: TGA trace of the commercial salt at 10 °C/min. Lower panel: Evolution of relevant fragments as function of temperature, the fragments were assigned considering the corresponding isotopic distributions.

correspond to 18.6 wt.% of water in the commercial salt.

A third method consisted in dissolving a small amount of the salt in a previously dried EC:PC mixture ($[H_2O] < 5$ ppm) and measuring the water content of the resulting solution by Karl-Fischer (KF) Coulometric titration. The water content found in the salt was around 30 wt.%, significantly higher than the estimations made by the previous two methods. The higher content of water estimated by KF titration may be the result of interferences of the anion during the measurement, as described in the experimental methods. This highlights the low reliability of KF to determine the water content of $Ca(BF_4)_2$ electrolytes. This interference is expected to play a particularly prominent role when the electrolyte under test has high water content, for example, the solutions employed for this experiment had a salt concentration of 0.1 M and resulted in water contents of around 7000 ppm according to KF.

To better understand the possible chemical reactions of the salt during the TGA essay, the mass spectra of the evolved gases was recorded and analysed by electron-ionization mass spectrometry (EI-MS). Using the EI, the decomposition products evolved from the sample are fully fragmented and these

fragments are counted as function of time. Figure 2.2 shows the TGA trace together with the evolution of some selected fragments. As expected, a big increase in the fragment of mass to charge ratio (m/z) 18 [H_2O^+] is recorded above 170 °C, corresponding with the first weight loss. An increase in the fragment of m/z 19 [F^+] during the same weight loss indicates that the anion is being decomposed even at these low temperatures. Upon further heating, the anion is completely decomposed as fragments of m/z 68 [BF_3^+], m/z 49 [BF_2^+], and m/z 19 [F^+] are detected in the evolved gases. Additionally, fragments of m/z 66 [BF_2OH^+] and m/z 47 [$BFOH^+$] are detected, demonstrating the hydrolysis of the BF_4^- anion during the heating process.

In LIBs, electrolytes based on PF_6^- or BF_4^- anions are known to suffer from hydrolysis if traces of water are present, releasing corrosive HF in the solution and promoting the formation of LiF in the SEI.[7] This anion decomposition reaction is expected to be exacerbated by the presence of a divalent cation, such as Ca^{2+}, which results in the precipitation of highly stable CaF_2.[76, 77] As the standard Gibbs free energy for CaF_2 formation is much higher than the one for LiF (–1167.3 *vs.* –587.71 kJ mol^{-1} respectively [78]), the anion is thermodynamically pushed to decompose when Ca^{2+} is present, a process that is further enhanced at higher temperatures.

In order to limit the anion decomposition, the removal of most of the water in the solid was performed at lower temperatures, following the next protocol:

1. A room temperature drying step using a rotary pump and a liquid nitrogen trap ($P \sim 8$ x 10^{-2} mbar) for at least 12h.
2. Increase the temperature to 80 °C and dry for another 12 h using a turbo pump and a liquid nitrogen trap ($P < 5$ x 10^{-3} mbar).
3. Increase the temperature to 120 °C at the same conditions, dry for 12 h.
4. Increase the temperature to 140 °C at the same conditions, dry for 12–24h.

At the end of this drying procedure, the commercial salt losses in total an average of 24% of its original weight.

Using this vacuum-dried salt, 0.45 M $Ca(BF_4)_2$ in EC:PC electrolytes were prepared, containing 700–1000 ppm of water according to KF titration. This amount of water would correspond to a total of 1–1.4 wt.% of water in the solid salt that was not removed during the drying procedure. As such elevated

water content would be detrimental for the operation of a Ca-metal battery, several drying procedures of the electrolyte itself were attempted.

First, the use of a water trapping agent was considered by placing the electrolyte on a bed of 3 Å molecular sieves. The amount of water was reduced to ∼400 ppm. However, no further decrease was recorded even after two weeks and several changes of freshly activated molecular sieves. Additionally, a significant K^+ or Na^+ contamination was found when molecular sieves are in contact with a calcium-containing electrolyte (> 500 ppm, measured by inductively coupled plasma mass spectrometry, ICP-MS), probably due to a cation exchange between the sieves and the solution. Given the risk of contamination and the low efficiency of this drying method, it was not further considered for future electrolyte preparation.

Second, the use of calcium hydride as water scavenger agent was investigated. The low solubility of both CaH_2 and $Ca(OH)_2$, which is produced by its reaction with water, would allow for an easy removal by filtration. However, the addition of 50 mg of $CaH_{2(s)}$/mL of electrolyte solution had no effect on the water content after one day of constant stirring. When the electrolyte was heated at 90 °C for 24 h in the presence of CaH_2, the amount of water decreased to 140 ppm. The remaining powder at the end of this process was filtered and rinsed with DMC, its powder X-ray diffraction pattern is shown in Figure 2.3. Remarkably, no presence of calcium hydroxide was recorded and the solid is entirely composed from unreacted CaH_2 mixed with crystalline

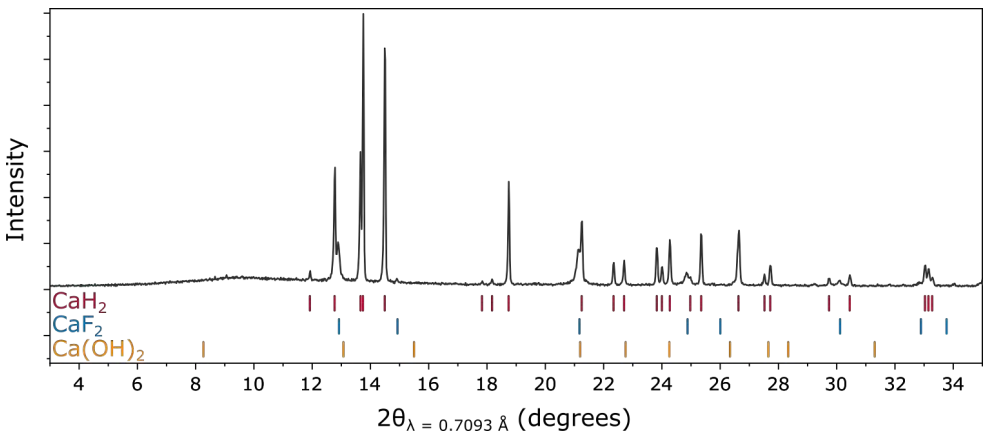

Figure 2.3: Powder XRD pattern of the reaction product of $CaH_{2(s)}$ and $Ca(BF_4)_2$ electrolytes. Peak positions for CaH_2 (ICSD 260873), CaF_2 (ICSD 60559), and $Ca(OH)_2$ (ICSD 51411) are shown as references.

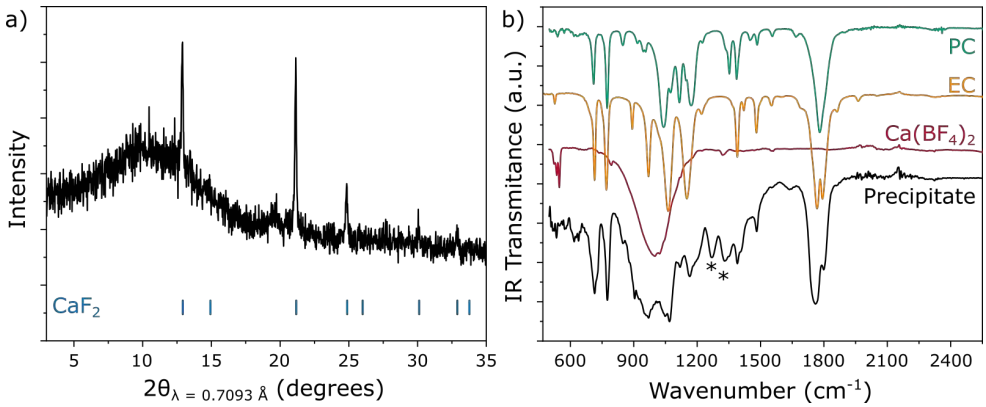

Figure 2.4: Characterisation of the precipitate formed in the electrolyte solution during heating. a) powder X-ray diffraction pattern of the precipitate. Peak positions of CaF_2 (ICSD 60559) are shown as references. **b)** FTIR spectra of the precipitate compared to the original components of the solution.

CaF_2, suggesting that instead of water consumption only the anion is being decomposed.

It is suggested that the BF_4^- anion itself must be acting as a water-scavenging agent at high temperatures. This hypothesis was tested by heating a 0.43 M $Ca(BF_4)_2$ in EC:PC electrolyte (containing around 1000 ppm of water) at 90 °C for 24 h. At the end of this heat treatment the water content decreased to 135 ppm, and the concentration of BF_4^- anion also decreases from 0.43 to 0.34 M evidencing a significant decomposition (the concentration of BF_4^- in solution before and after the thermal treatment was measured by qNMR, as described in Chapter 6, page 110). A gel-like film was formed at the bottom of the flask which was recovered, washed with DMC, and analysed by attenuated total reflectance Fourier transformed infrared spectroscopy (ATR-FTIR) and powder XRD (Figure 2.4).

The XRD pattern of the solid shows evidence of an amorphous phase with the presence of some crystalline CaF_2. Meanwhile, in the FTIR spectrum most of the bands may be attributed to remaining EC, PC, or $Ca(BF_4)_2$ from the electrolyte. In the region between 850 to 1100 cm^{-1} several contributions of different, poorly resolved bands are observed. There are two evident new bands (1269 and 1334 cm^{-1}) which can be attributed to B−O stretching vibrations in an amorphous boron compound, likely produced by anion decomposition/hydrolysis (not evidenced in the XRD).

As a conclusion, clear evidence of BF_4^- decomposition is observed upon ther-

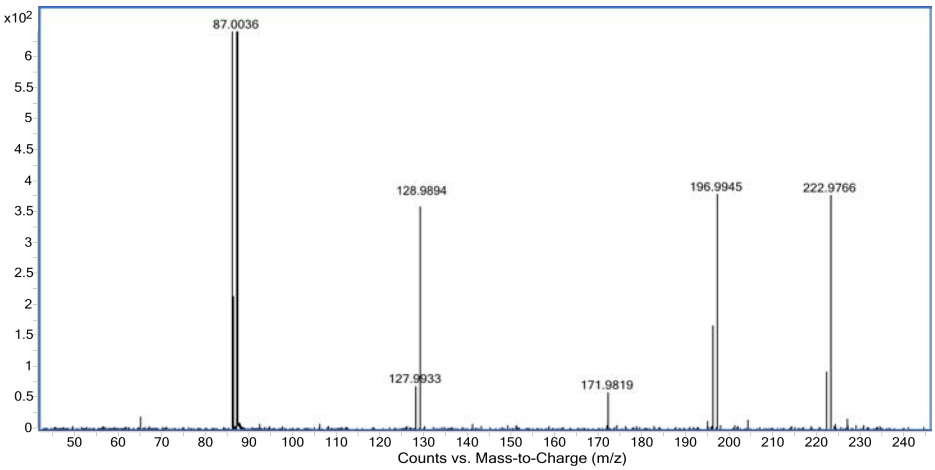

Figure 2.5: ESI-MS spectrum of a $Ca(BF_4)_2$ in EC:PC electrolyte after heat treatment. The use of electrospray-ionization (ESI) allowed the identification of high-molecular weight ions without fragmentation.

mal treatment of the electrolyte, a situation particularly aggravated by the presence of Ca^{2+} cations. Previously, Ca^{2+} has been used to remove BF_4^- and F^- contaminants in waste water by promoting the formation of stable CaF^+ and CaF_2 species, particularly at high temperature [76, 77]. In the case of organic electrolytes, as the ones studied here, this hydrolysis of tetrafluoroborate anion is acting as a water scavenger itself with longer heating times producing drier electrolytes, but at the expense of salt concentration. Preparation of very dry $Ca(BF_4)_2$ electrolytes was possible experimentally by heating the prepared electrolyte at 90 °C for long times.

It must be stressed that, although dry electrolytes were obtained by heating, this is not a desirable or optimal method for producing suitable electrolytes. The water content always decreases at the expense of anion concentration, producing several undesirable products. Apart from solid CaF_2 and the amorphous borate compound discussed before, which can be separated by filtration, several soluble boron compounds were observed in the mass spectrum of the filtered electrolyte (Figure 2.5). The intense peak at m/z 87.0036 corresponds to the expected BF_4^- predominant component of the electrolyte, the peaks at m/z 128.9894 and m/z 222.9766 correspond to higher molecular weight anions containing one boron atom (given the small satellite peak 1 u below the main peak and intensity ¼). Similarly, the peak at m/z 196.9945 corresponds to an anion with two boron atoms, based also in the boron isotopic distribution.

2.2 Anhydrous synthesis of $Ca(BF_4)_2$

The previous Section has outlined the difficulties to produce sufficiently dry $Ca(BF_4)_2$ starting from the commercial hydrate salt. In this Section, two anhydrous synthesis routes will be presented.

2.2.1 Solvothermal synthesis from borontrifluoride diethyletherate ($BF_3 \cdot O(CH_2CH_3)_2$) – Synthesis A

De Pape & Ravez studied the thermal properties of the anhydrous tetrafluoroborates of alkaline earth metals, which were prepared from the reaction of the corresponding fluoride with borontrifluoride diethyletherate (Equation 2.1) [79]. This reaction takes place only at high temperature, as the $BF_3 \cdot OEt_2$ complex dissociates only at $T > 130$ °C [80].

$$CaF_2 + 2\,BF_3 \cdot OEt_2 \xrightarrow{\Delta} Ca(BF_4)_2 + 2\,Et_2O \tag{2.1}$$

In a typical synthesis, 1.47 g of ultradry CaF_2 (18.8 mmol) were mixed with an excess of boron trifluoride diethyletherate (6 g, 42.2 mmol) in a polytetrafluoroethylene (PTFE)-lined stainless-steel autoclave (Figure 2.6). The autoclave was tightly closed inside an Ar filled glovebox and transferred to an oven at 150 °C. After 72h, the autoclave was cooled at room temperature and transferred back to the glovebox. The solid product was recovered and washed several times with dry DMC, a total mass of 2.99 g was obtained, corresponding to a yield of ∼59%. The presence of unreacted CaF_2 is evident in the powder XRD pattern that will be discussed in Section 2.2.3.

The reaction yield did not significantly increase by extending the reaction time. The low yield is attributed to the very low solubility of both CaF_2 and $Ca(BF_4)_2$ in the diethyletherate. As the reaction proceeds, the reaction product covers the surface of the CaF_2 particles and hampers further reaction. The use of a more suitable solvent (anhydrous HF) is explored in the following

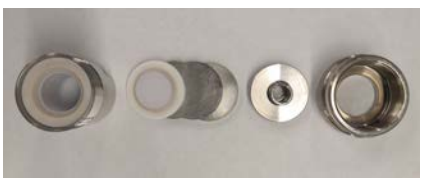

Figure 2.6: PTFE-lined stainless-steel autoclave used for $Ca(BF_4)_2$ synthesis.

Section.

2.2.2 Synthesis from $BF_{3(g)}$ in anhydrous HF – Synthesis B

Compared to other solvents, CaF_2 is slightly soluble in anhydrous HF (aHF), which makes it suitable for the synthesis of $Ca(BF_4)_2$ following Equation 2.2:

$$CaF_2 + 2\,BF_{3(g)} \xrightarrow{\text{aHF}} Ca(BF_4)_2 \tag{2.2}$$

This synthesis has been made in collaboration with Dr. Matic Lozinšek and Dr. Kristian Radan from the Jožef Stefan Institute (Ljubljana – Slovenia). The handling of HF, F_2 and BF_3 was performed in a metal vacuum line (nickel, copper) equipped with Monel Helicoid pressure gauges, PTFE valves, a soda lime scrubber, liquid-nitrogen-cooled traps, and a two-stage rotary vacuum pump. Commercial aHF was stored into a 1.9 cm outer diameter, 1.6 cm inner diameter and 23 cm long fluorinated ethylene propylene (FEP) vessel containing ∼1 cm high of K_2NiF_6 for water traces removal (Figure 2.7).

The reaction vessel consisted in a FEP tube (19 mm outer diameter, 16 mm inner diameter, 29 cm long; V = 58 mL) equipped with a PTFE valve and a PTFE-coated magnetic stirrer bar (Figure 2.7c). The reaction vessel was passivated with F_2 prior to use.

In a typical batch, 180 mg (2.31 mmol) of solid CaF_2 were weighed in the

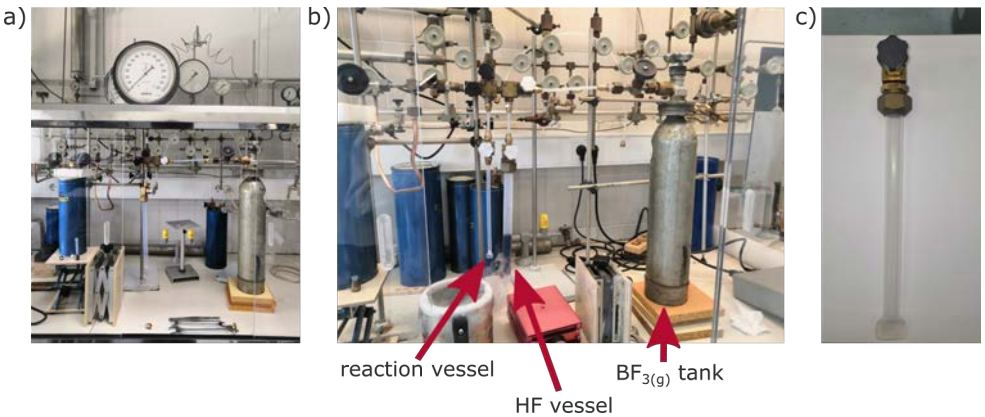

Figure 2.7: Equipment employed in the anhydrous synthesis of $Ca(BF_4)_2$ at room temperature. **a)** General view of the F_2 resistant vacuum line, **b)** detailed view of the assembly showing the reaction vessel, the HF storage vessel and the $BF_{3(g)}$ tank connected to the line, and **c)** FEP reaction vessel employed for the synthesis.

reaction vessel inside a glovebox. The reaction vessel was then connected to the vacuum line and the connections were passivated with F_2 for few hours. Approximately 3.6 mL of aHF were dispensed under static vacuum from the K_2NiF_6-containing storage vessel into the FEP reaction vessel which was kept at -196 °C in a liquid-nitrogen bath. Upon warming of the reaction vessel to room temperature, some of the solid was dissolved yielding a colourless solution over a white solid. An excess of BF_3 (∼7.66 mmol) was condensed into the FEP reaction vessel following the same procedure, together with more aHF solvent. The reaction was warmed to room temperature and let stirring for 2 days after which the aHF and the excess BF_3 were pumped out.

2.2.3 Characterization of the synthesized $Ca(BF_4)_2$

The formation of the desired product was confirmed in both cases by powder XRD (Figure 2.8). In the case of synthesis A, the low solubility of the CaF_2 precursor in the reaction media results in an incomplete reaction and some CaF_2 can be clearly observed in the obtained product. Rietveld refinement of the XRD pattern led to an estimation of 70 wt.% of $Ca(BF_4)_2$, the remaining 30 wt.% being attributed to CaF_2 (details of the Rietveld refinement are presented in Annex A). Synthesis B produces a much purer product, with all the peaks in the XRD pattern being assigned to the desired anhydrous $Ca(BF_4)_2$.

Figure 2.9 shows the ^{19}F and ^{11}B NMR spectra of the two synthesized salts,

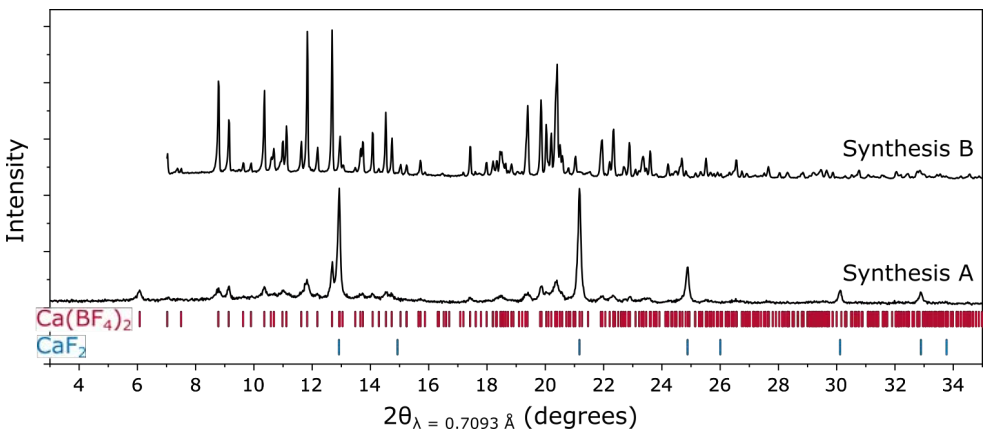

Figure 2.8: Powder XRD patterns of the $Ca(BF_4)_2$ prepared by the two anhydrous routes. Peak positions of CaF_2 (ICSD 60559) and $Ca(BF_4)_2$ (ICSD 1839) are shown for reference.

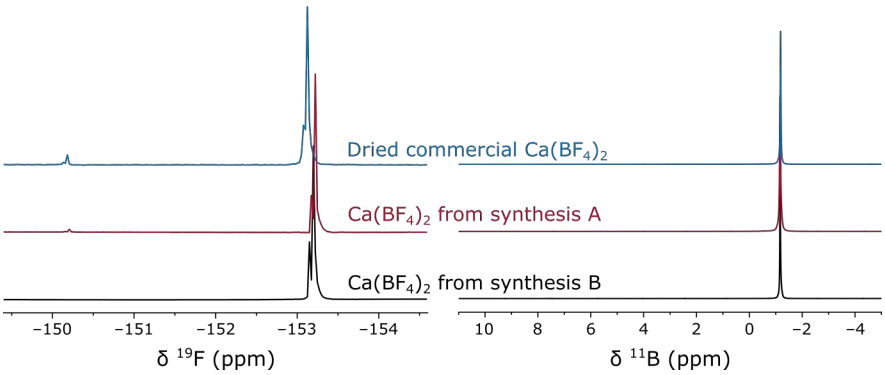

Figure 2.9: NMR spectra of the obtained $Ca(BF_4)_2$ by the two synthetic routes compared to the commercial product.

compared to the commercial salt dried with the protocol described in Section 2.1. The ^{11}B NMR shows a single peak at -1.20 ppm in the three cases, agreeing with the reported chemical displacement for the tetrafluoroborate anion.[81]

In the ^{19}F spectrum, the formation of the desired anion is also confirmed by the doublet at -153 ppm. A doublet is observed in this case due to the 80:20 isotopic ratio of ^{11}B:^{10}B, which influences the chemical environment of the fluorine ligands. A small impurity is observed at -150.2 ppm in the product of synthesis A, which is also present in the commercial $Ca(BF_4)_2$ after drying. Although we are unable to determine the exact chemical composition of this

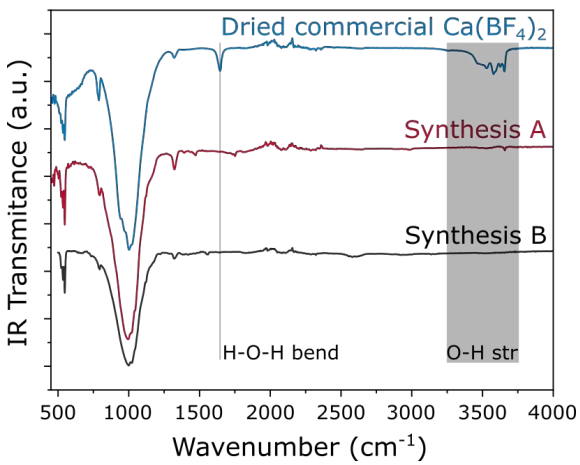

Figure 2.10: IR spectra of the obtained $Ca(BF_4)_2$ from synthesis A and synthesis B, compared to the commercial product after drying.

impurity, its ^{19}F chemical displacement suggests that is a BF_4^- decomposition product in which a –F ligand has been displaced by other lower electrowithdrawing group (as –OR) producing a downfield shift in the ^{19}F resonance [82].

Figure 2.10 shows the FTIR spectra of the prepared $Ca(BF_4)_2$ salts evidencing three of the four fundamental vibrations of the tetrahedral BF_4^- (543 cm^{-1}, 786 cm^{-1} and 1010 cm^{-1}), while the forth one is out of the experimental range (expected below 350 cm^{-1}) [83], refer to Table 2.1 for the respective assignments. Due to symmetry restrictions, only the bands at 543 cm^{-1} and 1010 cm^{-1} are supposed to be infrared active, however an asymmetric coordination environment in the solid would distort the original T_d structure and would activate the remaining vibration modes. The satellite band at 1310 cm^{-1} is also attributed to this symmetry distortion. Even after the extensive drying of the commercial salt, bands at 1642 and ∼3500 cm^{-1} clearly evidence the presence of water.

2.3 Preparation of solvated salts $Ca(BF_4)_2(DME)_2$ and $Ca(BOB)_2(DME)_2$

Given the low solubility of calcium salts in organic electrolytes, new calcium salts can be prepared by metathesis in which the desired calcium salt is precipitated from a respective lithium solution in a suitable solvent. This method was used recently in the preparation of $Ca(PF_6)_2$ [84], although the low solubility of the $CaCl_2$ precursor used would probably result in low yields. In this Section the isolation and characterization of $Ca(BF_4)_2$ and $Ca(BOB)_2$ from the corresponding $Ca(TFSI)_2$ solution is presented (BOB = $[B(C_2O_4)_2]^-$, bis(oxalato)borate).

$$Ca(TFSI)_2 + 2\,LiX \xrightarrow{DME} CaX_2\downarrow + 2\,LiTFSI \tag{2.3}$$

5 mL of a 0.5 m solution of $Ca(TFSI)_2$ in previously dried DME ($[H_2O]$ < 5 ppm) were carefully added on top of 3 mL of 1.5 m solution of $LiBF_4$ (or LiBOB accordingly). The addition was done paying particular attention to avoid any fast mixing, so that the calcium solution remained on top and the ions diffuse slowly across the solution. The vial was let undisturbed for three days, after which crystalline solids were obtained at the bottom of the flask. The crystals were washed several times with DME and left to dry in an open

vial inside the Ar-filled glovebox.

Attempts to obtain $Ca(BOB)_2$ by this route using water as solvent resulted in precipitation of calcium oxalate as the only product. When using THF as solvent, no solid is precipitated, the solution turns white and very viscous, suggesting some anion or solvent decomposition and the formation of a polymer. The reaction was only successful when a DME was used, given its high stability and low nucleophilicity.

2.3.1 Chemical and thermal characterization

Previous reports suggest that the produced salt by metathesis reaction might result in significant contamination from the Li^+ or TFSI used as initial reactants [85, 86]. The two obtained solids were analysed by ICP-MS to quantify the content of Ca, B, and Li. A 2:1 molar ratio of B:Ca was observed in both cases, and with Li contents below 100 ppm.

Following the quantification procedure described in the Experimental Section (Chapter 6, page 111), the number of DME molecules included in the crystal in each case was estimated by ^{1}H qNMR. A ratio DME:Ca^{2+} of 2:1 was found for both compounds, and thus the molecular formulas are confirmed as: $Ca(BF_4)_2(DME)_2$ and $Ca(BOB)_2(DME)_2$.

To evaluate the release of DME from the crystal solids, the TGA of both solvates was measured at 5 °C min^{-1} from room temperature to 600 °C, the respective traces are presented in Figure 2.11, compared to the obtained before for the commercial $Ca(BF_4)_2 \cdot xH_2O$ hydrate under the same conditions. In the case of $Ca(BOB)_2(DME)_2$, a two-step loss is observed at 124 and 188 °C respectively, with each step corresponding to 13.7 wt.% and agreeing with the loss of one DME molecule each time (theoretical weight loss = 15.1 wt.%). A third weight loss starting at 279 °C corresponds to the decomposition of the BOB anion, slightly lower than the reported decomposition temperature of LiBOB (293 °C, measured at a 1 °C min^{-1} heating ramp) possibly due to the presence of the different cation [87].

The behaviour of $Ca(BF_4)_2(DME)_2$ is slightly more complex. A two-step loss is also observed in this case, at 98 and 150 °C, but the weight loss in each step is much higher than the expected for the release of DME from the structure (theoretical loss = 22.8 wt.%). This mismatch could be the result of undesired secondary reactions happening during the heating of the solid, although a deeper investigation is needed. A third step, related to anion

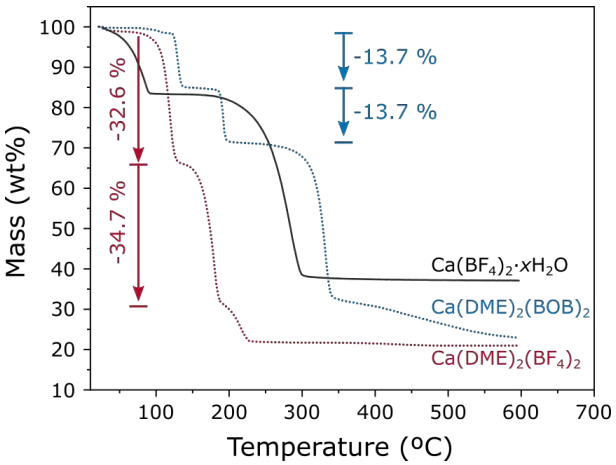

Figure 2.11: TGA traces of $Ca(DME)_2(BOB)_2$, $Ca(DME)_2(BF_4)_2$, and $Ca(BF_4)_2 \cdot xH_2O$. A constant heating ramp of 5 °C/min was applied, and a flow of dry N_2 gas was used.

decomposition can be seen starting at 199 °C, which is significantly lower than the reported decomposition temperature for anhydrous $Ca(BF_4)_2$ (280-285 °C) [75], and also lower than the previously observed for the commercial hydrate, discussed in Section 2.1.

2.3.2 Structural characterization

Crystals suitable for single-crystal XRD were grown using the same method described above, but employing lower concentrated solutions (0.18 m Ca $(TFSI)_2$ and 0.3 m LiX, with X = BOB or BF_4^- anions). Colourless crystals were obtained for both compounds. Upon exposure to air, they lose crystallinity and become white and brittle, indicating that DME molecules can be easily removed from the crystal structure, or exchanged by water from

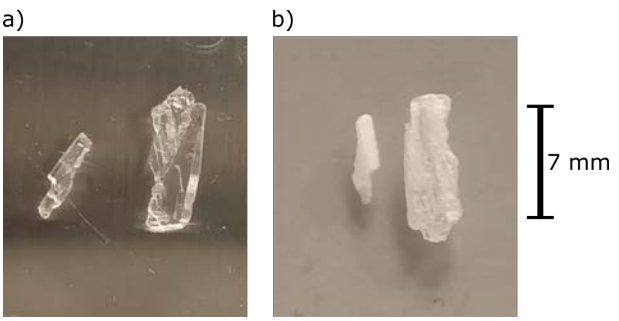

Figure 2.12: Picture of the prepared $Ca(BF_4)_2(DME)_2$ crystals. a) freshly prepared, and **b)** after 2 h in contact with air.

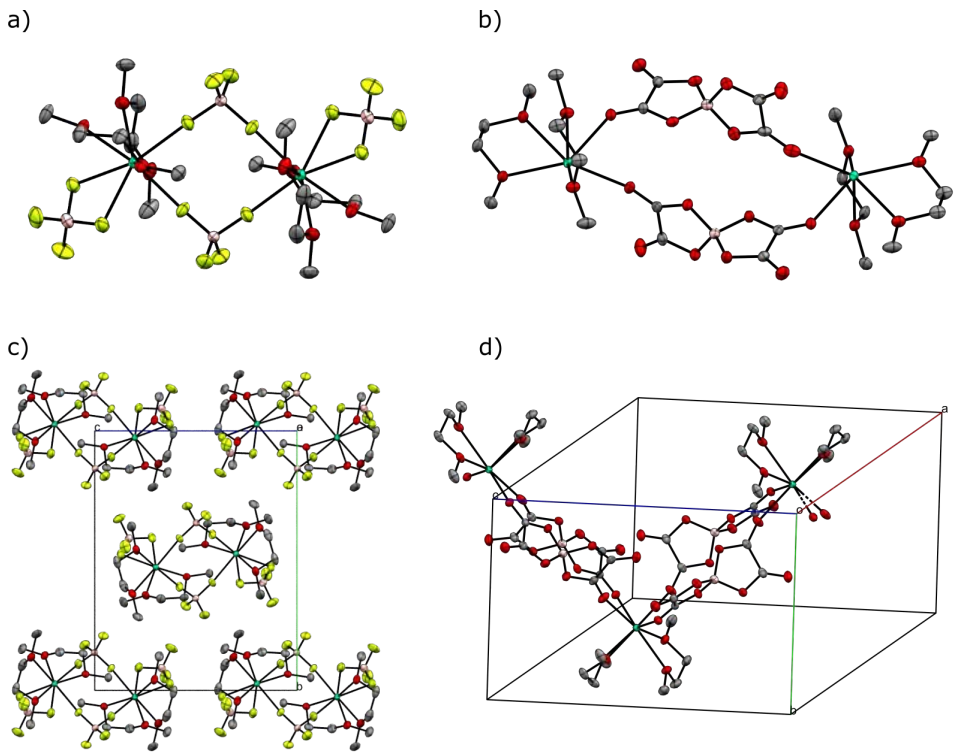

Figure 2.13: Crystal structure of $Ca(BF_4)_2(DME)_2$ and $Ca(BOB)_2(DME)_2$ salts refined from single-crystal XRD a) Structure of the $(BF_4)_4(DME)_4$ dimer, **b)** structure of the $[Ca(BOB)_2(DME)_2]_n$ chains, **c)** packing of the dimeric structure in the crystal, **d)** packing of the polymeric chains in the crystal. Ellipsoids are drawn for a probability of 50%. Ca, light blue; C, grey; F, green; O, red; protons are omitted for clarity.

the atmosphere (Figure 2.12). To avoid this, the crystals were stored in dry DME inside the glovebox until the XRD measurements were performed. The refinement of the crystal structures (Figure 2.13) was performed with collaboration of Dr. Matic Lozinšek from Jožef Stefan Institute (Ljubljana – Slovenia) and Prof. Elies Molins from the ICMAB.

The $Ca(BF_4)_2(DME)_2$ solvate crystallizes as $Ca_2(BF_4)_4(DME)_4$ dimers, in which two BF_4^- anions act as a bridge between the two calcium cations. The remaining two anions coordinate the Ca^{2+} cation in a bidentate configuration. Additionally, each Ca^{2+} is coordinated bidentately by two DME molecules, completing the 8-fold coordination environment typical for Ca^{2+} cations in solids (Figure 2.13a).Comparatively, the $LiBF_4(DME)_2$ analogue crystallizes as $[Li^+BF_4^-]$ pairs with the anion coordinating only monoden-

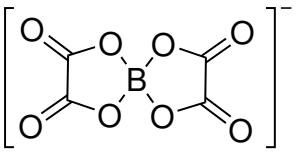

Figure 2.14: Chemical structure of the BOB anion.

tately the lithium cation [88]. Other $LiBF_4$ solvates have been reported, forming dimers or chains depending on the solvent molecule [89]. In all cases containing lithium, the anion coordination is monodentate. Bidentate coordination by BF_4^- has been reported before, but only in anhydrous monovalent salts like $NaBF_4$, KBF_4, $RbBF_4$, and $CsBF_4$, in which the ionic radius allows the accommodation of the anion by this configuration [90–93].

In contrast, the chemical structure of the BOB anion allows for the formation of coordination polymers as it displays four terminal O atoms in the two extremes of the molecule (Figure 2.14). This is the case of the $Ca(BOB)_2(DME)_2$ solvate, which crystallizes as $[Ca(BOB)_2(DME)_2]_n$ chains (Figure 2.13b and 2.13d). The backbone of the chains is formed by Ca^{2+} cations linked by a double bridge of BOB anion. Each anion binds one Ca^{2+} cation on each extreme by a monodentate configuration only. The equivalent solvate Li(BOB)(DME) also crystallizes forming coordination polymeric chains, but monodentate and bidentate coordination are present [94].

2.3.3 Spectroscopic characterization

The ^1H, ^{13}C, ^{11}B, and ^{19}F NMR spectra of the obtained products agree with the literature, confirming that the salts are obtained in high purity and with no contamination from TFSI anions:

$Ca(DME)_2(BF_4)_2$: ^1H NMR (DMSO-d_6, 400 MHz): δ 3.22 (s, 6H, C**H**$_3$O-CH$_2$CH$_2$OC**H**$_3$), 3.41 (s, 4H, CH$_3$OC**H**$_2$C**H**$_4$OCH$_3$). $^{13}C\{^1H\}$ NMR (DMSO-d_6, 100 MHz): δ 58.1, 71.2. ^{11}B NMR (DMSO-d_6, 128 MHz): δ -1.29 (s, **B**F_4^-), ^{19}F NMR (DMSO-d_6, 376 MHz): δ -153 (d, B**F**$_4^-$).

$Ca(DME)_2(BOB)_2$: ^1H NMR (DMSO-d_6, 400 MHz): δ 3.22 (s, 6H, C**H**$_3$O-CH$_2$CH$_2$OC**H**$_3$), 3.41 (s, 4H, CH$_3$OC**H**$_2$C**H**$_4$OCH$_3$). $^{13}C\{^1H\}$ NMR (DMSO-d_6, 100 MHz): δ 58.1, 71.1, 158.2. ^{11}B NMR (DMSO-d_6, 128 MHz): δ 7.36 (s, **B**$(C_2O_4)_2^-$).

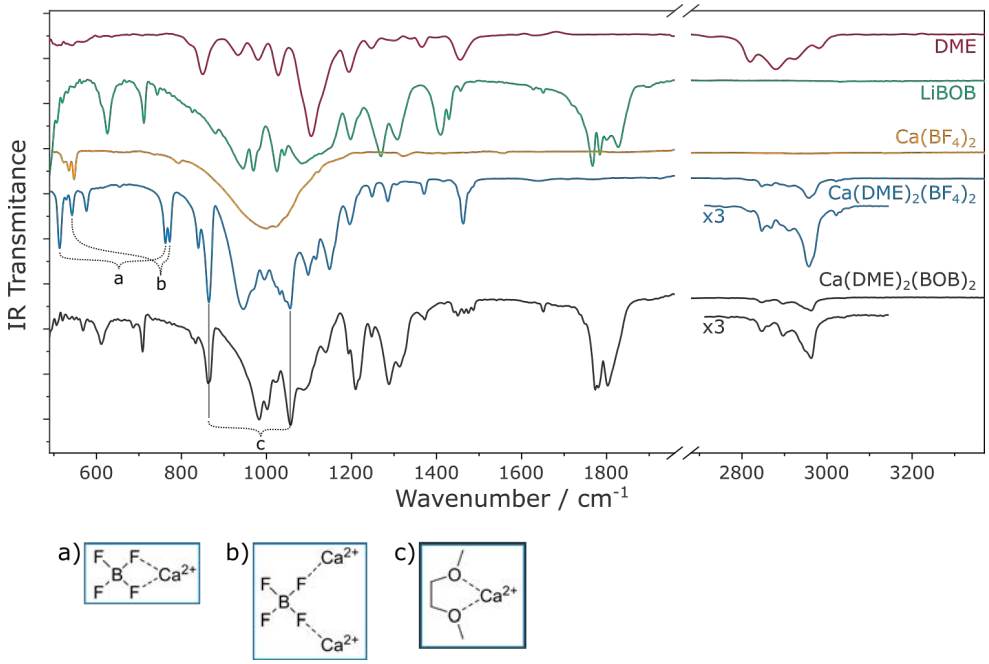

Figure 2.15: IR spectra of $Ca(BF_4)_2(DME)_2$ and $Ca(BOB)_2(DME)_2$ salts compared to pure DME, LiBOB, and $Ca(BF_4)_2$ Bands assigned to **a)** BF_4^- bidentate, **b)** BF_4^- bridging, and **c)** DME bidentate coordination are highlighted.

The infrared spectra of both solvated salts was measured and the assignment of some relevant bands was performed by comparison between them and with other reference compounds (Figure 2.15), a summary of the assignments is shown in Table 2.1. The coordination modes of DME and the anions towards the cation is discussed below.

The DME molecules in the neat solvent are conformationally *free*, resulting in broad bands in the C−H stretching region, around 2900 cm^{-1}. In solvated crystals, these bands evolve into very sharp peaks agreeing with a more rigid configuration of the DME chains. The CH_2 rocking mode at 850 cm^{-1} displaces to 869 cm^{-1} as expected from the *trans-gauge-trans* conformation of DME observed in the crystal structure [95]. The C–O–C stretching vibration of the neat solvent (at 1105 cm^{-1}) lies in a region crowded by several vibration modes of the BOB and BF_4^- anions. However, given the similarities between the DME coordination environments in $Ca(DME)_2(BF_4)_2$ and $Ca(DME)_2(BOB)_2$, we expect this vibration to occur at the same frequency. Thus, we assign the band at 1056 cm^{-1} to this vibration mode in the coordinated DME, also in agreement with other DME-containing complexes [96].

As discussed in section 2.2.3, the T_d symmetry of free BF_4^- anion implies that only two bands should be infrared active: 543 and 1010 cm^{-1}. In the solvate, however, two different coordination environments are present (the bidentate BF_4^- and the bridging BF_4^-, see Figure 2.13a), both of them with slightly distorted C_{2v} symmetry. The previously forbidden band at 786 cm^{-1} (assigned to the symm. stretching of the anion, ν_1) is then clearly visible and split into contributions at 772 and 762 cm^{-1}, corresponding to the two different BF_4^- in the solid. The same behaviour is observed for the band at 548 cm^{-1} (ν_4) which splits into 542 and 513 cm^{-1}, and the band at 1010 cm^{-1} (ν_3) which splits into 946 and 969 cm^{-1}.

Table 2.1: Assignment of some relevant IR bands of DME, LiBOB, $Ca(BF_4)_2$, $Ca(DME)_2(BF_4)_2$, and $Ca(DME)_2(BOB)_2$.

Vibration mode	neat DME	LiBOB	$Ca(BF_4)_2$	$Ca(BOB)_2$ $(DME)_2$	$Ca(BF_4)_2$ $(DME)_2$
		479		479	
$\nu_4(BF_4^-)$			547 537		542 513
d(O−B−O)		711		708	
$\nu_1(BF_4^-)$			786		772 762
b(CH_2)	850			869	869
d(O−C−O)		945		982	
ν_{as}(O−B−O)		969		1002	
$\nu_3(BF_4^-)$			1010		946 969
		1025		1025	
ν_s(O−B−O)		1084		1089	
b(O−C−O)	1105			1056	1056
		1149		1140	
	1193			1193	1193
	1247			1247	1247
ν(C−O) + ν(C−C)		1268		1288	
		1307		1312	
ν(C=O)		∼1800		∼1800	
ν(C−H)	2818 2878 2923 2982			2845 2866 2896 2961	2845 2866 2910 2961

2.4 Preparation of $Ca(B(OCOCF_3)_4)_2(DME)_2$

Calcium *tetrakis*(trifluoroacetoxy)borate ($Ca(TFAB)_2$) was synthesized in a one-pot synthesis route in two steps, following a similar route reported previously for the lithium and caesium analogues [97, 98]:

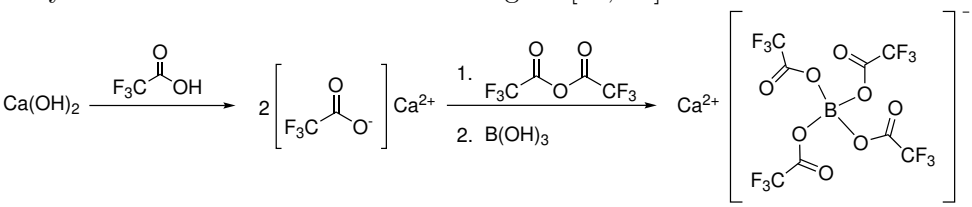

In a round-bottom flask, under an Ar protective atmosphere, and equipped with a magnetic stirrer bar, 250.8 mg (3.38 mmol) of $Ca(OH)_2$ were completely dissolved in a mixture of 8 mL of trifluoroacetic acid and 1 mL of trifluoroacetic anhydride, obtaining a completely transparent solution. 7 mL of trifluoroacetic acid and 2 mL of trifluoroacetic anhydride were again added to the reaction medium, together with 418.6 mg (6.77 mmol) of $B(OH)_3$. The boric acid was completely dissolved after one night of constant stirring producing a transparent and slightly yellow solution.

The obtained solution was completely dried under vacuum to remove the excess of solvent and unreacted anhydride. A total mass of 3.51 g of product was obtained, which was transferred to a glovebox to further purification. For purification, ∼350 mg of crude product were completely dissolved in 0.6 mL of dry DMC, 0.8 mL of DME were then added drop-wise producing a fast precipitation of a white crystalline solid. The solid was recovered, washed several times with small portions of DME, dried under vacuum, and stored inside the glovebox.

Due to the fast precipitation of the crystalline material we were unable to obtain crystals suitable for single-crystal XRD. The powder XRD diffraction pattern was measured in a sealed borosilicate capillary at ALBA Synchrotron (MSPD beamline) with an irradiation energy of 20 keV equivalent to a wavelength of 0.62 Å. The obtained difractogram is shown in Figure 2.16.

The formation of the anion can be tracked by IR spectroscopy when comparing the spectra of the starting CF_3COOH, the intermediate $Ca(CF_3COO)_2$, and the final recrystallized product (Figure 2.17). The ν C=O band undergoes the biggest shift as the coordination of the ligand changes substantially. This band, originally located at 1783 cm^{-1} in CF_3COOH, gets red shifted by about

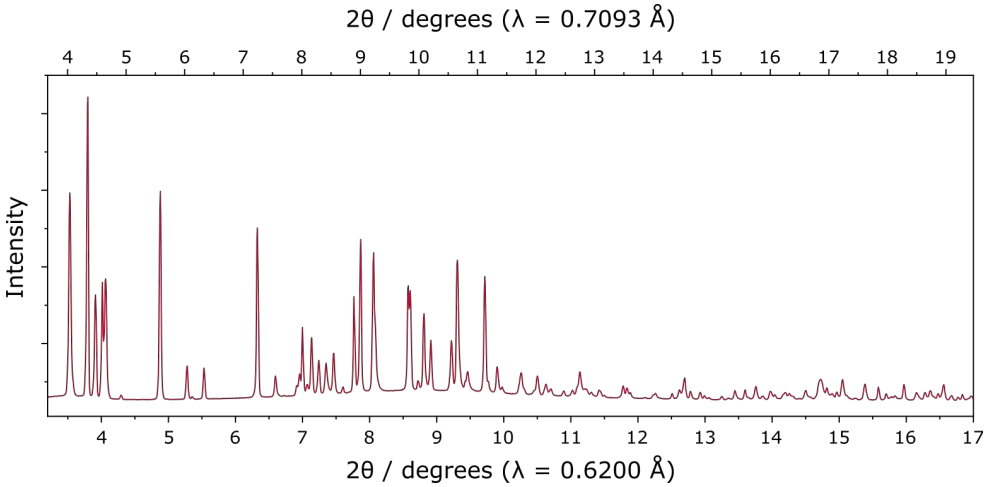

Figure 2.16: Powder XRD pattern of the purified $Ca(TFAB)_2$ salt The pattern was obtained using a 20 keV X-ray beam (λ = 0.6200 Å), the upper scale is added for comparison.

140 cm^{-1} in $Ca(CF_3COO)_2$, and then is blue shifted again to 1768 cm^{-1} in the TFAB anion. This behaviour is typically observed when carboxylate ligands change their coordination geometries, in our case the COO^- group acts as a bridge ligand in $Ca(CF_3COO)_2$ while it is a monodentate ligand to the central boron atom in TFAB anion.

The bands located between 950-1030 cm^{-1}, similar to the case of BOB anion, likely correspond to vibration modes of the B−O bonds in tetracoordinated boron. The rest of the vibration modes of the TFAB anion relate with the parent CF_3COOH and $Ca(CF_3COO)_2$ compounds and were assigned following previous reports [99, 100]: 733 cm^{-1} (d CF_3), 842 cm^{-1} (ν C−C), 1147 cm^{-1} (ν_{as} CF_3), and 1460 cm^{-1} (ν_s CO_2).

As in the case of the solvated salts reported in Section 2.3, the $Ca(TFAB)_2$ crystallizes with some DME molecules in its crystal structure. The group of bands located at 2900-3000 cm^{-1} resembles the profile observed in Figure 2.15 for DME ligands coordinated to a Ca^{2+} cation in a *trans-gauge-trans* conformation. We can anticipate, then, that the DME in this compound coordinates to the cation in a similar way, and thus the bands at 867 and 1061 cm^{-1} are attributed to the bending of CH_2 and C−O−C groups, respectively, in the DME-Ca^{2+}.

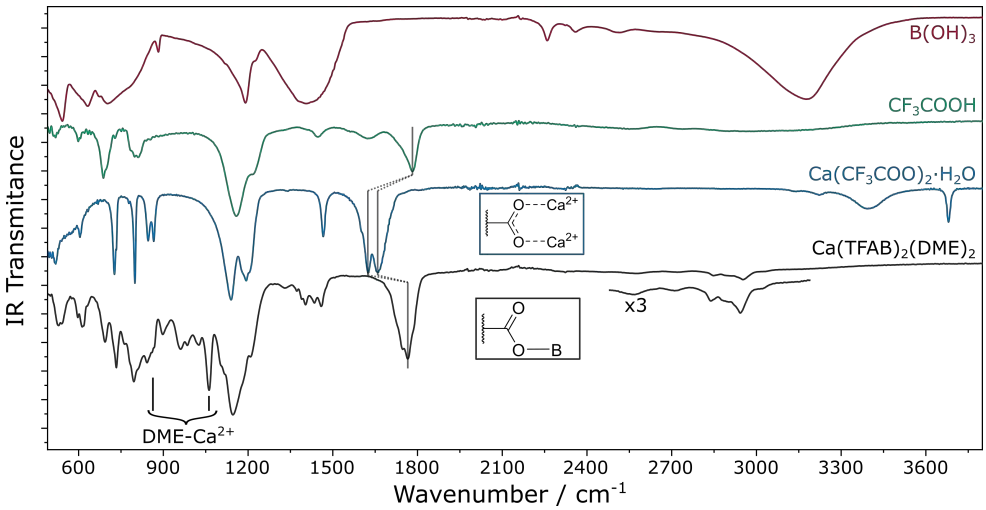

Figure 2.17: IR spectra of purified $Ca(TFAB)_2(DME)_2$ compared to $B(OH)_3$, CF_3COOH, and $Ca(CF_3COO)_2 \cdot H_2O$.

2.5 Summary and Conclusions

Evidence showing that the BF_4^- anion is prone to hydrolysis at elevated temperatures was shown, possibly promoted by the presence of Ca^{2+} cations and the formation of the very stable CaF_2. This inherent instability hinders the possibility of obtaining ultra-dry $Ca(BF_4)_2$ from the commercial hydrate salt by simple heating treatments. Alternatively, two synthetic routes were developed for the production of the anhydrous salt, and the characterization of the obtained products confirms the formation of the targeted salt. However, the use of corrosive/dangerous reagents (aHF, BF_3) may difficult its applicability in a bigger scale.

Three new solvated salts were also prepared ($Ca(BF_4)_2(DME)_2$, $Ca(BOB)_2$-$(DME)_2$ and $Ca(TFAB)_2(DME)_2$), the crystalline structure of the first two was successfully resolved by means of single-crystal XRD. The simple metathesis reaction employed for the production of $Ca(BF_4)_2(DME)_2$ and $Ca(BOB)_2$-$(DME)_2$ stands out as an easy to implement alternative for the production of water-free salts. Further studies are needed to fully evaluate the possibility of removing the crystallization solvent by thermal or vacuum methods. Although very little Li^+ contamination was detected in the two cases presented here, this is a possibility that needs to be kept in mind if the protocol intends to be expanded to bigger batch sizes or other magnesium or calcium salts.

The IR spectra of the solvated salts present particular bands assigned to solvents or anions when coordinated to Ca^{2+}, and a direct correlation was drawn between the coordination (*e.g.* monodentate *vs.* bidentate) and the position of the IR bands. Being able to determine the coordination structure of a molecule towards a cation in a coordination complex is of crucial importance as will be shown in the following chapter, dealing with solvation structure of cations in solution.

3

Physicochemical Properties of Divalent Cation Electrolytes

In this chapter, the density, viscosity, and ionic conductivity of the electrolytes are presented. The chemical structure of the different anions and solvents under study are presented in Figure 3.1. The influence of the salt choice is studied employing propylene carbonate (PC) as common solvent, given its broad liquid range and its polarity. In turn, the influence of the solvent was studied by setting $Ca(TFSI)_2$ as common salt, given its high solubility in organic solvents and its availability with high purity from commercial sources.

The temperature dependence of each of the three properties is fitted to a relevant model. Assuming that the volume of the solution expands linearly with the temperature, with a thermal expansion coefficient equal to β, the change in the density of the solution with temperature results in Equation 3.1.

$$\ln\left(\frac{1}{\rho}\right) = \ln\left(\frac{1}{\rho^*}\right) + \beta\,(T - T^*) \tag{3.1}$$

With ρ being the density of the electrolyte at a given temperature T, and ρ^* the density at a reference temperature T^*.

In the case of viscosity (η) and ionic conductivity (σ), the temperature dependence can be written according to a Vogel-Tamman-Fulcher (VTF) model as Equations 3.2 and 3.3, respectively.

$$\ln\left(\frac{\eta}{\sqrt{T}}\right) = \ln B + \frac{E_\eta}{T - T_{0,\eta}} \tag{3.2}$$

$$\ln\left(\sigma\sqrt{T}\right) = \ln A - \frac{E_\sigma}{T - T_{0,\sigma}} \tag{3.3}$$

Where A and B are pre-exponential factors, E_η and E_σ are the pseudo-activation energies for viscosity and conductivity, $T_{0,\eta}$ and $T_{0,\sigma}$ are the Vogel

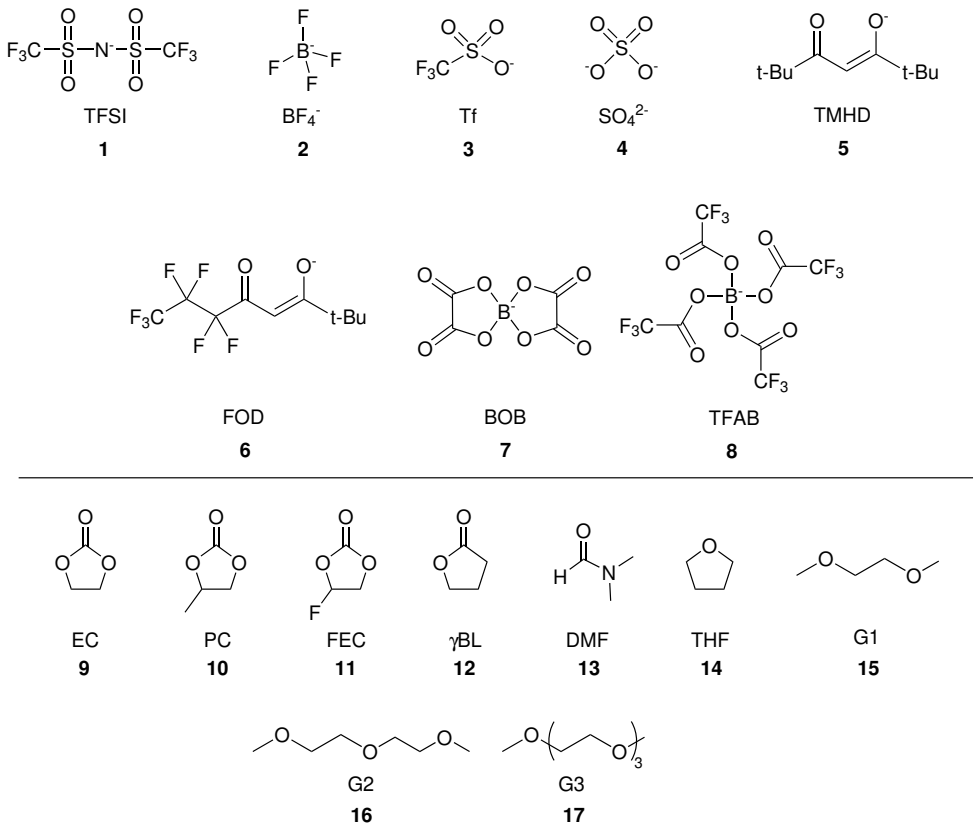

Figure 3.1: Chemical structure and acronyms of the anions and solvents studied for calcium and magnesium electrolytes. **1.** *bis*(trifluoromethylsulfonyl)imide, **2.** tetrafluoroborate, **3.** trifluoromethanesulfonate, **4.** sulfate, **5.** *2,2,6,6*-tetramethyl-*3,5*-heptanedionate, **6.** *6,6,7,7,8,8,8*-heptafluoro-*2,2*-dimethyl-*3,5*-octanedionate, **7.** *bis*(oxalato)borate, **8.** *tetrakis*(trifluoroacetoxy)borate. || **9.** ethylene carbonate, **10.** propylene carbonate, **11.** fluoroethylene carbonate, **12.** γ-butyrolactone, **13.** *N,N*-dimethylformamide, **14.** tetrahydrofuran, **15.** dimethoxyethane or monoglyme, **16.** Diethylene glycol dimethyl ether or diglyme, **17.** triethylene glycol dimethyl ether or triglyme.

temperatures for viscosity and ionic conductivity, respectively. A detailed deduction of these equations, and their relationship with the free-volume model is presented in the Section 6.8 in Chapter 6 - Experimental methods (page 124).

From the obtained fitting parameters, some trends are discussed in terms of the intermolecular interactions in the electrolyte (ion-dipole, ion-ion, dipole-dipole, etc.). Relevant comparisons with lithium and magnesium equivalent electrolytes are shown, particularly stressing the differences between monovalent and divalent cation based electrolytes. The ionicity, as a measure of free ions in solution, is discussed in the framework of the fractional Walden's rule [101]:

$$\Lambda_{eq}\,\eta^{\alpha} = C' \tag{3.4}$$

Where Λ_{eq} is the equivalent molar ionic conductivity of the solution, η is its viscosity, α is the Walden slope related to the degree of ion pairing, and C' is a constant for each electrolyte solution.

Finally, to gain deeper understanding on the molecular structure of the electrolyte solutions, an IR and Raman spectroscopic analysis is presented. From the obtained spectra, the solvation behaviour around the metal cation is obtained, and analysed considering the solvent's dielectric constant and donor numbers.

3.1 Densitometry and thermodynamic properties of electrolytes

The density of 0.1 M electrolytes in PC, using the different salts under study is presented in Figure 3.2a. Dissolving any of the salts produces an increase in the density compared to the pure solvent, the biggest change was observed in the case of $Ca(TFSI)_2$ solution, which density is 2.2% higher than the pure PC. The density increase comes together with a volume change that can be quantified by the apparent molar volume of the salt ($\widetilde{V}_i$):

$$\widetilde{V}_i = \frac{1}{c_i}\left(1 - \frac{\rho - c_i M_{W,i}}{\rho_0}\right) \tag{3.5}$$

With c_i being the molar concentration of the salt in the electrolyte, $M_{W,i}$ the molecular weight of the salt, ρ the density of the electrolyte, and ρ_0 the density of the pure solvent.

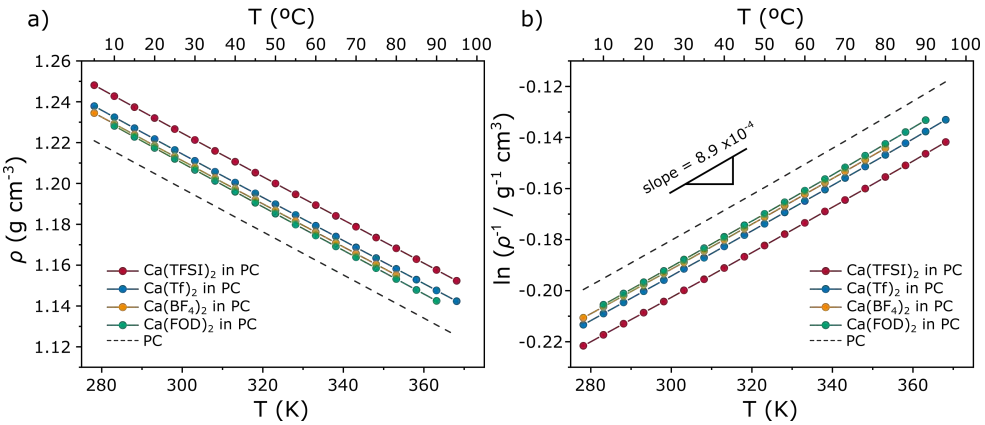

Figure 3.2: Density of studied calcium electrolytes. a) density of 0.1 M electrolytes in PC based on different calcium salts, as function of temperature. **b)** Fitting of the experimental data to the Equation 3.1, the slope represent the thermal expansion coefficient of the electrolyte.

$\widetilde{V_i}$ quantifies the volume change of a solvent when a certain amount of salt is added, so its name *apparent molar volume*, as the salt *appears* to have such volume itself. In practice, however, the apparent molar volume and the real molar volume are different, as the anion and cation are expected to interact strongly with the solvent molecules. Contrarily to the density, $\widetilde{V_i}$ varies significantly depending on the anion, being 20.26, 141.57, 274.67, and 421.55 cm^3/mol for $Ca(BF_4)_2$, $Ca(Tf)_2$, $Ca(TFSI)_2$, and $Ca(FOD)_2$, respectively, at 25 °C. As expected, the biggest apparent molar volume was found for salts containing bulky anions, such as TFSI or FOD, while the small BF_4^- anion produces only a small volume variation from the pure solvent.

The density of all electrolytes decreases with temperature, as expected from the volumetric expansion of the liquid. The thermal expansion coefficient was calculated as the slope of the linear fit of data to the Equation 3.1, as shown in Figure 3.2b. In all cases the volume of the electrolyte expands at a rate of $\sim$8.9x10^{-4} K^{-1}, with little variation between the different salts employed (Table 3.1). This little dependence is expected, given the low concentration of salt used (0.1 M) which is translated into a solvent:salt molar ratio of around 100:1. It is evident, nonetheless, that the obtained thermal expansion coefficients of the 0.1 M electrolytes is slightly lower than the one found for the pure solvent (PC), ascribed to the interaction between the ions and the solvent molecules, as will be explained later. This behaviour was also observed when comparing the $Ca(TFSI)_2$ electrolytes in γBL, and THF with their

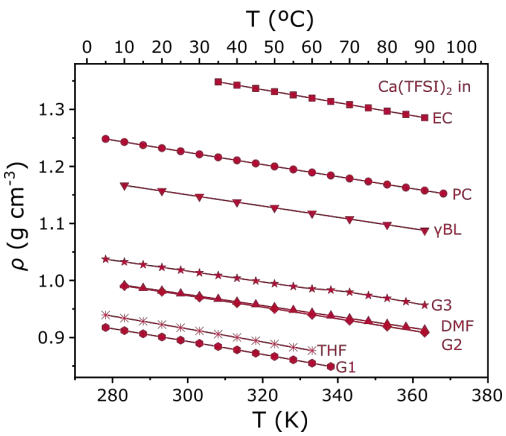

Figure 3.3: Density of 0.1 M $Ca(TFSI)_2$ electrolytes in different solvents, as function of temperature

corresponding pure solvents (β = 8.753, and 12.82 x10^{-4} K^{-1} respectively) [102].

Varying the solvent produces a great change in the density of the electrolyte, as observed in Figure 3.3, where the density of 0.1 M $Ca(TFSI)_2$ electrolytes in several solvents is plotted. The same is true for the thermal expansion coefficient which values are presented in Table 3.1, and which seems to be dependent on the chemical structure of the solvent. Electrolytes based on EC, PC and γBL have similar expansion coefficients while the low molecular weight ethers: THF and G1, resemble each other. In general, the thermal expansion coefficient is higher for low boiling-point solvents, as their intermolecular in-

Table 3.1: Thermal expansion coefficients of 0.1 M electrolytes.

Electrolyte (in PC)	β (x10^{-4} K^{-1})	$Ca(TFSI)_2$ electrolyte in	β (x10^{-4} K^{-1})
$Ca(TFSI)_2$	8.86 (± 0.02)	PC	8.86 (± 0.02)
$Ca(Tf)_2$	8.91 (± 0.02)	EC	8.67 (± 0.02)
$Ca(BF_4)_2$	8.85 (± 0.02)	γBL	8.75 (± 0.04)
$Ca(FOD)_2$	9.03 (± 0.02)	DMF	10.20 (± 0.04)
pure PC	9.04 (± 0.02)	THF	12.50 (± 0.07)
		G1	12.90 (± 0.09)
		G2	10.70 (± 0.08)
		G1	9.42 (± 0.03)

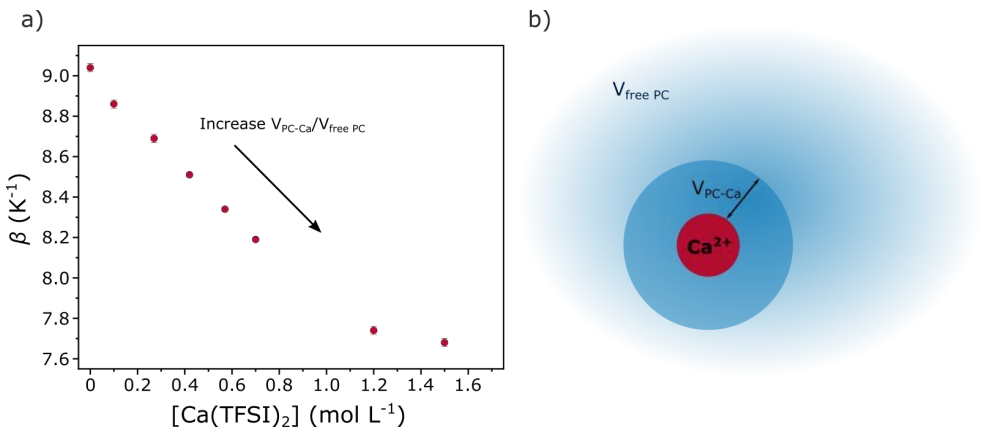

Figure 3.4: Thermal expansion coefficient (β) of Ca(TFSI)$_2$ in PC electrolytes as a function of salt concentration. **a)** evolution of β with the salt concentration, and **b)** sketch of a cation in solution depicting the difference between free and bound PC volumes.

teractions are weak and allow the molecules to distance themselves from one another.

Regarding the effect of the concentration, the β coefficient decreases monotonically from 0.1 to 0.7 M Ca(TFSI)$_2$, as shown in Figure 3.4a. Above 1.2 M, a change in the slope is observed, suggesting that β reaches a stable minimum at high concentrations. To explain this trend in the thermal expansion coefficient of the electrolyte, we can divide the PC molecules into two different volume categories (Figure 3.4b), V_{free} is the volume occupied by free PC molecules, while V_{PC-Ca} is the volume occupied by the PC molecules participating in the first solvation shell of the cation. It has been previously suggested that the solvent molecules participating in the solvation shell of a highly polarizing ion suffer from an electrostriction effect, rendering them fully compressed by the electrical forces [103]. This electrostriction effect causes a lower capacity of the V_{PC-Ca} to expand with temperature, compared to the V_{free}. Therefore, as the fraction of bounded PC increases with concentration, the overall thermal expansion coefficient of the electrolyte decreases. At concentrations above 0.7 M the fraction of free PC gets very low (as will be discussed later on in this chapter - section 3.5, page 64) causing β to stabilize.

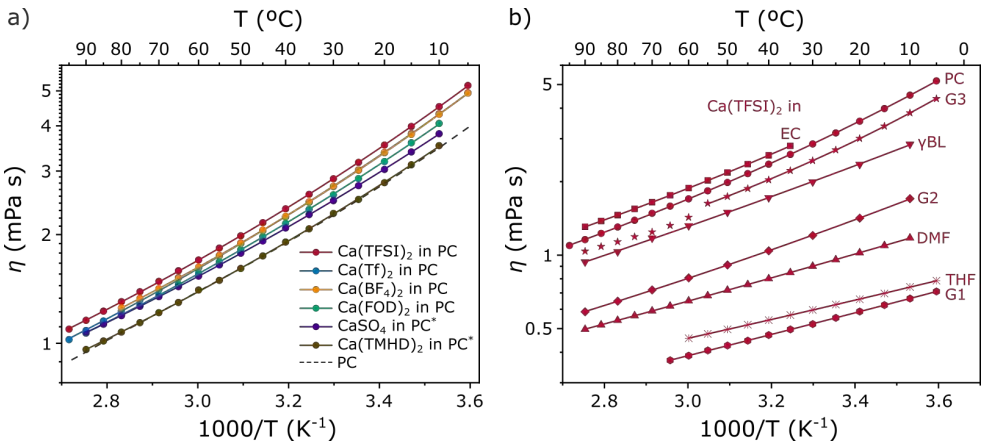

Figure 3.5: Viscosity of studied calcium electrolytes. a) viscosity of 0.1 M electrolytes of several salts in PC, *the saturated solutions of $CaSO_4$ and $Ca(TMHD)_2$ are presented as they have solubility limits below 0.1 M. **b)** viscosity of 0.1 M $Ca(TFSI)_2$ electrolytes in different solvents.

3.2 Viscosity of electrolytes

The viscosity of the electrolytes accounts for the mobility of all molecules in the liquid with respect to one another. At moderate concentration it is mostly influenced by the solvent and not by the salt. This is evident in the measured viscosity of the 0.1 M electrolytes of different salts in PC, which is only slightly higher than the one of the pure solvent (Figure 3.5a). At this point we also include saturated solutions of $CaSO_4$ and $Ca(TMHD)_2$, which saturation concentration was found to be much lower than 0.1 M.

When changing the solvent (Figure 3.5b), it is observed that the viscosity of the electrolyte follows the trend of the pure solvents, with the EC-based solutions being the most viscous and the ethers the most fluid. The continuous lines in Figure 3.5a and 3.5b correspond to the VTF model (Equation 3.2) fitted to the experimental data. The fitting parameters are presented in the Figure 3.6 and Annex C.

In the case of the G3 electrolyte, the viscosity could only be fitted by the VTF at temperatures below 60 °C, as higher temperatures produce an unexpected jump in the viscosity (see Figure 3.5b). This is not only a viscosity-related feature, but a truly structural change, as a similar discontinuity was observed also in the density and ionic conductivity (Figure 3.3b and Figure 3.9b). This feature will be discussed more deeply in Section 3.3, dealing with ionic

conductivity.

The viscosity of $Ca(TFSI)_2$ in PC electrolytes increases significantly upon increasing salt concentration, particularly at low temperatures, as shown in Figure 3.6a. The experimental data was well fitted to the VTF model, the adjusted R^2 value of the non-linear regression was above 0.9998 in all cases. The fitting parameters, together with their estimated uncertainty, are plotted in Figure 3.6b. Interpretation of the VTF fitting parameters will be done here using the free-volume theory, previously applied to the interpretation of transport properties of viscous liquids [104, 105].

Recalling, the VTF model for viscosity can be written as:

$$\ln\left(\frac{\eta}{\sqrt{T}}\right) = \ln B + \frac{E_\eta}{T - T_{0,\eta}} \tag{3.6}$$

Where the fitting parameters B, E_η, and $T_{0,\eta}$ are related to the free-volume in the fluid available for transport. More precisely, $T_{0,\eta}$ quantifies the temperature in which the free volume available for transport vanishes, while E_η ($= \gamma V_f^*/\alpha$) is related to the thermal expansion of such free-volume upon heating [105]. A more detailed derivation of the VTF model is presented in Chapter 6 - Experimental methods and data analysis, page 124.

It was found here, that the increase in the viscosity of the electrolytes at high salt concentrations is related to an increase in the Vogel temperature ($T_{0,\eta}$,

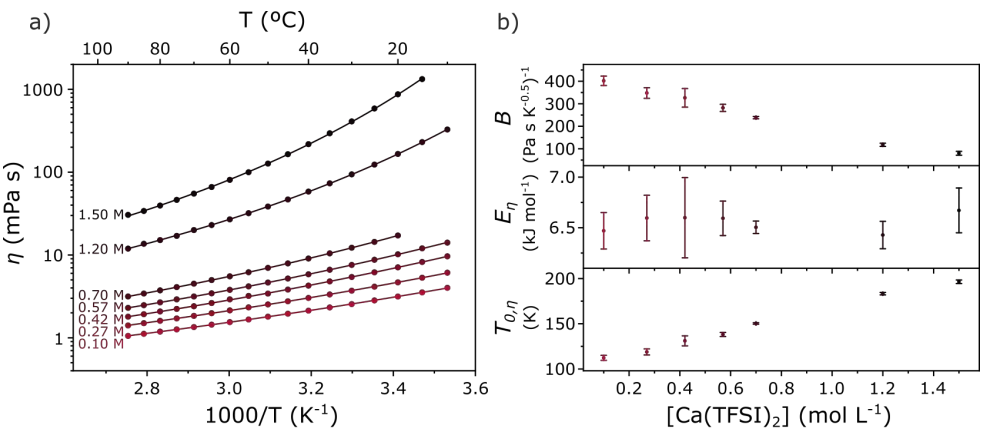

Figure 3.6: Effect of the salt concentration in the viscosity of $Ca(TFSI)_2$ in PC electrolytes. a) viscosity of the electrolytes as function of temperature, the continuous lines correspond to the fitting of the experimental data to the VTF model (Equation 3.2). **b)** VTF fitting parameters found for the different concentrations.

Figure 3.6b), implying that the free volume fraction is lower, and suggesting a higher intermolecular interaction and a lower disorder of the system. In contrast, the pseudo-activation energy, E_η, does not change across the entire concentration range, suggesting that the ratio between the critical minimum volume for transport and the thermal expansion coefficient of the free volume ($\gamma V_f^*/\alpha$)) remains constant. However, as demonstrated in Section 3.1, the thermal expansion coefficient of the electrolyte actually decreases at higher salt concentrations, which suggests that γV_f^* should increase at the same rate. The higher γV_f^*, deduced here for electrolytes containing high salt concentration, corroborates the fact that more intermolecular interactions are present in the electrolyte when more salt is present and will be further studied in the following sections.

3.3 Ionic conductivity of electrolytes

Contrarily to the viscosity, which is affected by the transport of all molecules in the electrolyte, the ionic conductivity only accounts for the mobility of charged species, and is greatly influenced by the choice of the salt. The ionic conductivity of 0.1 M electrolytes in PC of different calcium salts is shown in Figure 3.7.

The obtained conductivities can be understood in the light of the concentration of charge carriers in solution. TFSI, BF_4^-, and Tf, produce solutions with high concentration of charge carriers resulting in conductivities above 1 mS cm^{-1}. On the other hand, the FOD anion interacts more strongly with the calcium cations, probably due to the bidentate 1,3-diketone group (Figure 3.1). This stronger interaction diminishes the concentration of charge carriers and the ionic conductivity drops to 0.1-0.3 mS cm^{-1}. In the case of SO_4^{2-} and TMHD, the cation-anion interaction is strong enough to prevent salt dissociation, and ionic conductivities in the μS/cm range are recorded. These results highlight the importance of employing weakly-coordinating anions in battery electrolytes, particularly in multivalent systems where the charge density of the cations promotes a stronger interaction with the anions.

The solvated salts described in Chapter 2 were also characterized, using PC as electrolyte solvent in all cases, their ionic conductivities are shown in Figure 3.7b. The electrolytes with the solvate $Ca(BF_4)_2(G1)_2$ does not have a significantly different ionic conductivity than the equivalent $Ca(BF_4)_2$, suggesting that the presence of such small amount of G1 as cosolvent in the electrolyte

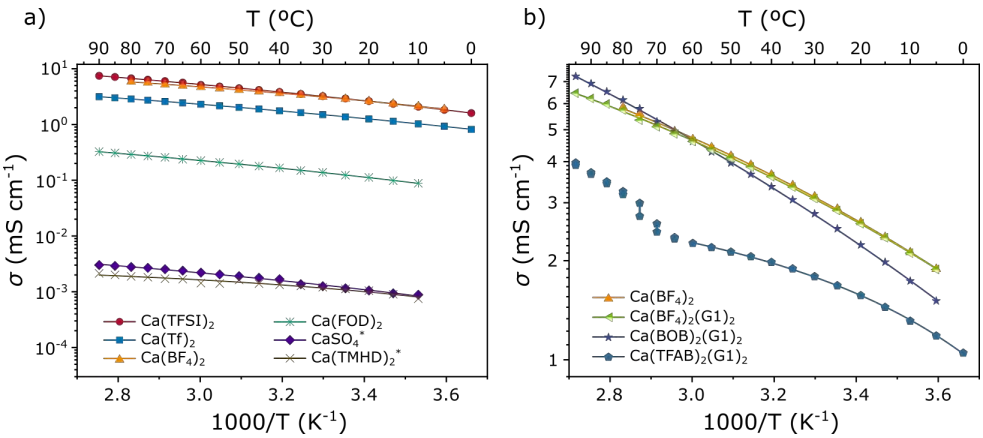

Figure 3.7: Ionic conductivity of electrolytes of different calcium salts in PC. **a)** Ionic conductivity of 0.1 M electrolytes of several salts in PC. *the saturated solutions of $CaSO_4$ and $Ca(TMHD)_2$ are presented as they have solubility limits below 0.1 M. **b)** Ionic conductivity of 0.1 M solutions of solvate salts prepared in Chapter 2. The data for $Ca(BF_4)_2$ in PC is the same in both panels.

does not affect the ionic conductivity. Comparatively, the $Ca(BOB)_2(G1)_2$ electrolyte has only slightly lower ionic conductivity at room temperature but higher at temperatures above 60 °C. In contrast, the presence of carbonyl groups in the chemical structure of the TFAB anion increases the interaction with Ca^{2+}, as clearly observed in the optimized chemical structure of the Ca^{2+}-TFAB ion pair, calculated by Dr. Piotr Jankowski from the Technical University of Denmark by DFT methods (M06−2X/6−311++G(d,p) level, Figure 3.8) which results in an interaction energy as high as 1225 kJ mol^{-1}, comparatively, the cation-anion interaction for a Ca^{2+}-TFSI pair was calculated as 1136 kJ mol^{-1} [106]. This favourable coordination produces electrolytes with lower ionic conductivities, although it still results in higher ionic conductivity as compared with $Ca(Tf)_2$-based electrolyte. The $Ca(TFAB)_2$ electrolyte, additionally, shows a drift in the ionic conductivity at temperatures above 60 °C probably related to a decomposition of the anion, further supported by the evidence of a yellow coloration at the end of the measurement.

The continuous lines in Figure 3.7 correspond to the best fit of the experimental data to the VTF equation (Equation 3.3). From the obtained fitting parameters (Table 3.2), it is possible to compare the different electrolytes. For example, the pre-exponential factor, A, gives indirect information about the charge carrier concentration in solution. As described before, the weakly

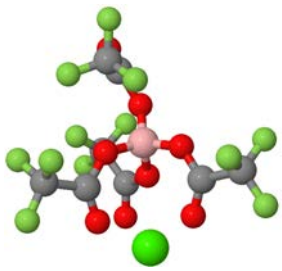

Figure 3.8: Optimized structure of a Ca^{2+}-TFAB ion pair. The structure highlights the preferable interaction between the carbonyl oxygens and the Ca^{2+} cation. Carbon atoms are shown in grey, oxygen in red, boron in pink, fluorine in dark green and calcium in bright green.

Table 3.2: VTF-conductivity fitting parameters of 0.1 M electrolytes based on different Ca-salts.

0.1 M Electrolyte in PC	A (S $K^{0.5}$ cm^{-1})	E (K)	E (kJ mol^{-1})	$T_{0,\sigma}$ (K)
$Ca(TFSI)_2$	2.58 (± 0.26)	708.2 (± 39.4)	5.9 (± 0.3)	118.3 (± 5.3)
$Ca(BF_4)_2$	1.02 (± 0.12)	467.9 (± 39.6)	3.9 (± 0.3)	143.1 (± 6.9)
$Ca(Tf)_2$	0.79 (± 0.03)	634.8 (± 15.8)	5.3 (± 0.1)	117.2 (± 2.4)
$Ca(FOD)_2$	0.10 (± 0.01)	659.2 (± 56.5)	5.5 (± 0.5)	126.9 (± 8.1)
*$Ca(TMHD)_2$	0.00012 (± 0.00005)	179.9 (± 97.0)	1.5 (± 0.8)	198.5 (± 30.2)
*$CaSO_4$	10.0009 (± 0.0004)	582.2 (± 190.2)	4.8 (± 1.6)	138.8 (± 28.7)
$Ca(BF_4)_2(G1)_2$	1.02 (± 0.08)	480.7 (± 27.0)	4.0 (± 0.2)	139.6 (± 4.9)
$Ca(BOB)_2(G1)_2$	13.02 (± 0.36)	774.6 (± 48.2)	6.4 (± 0.4)	115.8 (± 6.1)
$Ca(TFAB)_2(G1)_2$	0.095 (± 0.003)	97.9 (± 4.6)	0.8 (± 0.1)	215.9 (± 1.8)

coordinating anions produce solutions with higher A values, and therefore higher charge carrier densities. Trends in the pseudo-activation energy, E_σ, or the Vogel temperature, $T_{0,\sigma}$, between the different salts are less evident and their physical origin is not straightforward.

To study the effect of the electrolyte solvent, the ionic conductivity of 0.1 M $Ca(TFSI)_2$ in several solvents was measured (Figure 3.9). All the high polarity solvents, as PC, EC, DMF and γBL, produce electrolyte solutions with high ionic conductivities by allowing an effective cation-anion dissociation (Figure 3.9a). Solutions based on ethereal solvents, as THF or glymes, have slightly lower ionic conductivities which are attributed preliminary to a less efficient ion-ion separation (Figure 3.9b).

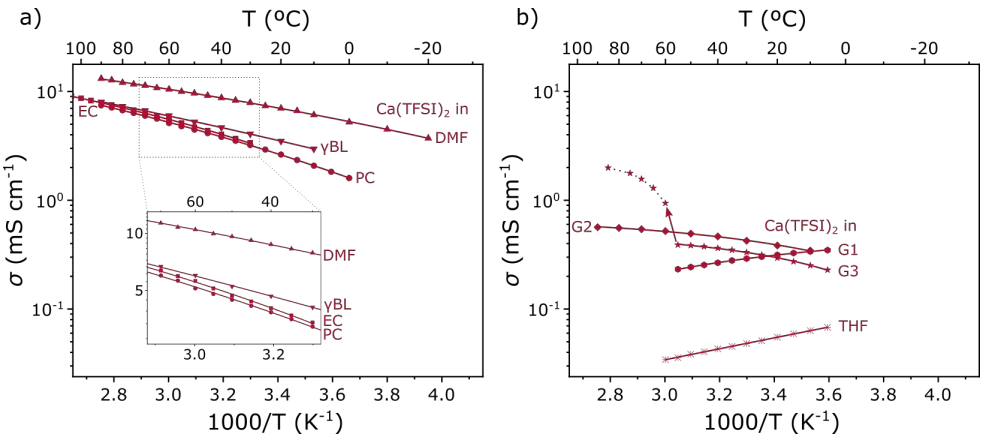

Figure 3.9: Ionic conductivity of $Ca(TFSI)_2$ electrolytes in different solvents. **a)** Ionic conductivity of 0.1 M $Ca(TFSI)_2$ electrolytes in DMF, γBL, EC, and PC. An inset is included for better clarity. **b)** Ionic conductivity of 0.1 M $Ca(TFSI)_2$ electrolytes in G1, G2, G3, and THF. The discontinuity in the G3 electrolyte is discussed in the text.

Electrolytes based on THF and G1 show a decrease in the ionic conductivity with temperature, which is an opposite behaviour than the other electrolytes studied here. A similar behaviour was reported previously for $LiBF_4$ electrolytes in low permittivity solvents [107], but its origin is still uncertain. By analysing the limiting ionic molar conductivity of the solutions and calculating the association constant between cation and anion, Barthel et al. suggest that the fraction of ion pairs and aggregates decreases at high temperatures which wouldn't explain the trend in conductivity [107]. However, more recent spectroscopic evidence contradicts this, suggesting that a higher cation-anion interaction exist at higher temperatures, at least for Li^+-based THF electrolytes [108].

Aside from the formation of ion-pairs and aggregates, a second hypothesis to explain the decrease in ionic conductivity with temperature could be related with the second and third solvation shells of the cations. Indeed, we hypothesize that a solvent with low permittivity, such as THF and DME, can form multi-layered solvation shells which arrangement can impact greatly the macroscopic properties, as observed before [109, 110]. In this respect, previous reports on the $Ca(TFSI)_2$-DME and $Ca(TFSI)_2$-THF systems have suggested that there is a significant interaction between TFSI and Ca^{2+} in solution, with some bidentate coordination from the TFSI [111]. Then, the presence of contact and solvent-separated ion pairs is expected to modulate the ionic conductivity of the electrolyte in the 0.1-0.5 M concentration range

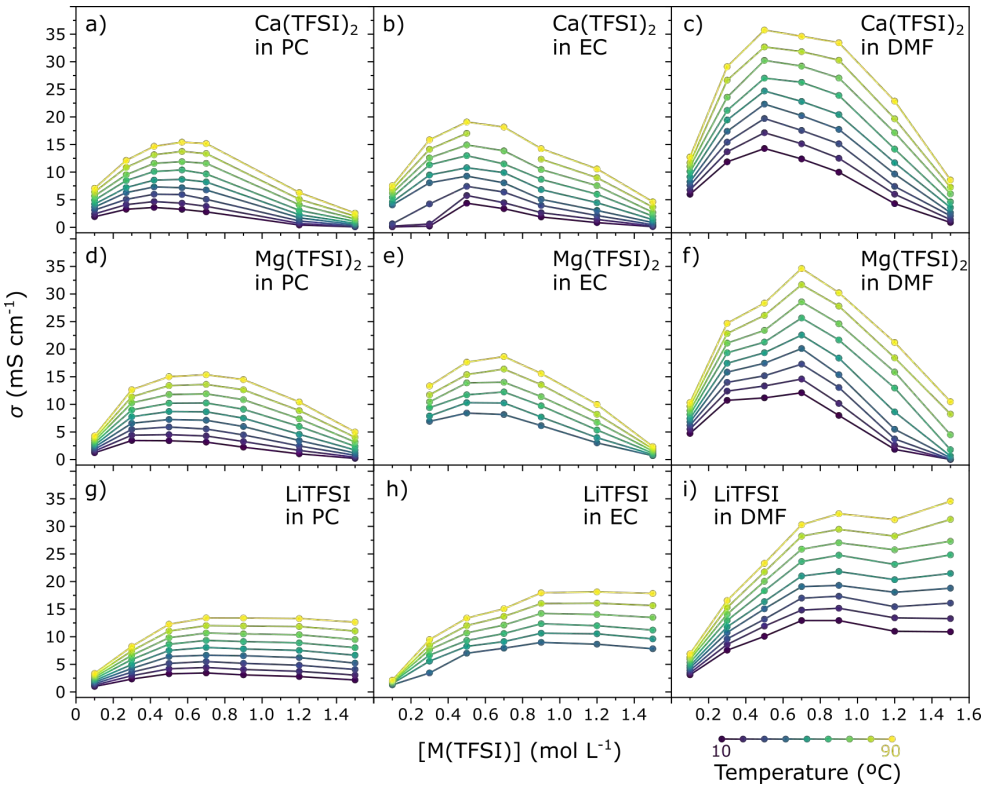

Figure 3.10: Ionic conductivity of $Ca(TFSI)_2$, $Mg(TFSI)_2$, and LiTFSI electrolytes as function of concentration and temperature. Comparison between PC **(a, d, g)**, EC **(b, e, h)**, and DMF **(c, f, i)** used as solvent. The temperature colour scale is shown in the bottom right.

[112]. Despite this findings, a temperature-dependent investigation on the solvation structure of Ca^{2+} in THF and DME is still lacking.

Lastly, in the $Ca(TFSI)_2$ electrolytes in G3, we observed a jump in the ionic conductivity at temperatures around 60 °C. This jump in conductivity is accompanied by a similar discontinuity in density and viscosity data (Figures 3.2b and 3.5b). As the three physicochemical properties are measured independently, we suggest this behaviour is a real feature of the $Ca(TFSI)_2$ electrolyte in G3 and not an artefact of the measurement. Since the low conductivity regime was not recovered by cooling back the electrolyte these results suggest the occurrence of an irreversible process at about 60°C affecting the physicochemical properties of the electrolyte.

To study the effect of the salt concentration in the ionic conductivity of the electrolyte, only the high permittivity solvents were considered (PC, EC, and

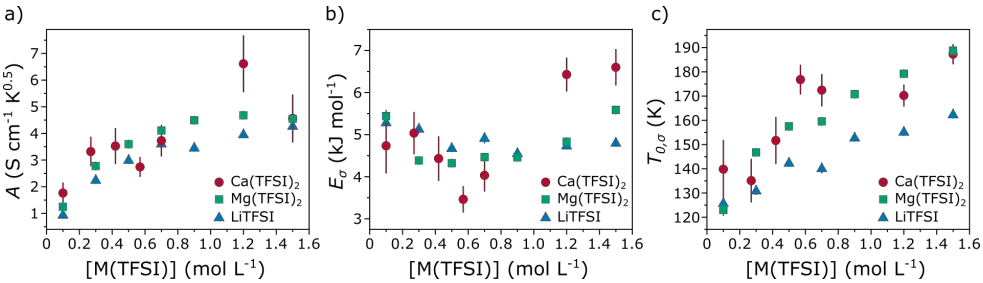

Figure 3.11: VTF fitting parameters for ionic conductivity of $Ca(TFSI)_2$, $Mg(TFSI)_2$, and LiTFSI electrolytes in PC as function of concentration. a) Pre-exponential factor, **b)** pseudo-activation energy, and **c)** Vogel temperature for conductivity. Error bars in each case represent the error in the parameter estimation.

DMF). The conductivity of $Ca(TFSI)_2$ electrolytes in the three selected solvents, as a function of temperature and concentration, is shown in Figure 3.10. For comparison, the ionic conductivity of equivalent electrolytes using $Mg(TFSI)_2$ and LiTFSI were also measured. In all electrolytes under study, the ionic conductivity initially increases with the concentration, until a maximum is reached. The presence of a maximum in the ionic conductivity is a common feature in electrolyte solutions and is the result of a competition between the increasing number of charge carriers and the increase in the viscosity and interionic interactions as the concentration increases [113]. In the case of divalent cation electrolytes, the maximum ionic conductivity is reached at concentrations around 0.4-0.6 M, somewhat lower than for LiTFSI electrolytes which maximum in ion conductivity observed typically around 1 M [114]. In all cases the concentration of maximum conductivity moves to higher values by increasing the temperature, as a result of a decrease in the viscosity.

The molecular origin of the ionic conductivity maxima can be visualized by fitting the evolution of the ionic conductivity with temperature for each concentration under study. The values of the three VTF fitting parameters for each concentration of $Ca(TFSI)_2$, $Mg(TFSI)_2$ and LiTFSI electrolytes in PC are shown in Figure 3.11. The maximum of ionic conductivity is related in the three cases with a minimum in the pseudo-activation energy (E_σ), after which the formation of ion pairs would hamper the ionic mobility. Both $T_{0,\sigma}$, and A, increase steadily with the salt concentration. In the case of the Vogel temperature, $T_{0,\sigma}$, this increase is related to a decrease in the fraction of free volume, which is the result of the constant increase of charge species in solution.

3.4 Ionicity and Walden plot analysis

While viscosity, in general, limits ion motion in electrolytes, intermolecular and electrostatic interactions are also important as they affect the nature of the diffusing species (free ions, ion-pairs, etc.) and their relative concentration. All of these interactions are taken into account in the ionicity of the electrolyte within the framework of the empirical Walden's rule [101]. While originally formulated for infinitely diluted aqueous electrolytes with solvated ions of the same radius, its use has been extended to study properties of nonideal, nonaqueous electrolytes [114, 115].

In a Walden plot, the logarithm of the equivalent conductivity, Λ_{eq}, is plotted against the fluidity, *i.e.*, the inverse of the viscosity, $1/\eta$. A straight line with slope equal to 1 and intercept at $(0, 0)$ is often included as reference, although its physical meaning is questionable [116, 117]. The relationship between limiting equivalent conductivity and viscosity can be expressed as:

$$\Lambda^0_{eq}\eta = k = \frac{e_0 F}{6\pi}\frac{1}{R_+ + R_-} \tag{3.7}$$

Where e_0 is the elementary charge, F is the Faraday's constant, and R_i is the Stokes radius of the ion. The expression for the constant k was directly derived from the definitions of ionic conductivity and viscosity using Nernst-Einstein equations. Note that here, the equivalent ionic conductivity is used instead of the molar ionic conductivity, as the former accounts for the number of charges released by mole of salt ($\Lambda_{eq} = \sigma/zc_i$) and can be compared between 1:1 and 1:2 electrolytes. The obtained Walden plots for 0.1 M electrolytes in PC employing the salts under study are shown in Figure 3.12.

The ideal Walden rule (Equation 3.7) is valid for strong electrolytes at infinite dilution, where the mobility of ions is supposed to be entirely limited by the viscosity of the medium, *i.e.* the friction between molecules, and no interionic interactions are present. Other authors have extended the use of the Walden rule to non-diluted systems, as ionic liquids of molten salts. To account for deviations from the ideal case, an exponent α can be included resulting in the fractional Walden rule [118, 119]:

$$\Lambda^0_{eq}\eta^\alpha = C' \log \Lambda_{eq} = \log C' + \alpha \log\left(\eta^{-1}\right) \tag{3.8}$$

MacFarlane et al. have estimated the ionicity in ionic liquids using Walden plots, but an adjustment is necessary to account for the effective ionic radii,

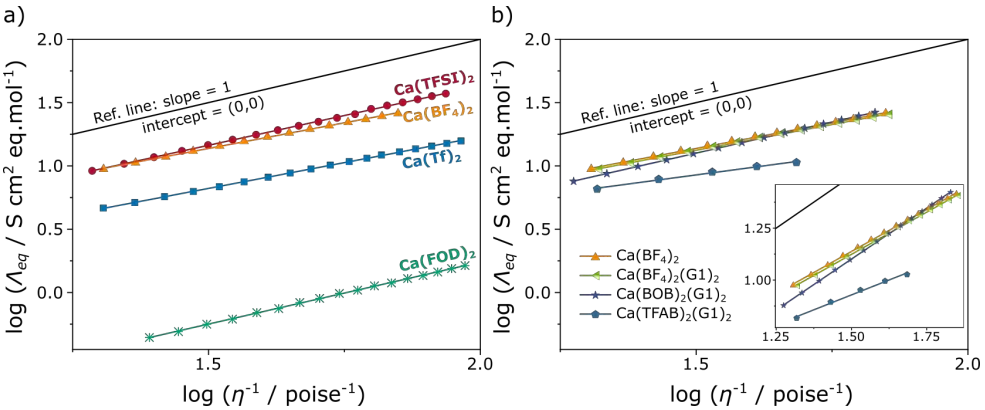

Figure 3.12: Walden plots of 0.1 M calcium electrolytes in PC. a) electrolytes based on commercially available salts, and **b)** electrolytes from salts prepared in-house.

which will have an important influence in the conductivity, as deduced from Equation 3.7 [120]. As the ionic radii in the electrolytes studied here is, in principle, not known, this adjustment cannot be performed, preventing a direct evaluation of the ionicity by a simple comparison with the reference line. An alternative for the estimation of ionicity is based on the measurement of the diffusion coefficient of the different ions in the electrolyte [121], although this method cannot be applied here, as the only NMR-active Ca-isotope (^{43}Ca) is not abundant enough to allow the straightforward NMR study.

In this study, then, we have decided to adjust the temperature-dependent viscosity and ionic conductivity data to the Equation 3.8 for all the electrolytes, and compare the fitting parameters: C' and α, which will also carry information about the ionicity of the solution. For example, contrarily to ionic liquids, the conductivity of common organic electrolytes is always limited by the viscosity, and thus the slope of the Walden plot, α, is necessarily below 1. Furthermore, the increase in ion pairing further hampers the mobility of charge species producing a decrease in the slope [119]. Previously, the slope α has also been associated with the ratio between the activation energy for viscosity (E_η) and the activation energy for conductivity (E_σ), calculated from Arrhenius or VTF fittings [118].

The obtained slope for different electrolytes follow the expected ionicity trend, with the highest slope calculated for the $Ca(BOB)_2(G1)_2$ electrolyte (α = 0.98) given its lower tendency to associate with cations in solution [122]. The order continues with the $Ca(TFSI)_2$ electrolyte (α = 0.94) followed by

$Ca(BF_4)_2$ and $Ca(Tf)_2$, both with $\alpha = 0.81$. Curiously, the $Ca(FOD)_2$-based electrolyte has a slope of 0.98 despite the low values of ionic conductivity found experimentally. On the other hand, the intercept of linear regression allows to calculate the C' parameter, which is inversely proportional to the effective ionic radii of the moving ions. Indeed, the obtained C' for the FOD-based electrolyte is the lowest among all, agreeing with its big size. A summary of the obtained α and C' parameters found for the 0.1 M solutions of the different salts in PC is presented in Table 3.3.

Table 3.3: Fractional Walden rule fitting parameters of 0.1 M electrolytes based on different Ca-salts.

Electrolyte (in PC)	α	C'
$Ca(TFSI)_2$	0.941 (± 0.004)	0.564 (± 0.009)
$Ca(BF_4)_2$	0.810 (± 0.006)	0.836 (± 0.019)
$Ca(Tf)_2$	0.815 (± 0.003)	0.397 (± 0.004)
$Ca(FOD)_2$	0.979 (± 0.005)	0.019 (± 0.001)
$Ca(BF_4)_2(G1)_2$	0.813 (± 0.006)	0.803 (± 0.018)
$Ca(BOB)_2(G1)_2$	0.981 (± 0.001)	0.425 (± 0.003)
$Ca(TFAB)_2(G1)_2$	0.574 (± 0.027)	1.172 (± 0.112)

The parameters found for the $Ca(TFAB)_2(G1)_3$-based electrolyte do not seem to agree with its expected behaviour. As mentioned before, this electrolyte displays a low ionic conductivity given the higher tendency of the anion to interact with Ca^{2+}, decreasing the ionicity ($\alpha = 0.57$). However, this electrolyte present a significantly higher C', corresponding to very small ionic radius, but disagreeing with the real structure of the TFAB anion. A deeper study on this electrolyte is needed to understand this phenomenon.

A similar ionicity analysis can be performed for 0.1 M $Ca(TFSI)_2$ electrolytes in various solvents (Figure 3.13 and Table 3.4). The solutions in EC, PC, γBL, and DMF follow all a linear behaviour corresponding to Equation 3.8. The highest ionicity is observed in the EC-based electrolyte ($\alpha = 1.00$), while DMF displays the lowest ($\alpha = 0.87$).

The low permittivity solvents, as G1, G2, or G3, behave significantly different. At low temperatures the data tends to a linear relation, with $\alpha = 0.67$ for G3 and $\alpha = 0.59$ for G2. As the temperature increases, however, a clear deviation is observed resulting in even lower slopes. This dependence of the α parameter to the temperature indicates a strong correlation between the

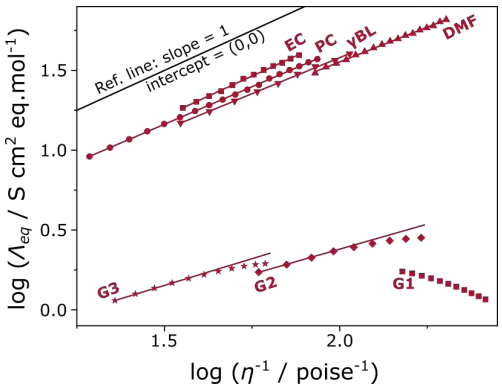

Figure 3.13: Walden plots of 0.1 M Ca(TFSI)$_2$ electrolytes in different solvents.

temperature and the ion pair formation in these electrolytes. The effect is even stronger in the case of G1 electrolytes, producing a negative slope in the Walden plot (Figure 3.13).

Table 3.4: Fractional Walden rule fitting parameters of 0.1 M Ca(TFSI)$_2$ electrolytes in different solvents.

	α	C'
EC	1.007 (± 0.012)	0.504 (± 0.024)
PC	0.941 (± 0.004)	0.564 (± 0.009)
γBL	0.903 (± 0.009)	0.594 (± 0.022)
DMF	0.872 (± 0.008)	0.642 (± 0.025)
G3 (at low T)	0.675 (± 0.009)	0.138 (± 0.004)
G2 (al low T)	0.598 (± 0.010)	0.150 (± 0.007)

A constant decrease in the α parameter is observed when the salt concentration increases from 0.1 M to 1.5 M for Ca(TFSI)$_2$, Mg(TFSI)$_2$ and LiTFSI (Figure 3.14) as a result of increasing ion pairing and decreasing ionicity. However, the values obtained for the different salts couldn't be directly compared; similar values for α were observed for 0.7 M solutions of the different cations even when the divalent cations are expected to interact more readily with the anions in solution than the monovalent cations. This results highlight the fundamental differences in the ionic behaviour between monovalent cation and divalent cation electrolytes.

Just to illustrate this point, consider the differences between the speciation of a LiTFSI and a Ca(TFSI)$_2$ electrolyte in a polar solvent. At sufficiently

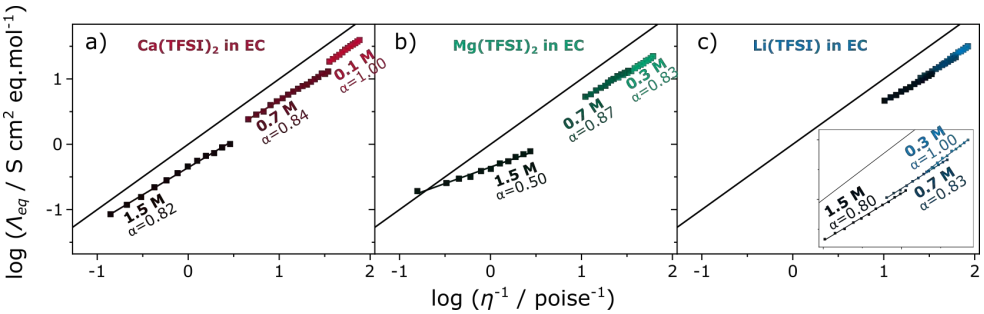

Figure 3.14: Walden plots of calcium, magnesium and lithium electrolytes in EC with different concentrations. a) $Ca(TFSI)_2$ in EC, **b)** $Mg(TFSI)_2$ in EC, and **c)** LiTFSI in EC.

low concentrations the salts will be completely dissociated:

$$\mathrm{LiTFSI} \longrightarrow \mathrm{Li^+} + [\mathrm{TFSI}]^-$$
$$\mathrm{Ca(TFSI)_2} \longrightarrow \mathrm{Ca^{2+}} + 2\,[\mathrm{TFSI}]^-$$

By increasing the concentration of the solution, some fraction of the ions will form ion pairs:

$$\mathrm{Li^+} + [\mathrm{TFSI}]^- \longrightarrow [\mathrm{Li{-}TFSI}]^0$$
$$\mathrm{Ca^{2+}} + [\mathrm{TFSI}]^- \longrightarrow [\mathrm{Ca{-}TFSI}]^+$$

The Li-TFSI ion pair results in a neutral complex which does not participate in the conduction of charge and diminishes the ionicity. The Ca-TFSI pair, on the contrary, is charged and will continue to account in the ionic conductivity. Even in the case when all cations get into ion pairs, the divalent electrolyte would still be able to conduct charge as a monovalent: $\mathrm{Ca(TFSI)_2} \longrightarrow [\mathrm{Ca{-}TFSI}]^+ + [\mathrm{TFSI}]^-$. An interesting case of study, which is left open for the future, would be to analyse the Walden plot and the ionicity of an electrolyte containing a divalent cation and a divalent anion.

3.5 Spectroscopic study of ion pairing in solution

To study the cation-solvent and the cation-anion interactions we turn to vibrational spectroscopy, which allows to assess the local coordination in more detail. As it will be shown in this section, by following the evolution of several IR and Raman active modes at different concentrations, an estimation of the solvation number around the metal cation can be obtained. As the shifts in

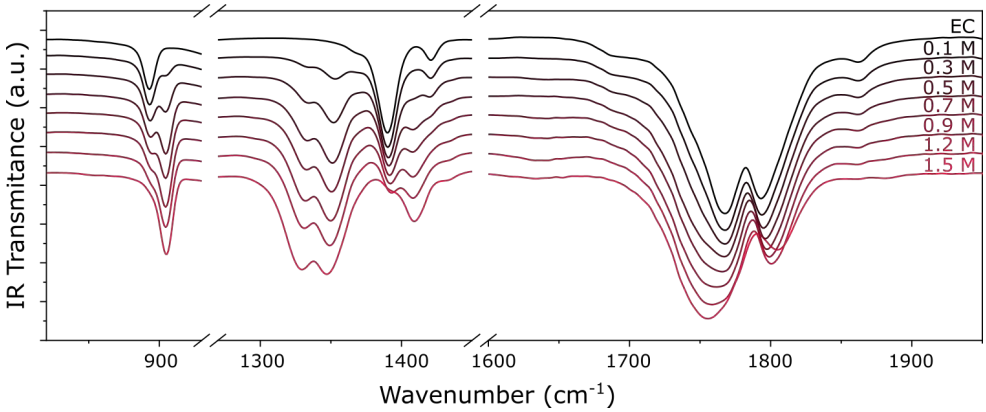

Figure 3.15: Selected IR bands of 0.1-1.5 M $Ca(TFSI)_2$ in EC electrolytes.

the IR and Raman bands is more evident when a direct contact exists between the cation and the ligand (either solvent or anion), this spectroscopic approximation is particularly suitable to study the first solvation shell in solution while is not very sensitive for solvent-separated ion pairs, for example.

First, interesting IR and Raman bands were defined to assess the solvent-cation interaction. Given that the carbonyl oxygen in EC, PC and DMF solvents has the highest Lewis base character, it is expected to be involved in the coordination of cations in solution. Furthermore, as the C=O stretching mode displays a very strong absorption band in infrared, it would make an ideal probe to study the cation solvation.

Unfortunately, for cyclic carbonates, the presence of a Fermi resonance phenomenon prevents any straightforward analysis. The Fermi resonance effect in EC has been extensively studied [123, 124], it is the result of the strong coupling between the fundamental stretching frequency of C=O (ν_2) at 1793 cm^{-1} with the first overtone of the skeletal breathing of the ring ($2\nu_7$), producing an intense band at 1767 cm^{-1} (Figure 3.15). Upon coordination with a cation, these bands shift due to different mechanisms: *i.* losing the Fermi coupling condition would produce a blueshift of the C=O stretching, moving towards the "unperturbed" frequency (gas-phase IR *ca.* 1870 cm^{-1} [125]); *ii.* decreased electron density of the C=O bond would produce a redshift of the vibration, and/or reduced its intensity; and *iii.* the decoupling between the two bands produces a redshift of the $2\nu_7$ overtone. This complex combination of mechanisms prevents any unambiguous use of the carbonyl region.

Instead, the out-of-phase wagging of the CH_2 groups (ν_{15}, 1390 cm^{-1}) and

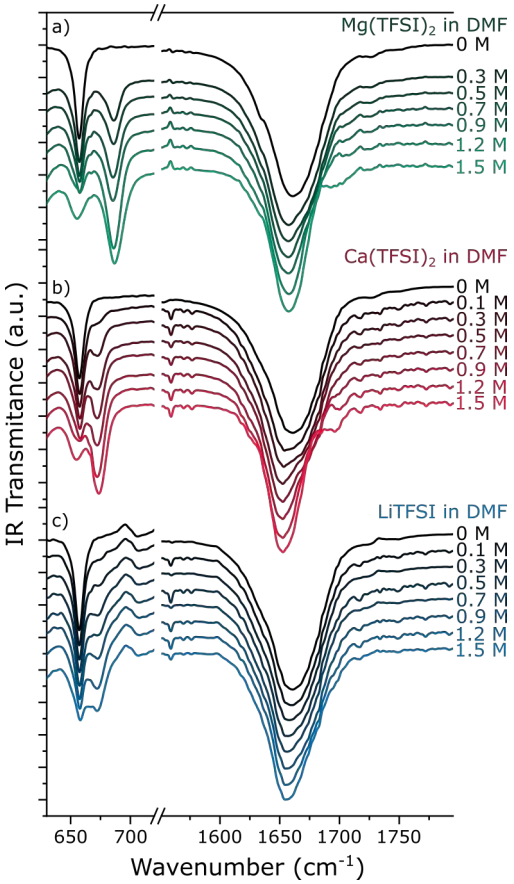

Figure 3.16: Selected IR bands of 0.1-1.5 M $Mg(TFSI)_2$, $Ca(TFSI)_2$, and LiTFSI in DMF electrolytes

the fundamental skeletal breathing of the ring (ν_7, 892 cm^{-1}) are used. Both bands shift to higher wavenumbers as the Ca-salt concentration increases (Figure 3.15). At 1.5 M, these free solvent bands are almost gone, suggesting that almost all EC molecules are coordinated by the Ca^{2+} cations. Considering that for lithium electrolytes, free EC is found at 1.8M [117] points at the Ca^{2+} cations having a larger first solvation shells (containing more solvent molecules).

The carbonyl region of the IR spectra of PC-based electrolytes is laden with the same problems as those for EC, but with the additional disadvantage that the chiral nature of PC produces, in general, broader bands [126]. For the PC electrolytes, we discern that the same modes are affected by Ca^{2+} coordination, but the shifts are not sufficiently large to allow us to correctly determine the contributions from free and coordinated PC, respectively.

In the case of DMF electrolytes (Figure 3.16), the C=O stretching mode gets

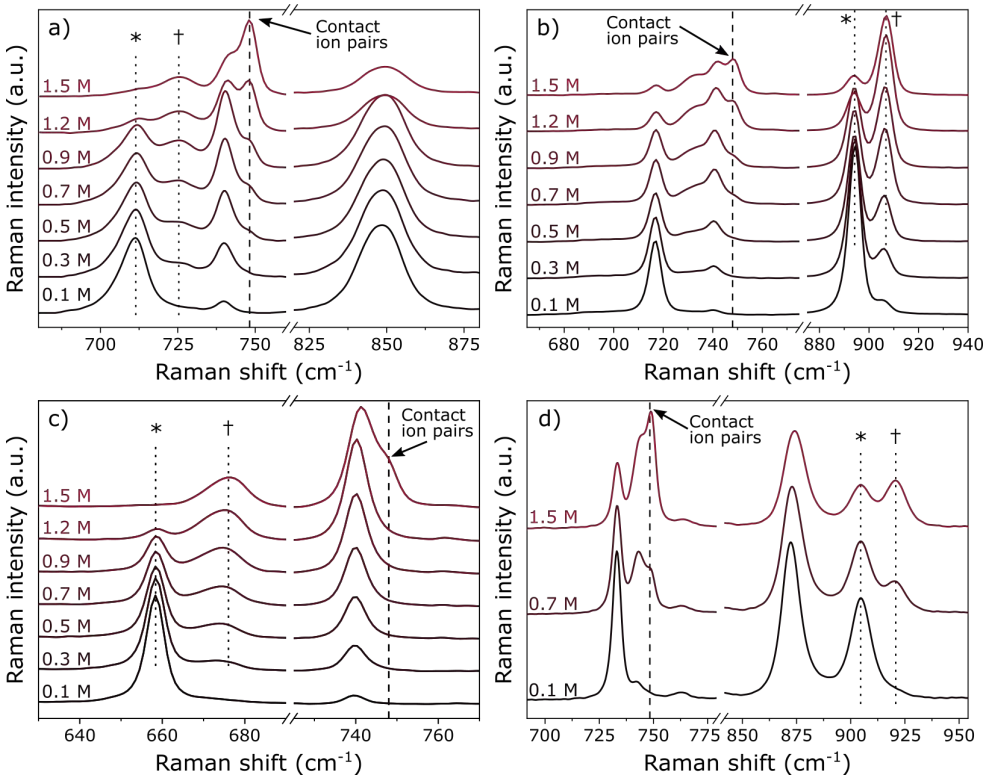

Figure 3.17: Raman spectra of $Ca(TFSI)_2$ electrolytes in different solvents as function of salt concentration. a) $Ca(TFSI)_2$ in PC, **b)** $Ca(TFSI)_2$ in EC, **c)** $Ca(TFSI)_2$ in DMF, and **d)** $Ca(TFSI)_2$ in FEC. *denotes a Raman band assigned to free solvent while † denotes Ca^{2+}-coordinated solvent. The band assigned to cation-anion contact ion pairs appears in all cases at 748 cm^{-1} and that of free TFSI at 740 cm^{-1}.

clearly shifted toward lower wavenumbers upon coordination by Li^+, Mg^{2+}, or Ca^{2+}. However, the O=C−N bending at 658 cm^{-1} is a better option to analyse the cation-DMF interaction, with a significantly larger shift obtained for the Mg^{2+} electrolyte. The larger shift is attributed to the more polarizing character of the magnesium cation, resulting in a tighter first solvation shell. This is the first evidence we have that points to a significant difference in the strength of the cation-solvent interaction, which is then expected to influence the desolvation kinetics of the different cations at an electrode surface.

For the cation solvation number determination, we turn to Raman spectroscopy and a few relatively intense bands for each solvent, which are minimally affected by other vibration modes but highly sensitive to cation coordination (Figure 3.17): ring breathing mode for EC (at 894 cm^{-1}), C=O

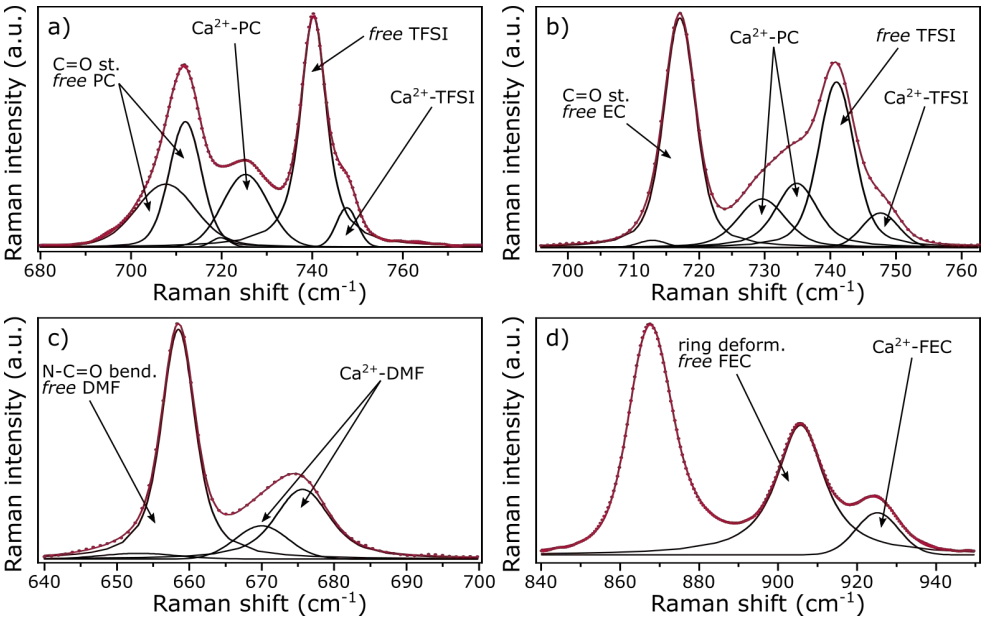

Figure 3.18: Deconvoluted Raman spectra of 0.7 M Ca(TFSI)$_2$ electrolytes. a) Ca(TFSI)$_2$ in PC, **b)** Ca(TFSI)$_2$ in EC, **c)** Ca(TFSI)$_2$ in DMF, and **d)** Ca(TFSI)$_2$ in FEC.

stretching for PC (sum of two bands at 706 and 712 cm^{-1}), and O=C−N bending for DMF (at 658 cm^{-1}). At this point, we also include fluoroethylene carbonate (FEC) as a model solvent with a very low donor number, and the band analysed is the ring breathing mode (at 905 cm^{-1}).

In all cases, the free solvent band shifts toward higher wavenumbers upon cation coordination. By deconvolution of the spectra (Figure 3.18), the solvation number (SN) of the cations was calculated using Equation 3.9:

$$\mathrm{SN} = \left(\frac{A_{bound}}{A_{bound} + \theta A_{free}}\right)\left(\frac{c_S}{c_{Ca^{2+}}}\right) \tag{3.9}$$

where c_S and $c_{Ca^{2+}}$ represent the molar concentrations of the solvent and Ca-salt, respectively. The parameter, θ, is the ratio of the Raman activity (RA) of free and coordinated solvent molecules as obtained by density functional theory (DFT) calculations ($\theta = \mathrm{RA}_{coord.}/\mathrm{RA}_{free}$). The fitting of the experimental Raman bands, and the estimation of the RA by computational methods carries some uncertainty that results in only a semi-quantitative estimation of the SN by this method.

Similarly, the number of TFSI anions coordinating each cation, as a measure

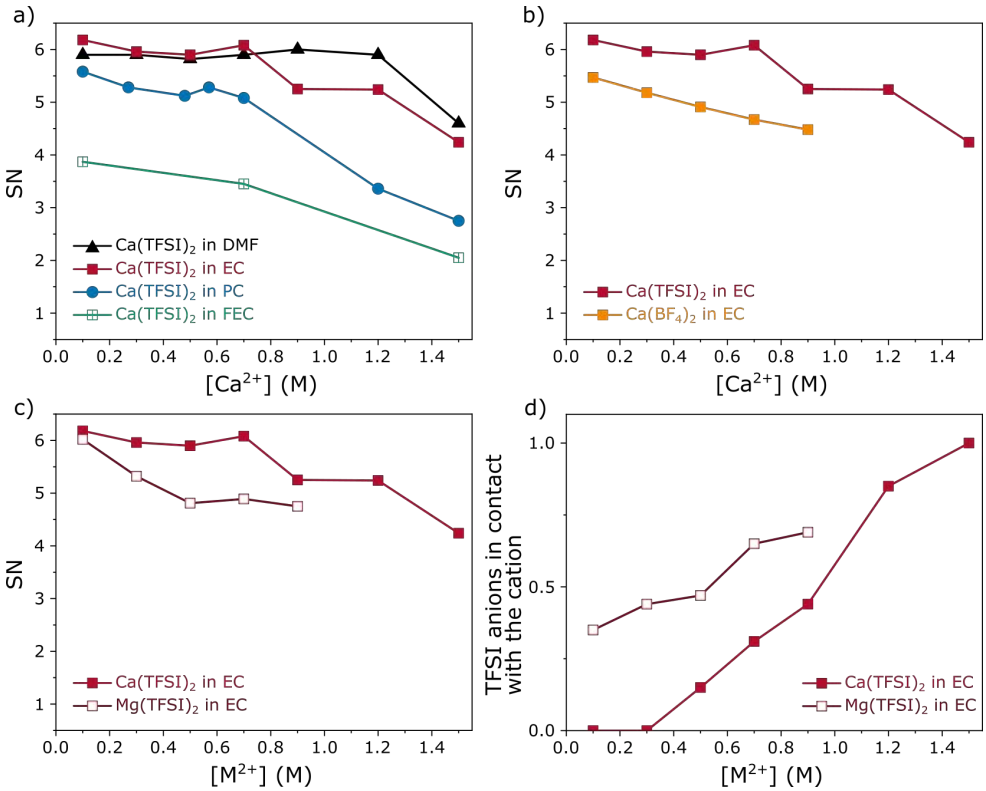

Figure 3.19: Evolution of the cation SN as function of salt concentration for different electrolytes. a) SN of Ca^{2+} in $Ca(TFSI)_2$ electrolytes in different solvents, **b)** comparison between $Ca(TFSI)_2$ and $Ca(BF_4)_2$ in EC electrolytes, **c)** comparison between $Ca(TFSI)_2$ and $Mg(TFSI)_2$ in EC, and **c)** estimation of the number of TFSI anions in contact with cations in $Ca(TFSI)_2$ and $Mg(TFSI)_2$ electrolytes in EC.

of the contact ion-pair concentration, was calculated using Equation 3.10.

$$\text{TFSI coordinated to } M^{2+} = \left(\frac{2A_{bound}}{A_{bound} + A_{free}} \right) \tag{3.10}$$

Which is derived from Equation 3.9 considering the 2:1 TFSI/Ca^{2+} relation and assuming that the RA of the TFSI breathing mode at 740 cm^{-1} does not change upon coordination (*i.e.* $\theta = 1$). This assumption has been previously suggested in the literature with successful results [127, 128].

The number of solvent molecules (SN) and TFSI anions in the first solvation shell of the cation is plotted in Figure 3.19 for the different solvents under study. A decrease in the SN is observed at high salt concentrations as a result

Table 3.5: Properties of the solvents employed.

Solvent	DN[a] (kcal mol^{-1})	ε^b
DMF	26.6	38.25
EC	16.4	89.78
PC	14.9	66.14
FEC	9.1	78.4

of TFSI anions being included in the first solvation shell:

$$[\mathrm{Ca(S)_x}]^{2+} + [\mathrm{TFSI}]^- \longrightarrow [\mathrm{Ca(S)_{x-1}}]^+ + \mathrm{S}$$

The concentration threshold at which this process is triggered is highly dependent on the solvent, DMF being the most resilient to be displaced, followed by EC, PC, and finally FEC. This trend follows the donor number of the different solvents ($\mathrm{DN}_{DMF} > \mathrm{DN}_{EC} > \mathrm{DN}_{PC} > \mathrm{DN}_{FEC}$) instead of their permittivity ($\varepsilon_{EC} > \varepsilon_{FEC} > \varepsilon_{PC} > \varepsilon_{DMF}$), as reported in Table 3.5. Surprisingly, the electrolytes using DMF appear to have the lowest concentration of ion-pairs, despite the lower ionicity found in the Walden analysis (Section 3.4) and supports the idea that solvent's DN is a crucial optimization parameter for divalent cation electrolytes.

This apparent contradiction can be rationalized in terms of the physical meaning of the solvent's relative permittivity and the donor number. The relative permittivity, ε_r, is measured as the proportion of the electric field (between two charged plates) that is screened by the presence of a material. A high ε_r solvent is, then, capable of limiting the attraction between two opposite charged ions in solution (Figure 3.20). The DN, although does not have a single unified definition, and several scales have been proposed over the years [129], it can be understood, as the interaction energy between a ligand (a solvent molecule in our case) and a Lewis acid (a cation in solution).

A high DN solvent, then, binds strongly to the metal cation and produces very stable $[\mathrm{Ca(S)_x}]^{2+}$ complexes, but if the solvent has a low dielectric constant, the strong binding will not impede the anion-cation interaction and the formation of $[\mathrm{Ca(S)_x(TFSI)}]^+$ adducts will be favoured. Therefore, the use of high DN solvents appears as a good strategy to prevent the formation of contact ion pairs (CIPs) but solvent separated ion pairs can be formed when such solvent possesses low dielectric constant.

When a more coordinating anion is used, a lower salt concentration is re-

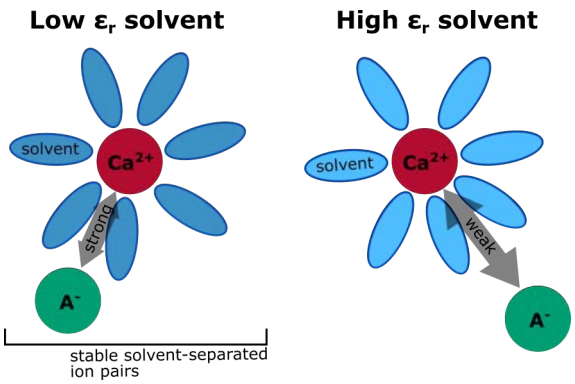

Figure 3.20: Illustration of the different strengths of interionic interaction in solvents of high and low relative permittivity.

quired to form stable cation-anion pairs. This is evidenced in the evolution of the solvation number calculated for $Ca(BF_4)_2$ in EC electrolytes at different concentrations (Figure 3.19b). This highlights the importance of development of new weakly coordinating anions for calcium and magnesium batteries. In fact, the panorama for magnesium electrolytes is even more drastic, with some evidence of Mg^{2+}-TFSI interaction at concentration as low as 0.1 M (Figure 3.19d). Also, a higher binding energy in Mg^{2+}-EC and Mg^{2+}-TFSI pairs has been reported (544 and 1442 kJ mol^{-1}, respectively) as compared to the Ca^{2+}-EC and Ca^{2+}-TFSI cases (380 and 1162 kJ mol^{-1}, respectively) [106].

3.6 Summary and Conclusions

Two complementary points of view have been presented in this chapter for the study of physicochemical properties of electrolytes. The study of the macroscopic properties such as density, viscosity, and ionic conductivity allowed the understanding of the global characteristics of the electrolyte while the spectroscopic study gave information about the local coordination of the cations in solution and the formation of contact ion pairs and aggregates.

In the macroscopic study, an effort was done to correlate the different properties under study to the physical underlying phenomena. This was accomplished by measuring the temperature-dependence of each property and fitting the obtained results to a suitable model. In the case of the density, for example, it was shown that an increase in the concentration causes a decrease in the thermal expansion coefficient, which is the result of a higher fraction of solvent participating in the solvation shell of the ions. The viscosity and

ionic conductivity, in turn, were fitted to a VTF model and trends in the pseudo-activation energy and Vogel temperature were observed. For example, it was shown that the Ca- and Mg-based electrolytes display a maximum in ionic conductivity at salt concentrations significantly lower than the Li-based electrolytes. This maximum, additionally, was found to be linked with a minimum in the pseudo-activation energy in the three cases.

The ionicity of the different electrolytes, as a measure to understand how independently the ions move in solution, was evaluated by means of the fractional Walden rule. Although interesting trends were observed in the slope and the intercept of the Walden plot, this model is mostly qualitative and is only capable of providing general trends when comparing different solvents or different salts of the same cation. It was not possible, however, to compare directly the ionicity of monovalent and divalent cation electrolytes given their fundamental differences in behaviour, as outlined in Section 3.4.

Compared to the macroscopic view, the vibration spectroscopy study allowed to study changes in the local structure of the cation solvation in a more quantitative way. On this respect, it was shown that the anion is more present in the solvation of the cation as the salt concentration increases. The threshold concentration where this process becomes dominant is a function of the solvent's donor number, and agrees with the minimum in the pseudo-activation energy for conductivity calculated by VTF fitting. A temperature-dependent Raman study would provide much more information to compare to the evolution of the macroscopic properties, particularly the ionic conductivity, which is expected to be highly influenced by ion-pair formation.

Effectively characterizing the second solvation shell of the cation is a much trickier task. However, using the combined local & macroscopic approach presented here, the effect of using a low relative permittivity solvent was discussed and compared to a high relative permittivity solvent.

4

Electrochemical Characterisation of Electrolytes & SEI Formation

After having explored the synthesis of new salts and the physicochemical properties of the resulting calcium electrolytes, here the compatibility of some calcium electrolytes with the operation of a battery based on a calcium metal anode is explored. The electrochemical tests mainly focus on the reductive stability of the electrolytes, as it will govern the performance of an electrolyte in contact with a metal with low standard redox potential, such as calcium (Standard redox potential Ca^{2+}/Ca = -2.87 *vs.* SHE). Electrolytes based on $Ca(BF_4)_2$ salt are more deeply investigated, as they have shown to allow electrochemical plating of Ca metal [62]. A detailed study on the morphology and chemical composition of the solid-electrolyte interphase (SEI) formed is presented, comparing with an $Ca(TFSI)_2$-based electrolyte, which does not allow for Ca electrodeposition.

Finally, based on the results obtained from the SEI analysis, some boron-based additives are proposed. Their electrochemical behaviour is studied, showing that they decompose upon reduction, forming a surface layer on the working electrode which is beneficial for the subsequent Ca plating/stripping reaction.

4.1 Electrochemical tests of $Ca(TFAB)_2$-based electrolytes

The electrochemical stability window (ESW) of a $Ca(TFAB)_2$ (calcium *tetrakis* (trifluoroacetyl)borate) in EC:PC electrolyte was measured on a stainless steel

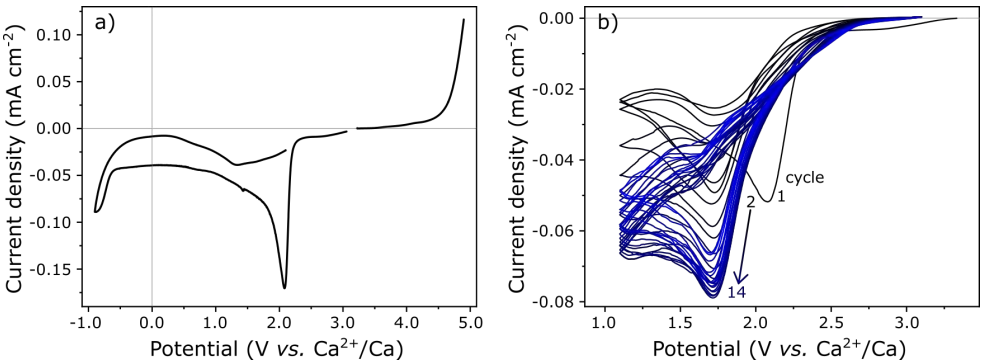

Figure 4.1: Electrochemical stability window determination of 0.1 M Ca(TFAB)$_2$ in EC:PC electrolytes. **a)** cathodic and anodic branches of the ESW measured at 1 mV/s. **b)** cycling of the electrolyte at 0.1 mV/s, focusing on the salt reduction peak. In both cases SS was used as WE, activated carbon cloth as CE, and Ag wire as RE (calibrated to Fc$^+$/Fc). Experiments performed at RT.

(SS) electrode by linear sweep voltammetry (LSV) at a scan rate of 1 mV/s (Figure 4.1a). As during the polarization towards positive or negative potential, the electrolyte can decompose forming a passivation layer which may interfere with the subsequent measurements, two independent cells were used to evaluate the cathodic and anodic stability branches. A clear oxidation wave starts at 4.5 V *vs.* Ca^{2+}/Ca although some minor oxidation current is evident already at 4 V. Upon reduction, a very intense peak is observed at 2.1 V *vs.* Ca^{2+}/Ca, attributed to anion decomposition. The electrolyte was cycled between 3.0 and 1.1 V *vs.* Ca^{2+}/Ca to focus on the decomposition of the anion and promote the formation of a passivation layer on the surface of the electrode (Figure 4.1b). However, this reduction peak does not decrease upon cycling, suggesting that the reductive decomposition of the TFAB anion does not produce an efficient passivation layer, it possibly generates only soluble species.

If the potential is further decreased, a second reduction process appears at -0.7 V *vs.* Ca^{2+}/Ca which could be related to calcium plating, although on the reverse scan no sign of calcium stripping is recorded. Therefore, the ESW of the 0.1 M Ca(TFAB)$_2$ in EC:PC electrolyte was found to be only 1.9 V (from 2.1 to 4.0 V *vs.* Ca^{2+}/Ca).

4.2 Electrochemical test of $Ca(BF_4)_2$-based electrolytes

4.2.1 Over stainless steel working electrodes

The voltammetric response of the 0.45 M $Ca(BF_4)_2$ in EC:PC shows the same behaviour as previously observed in the literature (Figure 4.2) [62]. During the first reduction, a reduction wave is recorded between 0.5-1.0 V *vs.* Ca^{2+}/Ca, attributed to solvent and/or anion decomposition and formation of a passivation layer on the electrode surface. Calcium plating occurs at potentials below -0.75 V *vs.* Ca^{2+}/Ca (peak potential $E_{p,red}$ = -0.99 V). The corresponding oxidation peak, attributed to Ca stripping ($Ca_{(s)} \longrightarrow Ca^{2+}$) is observed with an onset potential at -0.45 V ($E_{p,ox}$ = -0.32 V). Calcium plating and stripping are observed here at potentials below 0 V *vs.* Ca metal due to the formation of a passivation layer on the RE, which causes a shift on its redox potential, as reported previously [130].

A constant electrolyte decomposition is observed during the entire experiment, resulting in a residual reduction current and shifting the entire CV curve to negative current values. This residual current diminishes upon cycling as the electrode surface gets more passivated, however it is still evident after 9 cycles.

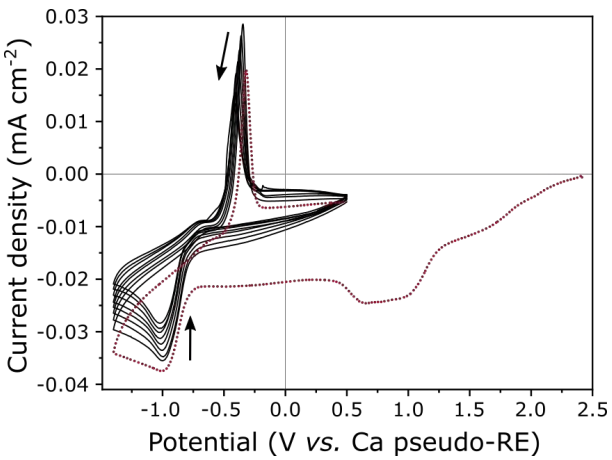

Figure 4.2: Cyclic voltammogram of 0.45 M $Ca(BF_4)_2$ in EC:PC electrolyte over a SS electrode (0.1 mV/s and 100 °C). 1_{st} cycle: dashed red curve; 2_{nd}-9_{th} cycles: continuous black curve. RE: Ca metal, and CE: Ca metal. Arrows show the evolution of peak intensity during cycling.

The efficiency for calcium plating was found to be dependent on the salt quality. The salt prepared by direct reaction of CaF_2 and $BF_{3(g)}$ in aHF solvent (refer to Chapter 2, page 25 for details) presented the highest stripping capacity, which is used here as a measure of the amount of metallic calcium deposited. While the deposited calcium in this case is about 44 mC cm^{-2}, the salts prepared by other methods are at least 50% lower (around 30 mC cm^{-2}). The water content in the $Ca(BF_4)_2$ electrolytes produced by the two anhydrous synthetic routes were below 110 ppm while the one produced by drying of the commercial product was about 135 ppm, according to KF titration. Aside from water, it is suggested that the presence of some other non-identified contaminants, as showed in Chapter 2.1 - page 27 are responsible for the difference observed in the CV curves.

4.2.2 Over Ca electrodes

Figure 4.3 shows the voltammetry response of a calcium electrode upon reduction, where the peak for Ca electrodeposition is observed at around -1 V *vs.* a Ca metal used as RE. As mentioned in the case of calcium plating on SS electrodes, the Ca metal RE in this configuration does not operate at the expected potential of the Ca^{2+}/Ca couple due to the formation of a passivation layer at the surface. This results in an unreliable measured potential when Ca metal is used as RE (same would happen with a Mg RE), as discussed in previous studies [130], where a shift of up to 1 V is observed in the Ca RE in this electrolyte. Additionally, as Ca metal is also employed here as WE,

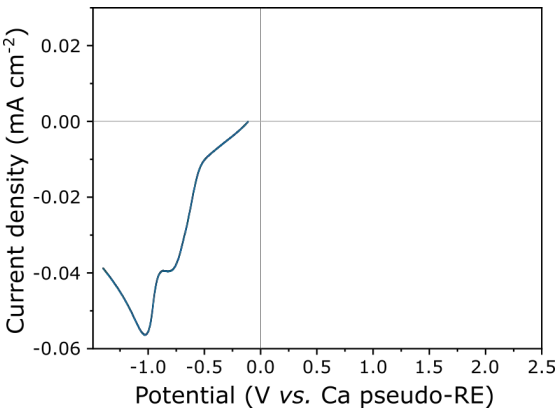

Figure 4.3: Linear sweep voltammetry of 0.45 M $Ca(BF_4)_2$ solutions in EC:PC over a metallic calcium electrode. Temperature: 100 °C, sweep rate: 0.1 mV/s, CE: Ca metal; RE: Ca metal.

it is expected to get passivated upon contact with the electrolyte, further hampering the plating of Ca. Previous studies have shown how strongly the electrochemical response of a Ca electrode is related to its passivation layer [131].

Given the problems arising from the use of Ca metal as RE for electrochemical tests, across the time-spam of this thesis several other RE were tested (Ag wire, or Ag_2S/Ag) and their potential was calibrated using ferrocene (Fc) as standard. This was the case for the experiments presented below. More details about this calibration are shown in Chapter 6 - Experimental methods, page 122.

Holding the Ca working electrode at -4.2 V *vs.* Ag wire RE (-1 V *vs.* Ca^{2+}/Ca) for several hours resulted in the formation of a thick deposit on the surface, evidenced by the dark black colour of the originally shiny calcium electrode (Figure 4.4a). The low conductivity of Ca^{2+} cations across the surface layer resulted in very low current densities < 10 μA cm^{-2} after 20 h. The growth of the passivation layer was followed by dynamic Electrochemical Impedance Spectroscopy (EIS) every 2 h. A constant bias of -1 V *vs.* Ca^{2+}/Ca was maintained while a potential wave with 20 mV of amplitude was applied, the obtained impedance spectra are shown in Figure 4.4b. The total impedance of the electrode, represented by the diameter of the semicircle, increases significantly in the first 10-20 h of polarization and it is not entirely stabilized even after 100 h. This suggests that the passivation of the electrode is incomplete, and that the SEI grows continuously during the process.

In dynamic EIS, a constant current or potential is set at the WE on top of which the sinusoidal perturbation is applied. Although its less employed than the static EIS (performed at OCV), it has been used in the elucidation of Mg or Li metal plating mechanisms [47, 132]. It is particularly suitable for the investigation of processes which require the application of a higher potential than the applied in EIS perturbation ($\sim$20 mV).

Naturally, the dynamic EIS involves a continuous change in properties of the electrode under testing and is, therefore, in a non-stationary regime. This contradicts in principle the conditions of stationarity and linearity required for correct interpretation of EIS data, but could be circumvent if a correct experimental protocol is implemented. For example, the non-stationary distortions could be reduced by measuring at steady-state, when a constant current is obtained (*e.g.* t $>$ 80 h in Figure 4.4a). Indeed this condition was verified with the help of Dr. Romain Dugas from Collège de France (Paris) by fitting the

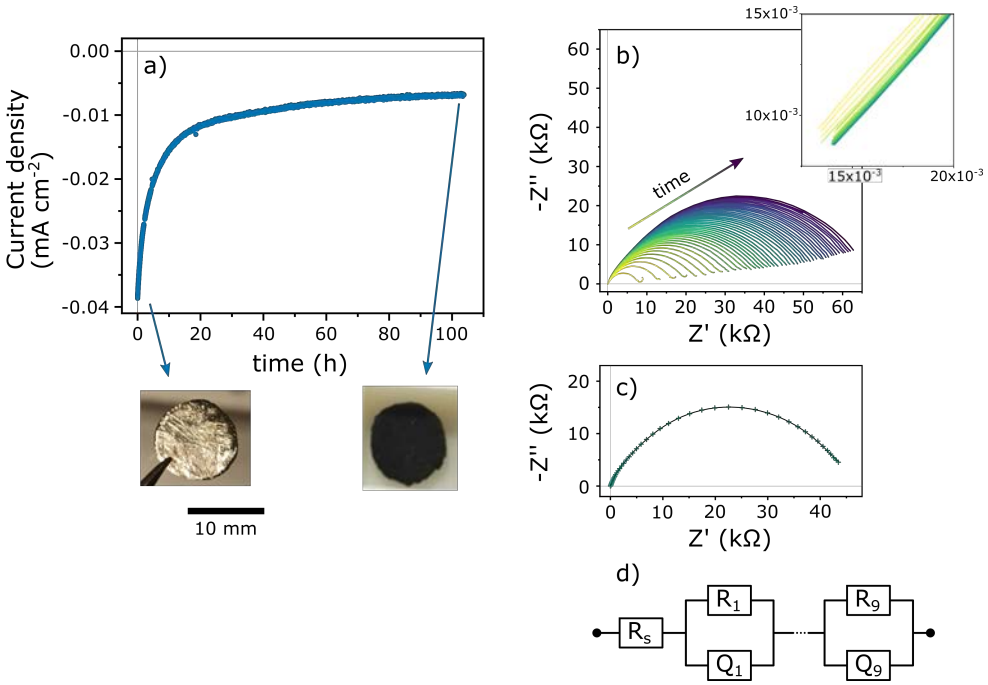

Figure 4.4: Electrochemical response of a Ca metal electrode upon polarization at −1 V *vs.* Ca^{2+}/Ca. a) current density as function time with pictures of the metal electrodes at the beginning and at the end of the polarization period. **b)** Nyquist plots of the EIS response of the electrode hold at -1 V *vs.* Ca^{2+}/Ca and measured every 2h. Inset: zoom in the high frequency region. **c)** Nyquist plot showing the impedance of the WE after 40h (markers) together fitted response, corroborating the Kramers-Kronig conditions. **d)** Equivalent circuit used to fit the data in panel **c)**. Temperature: 100 °C, WE: Ca metal; CE: Ca metal; RE: Ag ring.

EIS spectra to a model circuit consisting of a series of R|Q elements, as shown in Figure 4.4c. The equivalent circuit displayed in Figure 4.4d was used to fit the experimental data, where R_i is a resistance and Q_i is a constant phase element which complex impedance is given by: $Z(\omega) = ((i\omega)^{\alpha} C_{\alpha})^{-1}$ with $0 < \alpha \leq 1$. The equivalent circuit employed here lacks any physical meaning, and thus the parameters obtained for R_i and C_{α} give little information regarding the real process happening at the electrode. This fitting procedure was only employed to corroborate the compliance of the obtained parameters to the stationarity and linearity conditions. As the experimental data deviate only marginally from the fitted spectrum, it is deduced that the EIS response fulfills the Kramers-Kronig conditions of linearity and stationarity.

The intercept of the impedance spectra with the Z′ axis at high frequencies

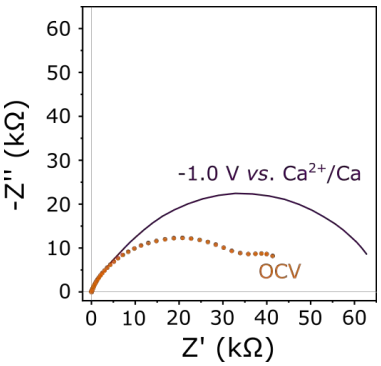

Figure 4.5: Impedance spectra of a Ca metal electrode recorded at the end of 100 h of polarization. Impedance recorded at under bias (-1 V *vs.* Ca^{2+}/Ca, continuous line) and after relaxation at OCV (markers). Temperature: 100 °C, WE: Ca metal; CE: Ca metal; RE: Ag ring.

corresponds to the resistivity (inverse of the conductivity) of the electrolyte between the RE and WE. During the potentiostatic experiment, a constant shift to higher Z′ values evidences the decrease in the ionic conductivity of the solution, caused by the consumption of the salt (inset Figure 4.4b). This agrees with a continuous SEI formation by electrolyte decomposition.

Subsequently, the potential of the electrode was left to relax to OCV, reaching a stable potential of -0.1 V *vs.* Ca^{2+}/Ca after 10 minutes, and the impedance was remeasured (Figure 4.5). The difference between the two measurements (at -1 V and at OCV) can be tentatively rationalized understanding the different phenomena occurring at the two different potentials. At -1 V, the response of impedance signal is the sum of: *i)* the calcium migration in the liquid, *ii)* the desolvation of the calcium cation at the surface, *iii)* the migration of Ca^{2+} cations through the SEI, and *iv)* the plating of Ca^{2+} onto the metal surface. In contrast, at OCV the amplitude of the impedance perturbation (20 mV) is not enough to allow all these processes to happen, and thus only some of them will be active, reducing the total impedance of the electrode. A similar effect is observed with graphite or $Li_4Ti_5O_{12}$ electrodes in lithium electrolytes, which behave as blocking electrodes at OCV but showed a significant change in the impedance upon negative polarization, as lithium intercalation in both materials starts to take place [133, 134].

The deconvolution of the different phenomena occurring during the EIS measurement could be obtained by fitting of the impedance spectra to a suitable equivalent circuit or a transmission line model as described by other authors [135]. However, particular care needs to be taken to guarantee the compliance of the measured data to linearity, as described before, this project is left open for future studies.

A symmetrical Ca||Ca cell was assembled and cycled at constant current.

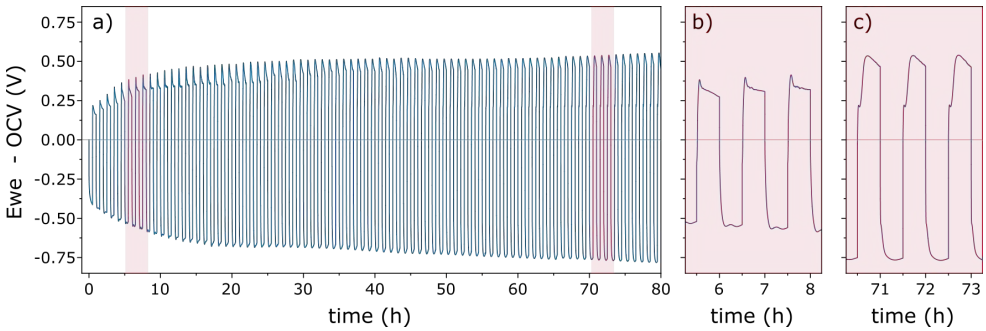

Figure 4.6: Galvanostatic cycling of a Ca working electrode in a 0.45 M $Ca(BF_4)_2$ in EC:PC electrolyte Electrolyte prepared by heating treatment of the commercial salt, as descried in Chapter 2.1 - page 17. Alternating current steps of 30 μA cm^{-2} and -30 μA cm^{-2} for 30 minutes each. Experiments performed at 100 °C using Ca CE and Ag wire RE. Zoom of the highlighted areas in panel **a)** are presented in panels **b)** and **c)**.

Figure 4.6 shows the evolution of the potential of one of the Ca metal electrodes (measured in a 3-electrode cell configuration) when subsequent cycles of 30 min of plating/stripping are applied at a current density of 30 μA cm^{-2}. In the first cycles, a sharp peak was recorded at the beginning of the stripping step. Similar behaviour was previously reported for the first oxidation of a calcium electrode in a DME-based electrolyte [136], and ascribed to the breakdown of the SEI layer. After several cycles, this oxidation peak becomes less evident, and while the total polarization between plating and stripping grows in the first 20 h, the whole process almost stabilized. A possible explanation for this evolution is a continuous change of the structure and ionic conductivity of the SEI layer upon cycling, especially important during the first cycles.

Later in this chapter, a detailed study of the passivation layer (or SEI) formed on Ca electrodes is presented. Briefly, it was observed that the SEI formed using a $Ca(BF_4)_2$-based electrolyte is rich in borate species which might be responsible for the ionic conductivity of the layer. Therefore, a first attempt to enhance the borate content of the SEI was carried out by changing the salt concentration in the electrolyte. Figure 4.7 shows the recorded impedance spectra of calcium electrodes at OCV after being polarized at -1 V *vs.* Ca^{2+}/Ca for 100 h in 0.1-0.9 M $Ca(BF_4)_2$ in EC:PC electrolytes. A clear trend is observed with the impedance decreasing as the salt concentration was increased, the lowest value being recorded in the case of the 0.9 M solution. While the origin of such differences remains unclear it can be indicative of the formation of a SEI layer more favourable for cation transport at high salt

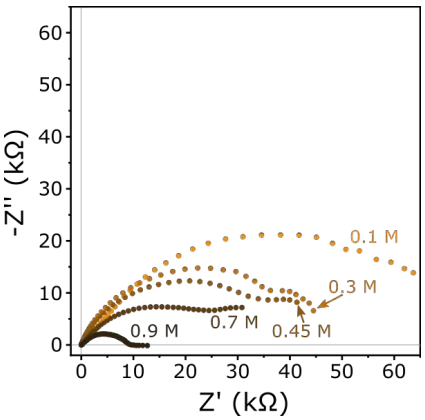

Figure 4.7: Nyquist plots of calcium metal electrodes at OCV after being polarized at -1 V *vs.* Ca^{2+}/Ca for 100 h in 0.1-0.9 M $Ca(BF_4)_2$ in EC:PC electrolytes. Temperature: 100 °C, WE: Ca metal; CE: Ca metal; RE: Ag ring.

concentration, even though the liquid electrolyte at such high salt concentration presents lower ionic conductivity and high viscosity (see Chapter 3, page 49). These are promising results towards the optimization of the Ca plating and stripping kinetics, and a systematic characterization of passivation layers formed at different salt concentrations is underway in order to determine the relationship between low impedance and SEI chemical composition and morphology.

4.3 SEI formation: TFSI *vs.* BF_4^- based electrolytes

Contrary to the case of $Ca(BF_4)_2$ electrolytes, which allow calcium plating and stripping at elevated temperatures, the use of electrolytes based on $Ca(TFSI)_2$ results in completely featureless CV curves (Figure 4.8). In both cases, it is expected that a surface layer covering the electrode is formed, which properties are likely to affect the migration of cations and thus the electrochemical response. In this section a comparative study of the morphology and chemical composition of the passivation films formed in both electrolytes is presented.

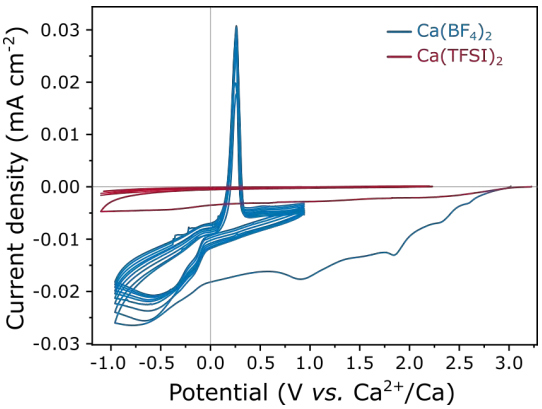

Figure 4.8: Cyclic voltammograms over a SS electrode of 0.45 M $Ca(BF_4)_2$ and $Ca(TFSI)_2$ in EC:PC electrolytes. Cycles 1-9 are shown. Scan rate: 0.1 mV/s, temperature: 100 °C, WE: SS; CE: Ca metal; RE: Ag wire, calibrated with Fc^+/Fc.

4.3.1 Morphology

The morphology of the passivation layers formed electrochemically from the two electrolytes was studied by transmission electron microscopy (TEM) with the help of Dr. Carine Davoisne from the Laboratoire de Réactivité et Chimie des Solides in Amiens (France). For the deposition of the films, nickel powder particles were used as a working electrode without the addition of any binder and were held in contact with the current collector by the glass fibre separator and the spring in the Swagelok cell (see Chapter 6 - page 121 for details). Figure 4.9 shows the obtained nickel particles before and after a potentiostatic deposition at -1.4 V *vs.* Ca metal for 48 hours.

In the case of $Ca(TFSI)_2$ based electrolyte, a 12-20 nm thick amorphous layer covers homogeneously the nickel surface (Figure 4.9b). In contrast, in the $Ca(BF_4)_2$ electrolyte, the deposit is thicker ∼70-80 nm (named SEI2) and presents a polycrystalline morphology, as observed by the presence of well-defined rings in the selected area electron diffraction in the inset of Figure 4.9d. The layer is composed of small crystallites of ∼10 nm in size and the indexing of the diffraction pattern is in good agreement with that of CaF_2. In some areas, additional amorphous sheet-like features (named SEI1) are observed.

Despite producing a much thinner surface layer, the $Ca(TFSI)_2$ based electrolyte does not allow for reversible plating/stripping of Ca metal, which suggest that this layer has remarkably low ionic conductivity, and thus a mere

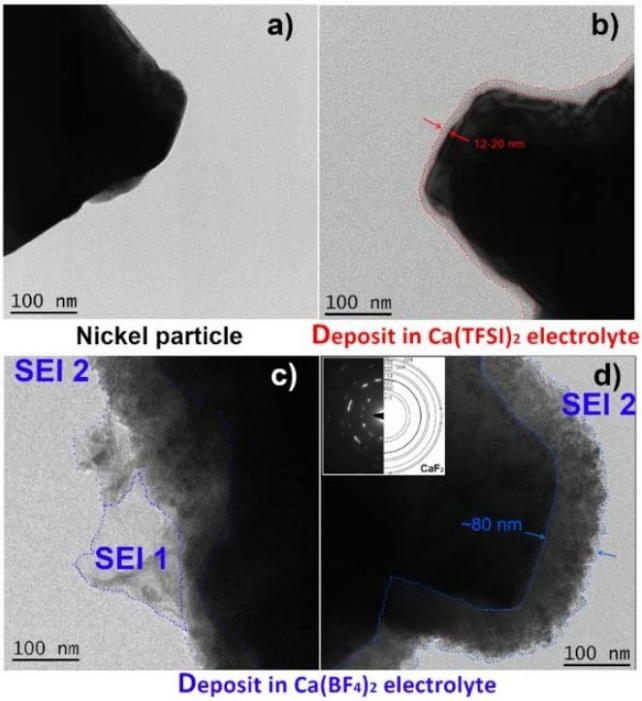

Figure 4.9: Bright field TEM images of Ni particles before and after formation of a surface layer. **a)** pristine Ni particles, **b)** nickel particles after 48h deposition in $Ca(TFSI)_2$-based electrolyte. **c)** and **d)** nickel particles after deposition in $Ca(BF_4)_2$-based electrolyte. Red and blue dotted lines are as a guide for the eye to indicate the thickness of each passivation layer. The inset in panel **d)** corresponds to the diffraction pattern associated to the deposit.

20 nm are sufficient to passivate fully the electrode. In contrast, the surface layer produced using the $Ca(BF_4)_2$ based electrolyte seems much less compact, resembling an organic polymeric deposit in which the CaF_2 crystallites are embedded.

4.3.2 Chemical Composition

In an attempt to link the ionic conductivity of the deposited surface layers to a difference in composition, the surface layers produced using $Ca(BF_4)_2$ and $Ca(TFSI)_2$ based electrolytes were analysed by XPS, FTIR and Electron energy loss spectroscopy (EELS). The XPS and EELS experiments were carried out in collaboration with, respectively, Dr. Rémi Dedryvère from the Institut des Sciences Analytiques et de Physico-Chimie pour l'Environnement et les Matériaux (IPREM) in Pau and Dr. Carine Davoisne from the Lab-

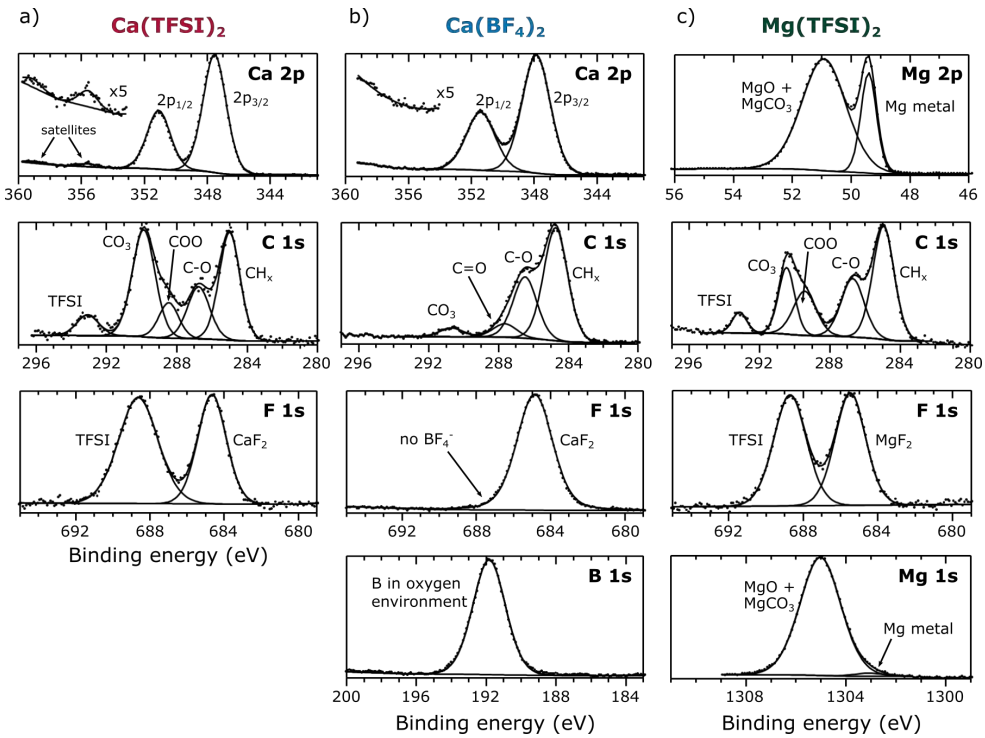

Figure 4.10: XPS spectra of the passivation layers over Ca and Mg electrodes in different electrolytes. a) 0.45 M $Ca(TFSI)_2$ in EC:PC, **b)** 0.45 M $Ca(BF_4)_2$ in EC:PC, and **c)** 0.45 M $Mg(TFSI)_2$ in EC:PC. The surface layers were prepared by polarizing metallic electrodes for 48h at -1.4 V *vs.* Ca or Mg metal RE, accordingly. The binding energy scale was calibrated by the C 1s peak from hydrocarbon contamination at 285.0 eV.

oratoire de Réactivité et Chimie des Solides (LRCS) in Amiens. The IR-microspectroscopy experiments were performed at the MIRAS beamline at ALBA synchrotron radiation source, with the assistance of Dr. Ibraheem Yousef.

The C 1s, Ca 2p, F 1s and B 1s XPS spectra of calcium disks polarized at -1.4 V *vs.* Ca metal at 100 °C for 48 h in either $Ca(TFSI)_2$ or $Ca(BF_4)_2$ based electrolytes is shown in Figure 4.10, with the corresponding quantitative elemental distribution summarized in Annex E. For the two disks, the signal of the metallic calcium was not detectable, meaning that in each case the calcium surface is covered by a thicker layer than the maximum depth that the XPS can probe (∼10 nm). The surface layer produced by the $Ca(TFSI)_2$ based electrolyte could be recorded without any charge compensation, whereas the one from $Ca(BF_4)_2$ based electrolyte could not. These observations indi-

cate an important difference in chemical composition, affecting the electronic conductivity of the film, as much as a difference in their thickness [137], in agreement with TEM observations.

The $Ca(TFSI)_2$ disk was characterised by a substantial quantity of carbonate, accompanied by mono- and di-oxygenated carbon atom environments from undefined species. In the Ca 2p spectrum, additionally, two satellite (plasmon) features are observed at +8 eV from $2p_{3/2}$ and $2p_{1/2}$ main peaks (355.5 and 359 eV) correspond with previous reports of $CaCO_3$ and CaO [138, 139].

In the B 1s spectrum of the film produced by the $Ca(BF_4)_2$ based electrolyte, a great amount of boron (∼14%) was observed. The electron binding energy found for the B 1s peak (Figure 4.10b) correspond to a boron in an oxygenated environment, in contrast to the original B−F coordination which would produce a peak centered above 195 eV [140]. The absence of B−F groups reveals a complete displacement of the fluoride ligands by oxygen atoms, in agreement with previous reports on the labile character of the tetrafluoroborate anion [141]. Additionally, the C 1s spectrum shows that the surface contains much lower proportion of carbonate (∼8% $CaCO_3$) when compared with the $Ca(TFSI)_2$-derived layer, although the total contribution of other carbon species (C−C, C−H and C=O) corresponds to ∼35 at.% of the surface for BF_4^-, instead of ∼16 at.% for TFSI. The higher content of carbon (aside from CO_3^{2-}), boron and oxygen in the BF_4^--derived SEI suggests that this surface layer is much richer in organic species than the TFSI-derived one, possibly comprising the formation of polymeric species containing boron.

Finally, a higher content of fluoride is detected in the surface layer produced by $Ca(BF_4)_2$ based electrolyte, agreeing with the large amount of crystalline CaF_2 observed by TEM and with the very low electronic conductivity of the sample's surface which required charge compensation when performing the XPS measurements.

The passivation layer formed in a Mg surface in a $Mg(TFSI)_2$ electrolyte resembles the one produced in the equivalent calcium case (Figure 4.10c), although it is much thinner, allowing the detection of Mg metal in the XPS measurement. A high content of $MgCO_3$ is formed, as a result of carbonate solvent decomposition, as was the case for the $Ca(TFSI)_2$ electrolyte. A carbonate-rich layer appears to block entirely the electrochemistry of both Ca and Mg metal electrodes, in agreement with the high migration energy barriers calculated for the cations in this materials (1436 and 1814 meV in

$CaCO_3$ and $MgCO_3$, respectively) [142].

In order to gain more information about the chemical species present in both surface layers, IR spectra were measured and compared with some relevant reference compounds (Figure 4.11). The spectrum of the film formed in the TFSI based electrolyte showed no distinguishable bands, because the SEI was too thin and the total mass of deposited species was too low to be clearly detected. In contrast, in the FTIR spectrum of the film deposited from the BF_4^- based electrolyte, several bands can be assigned to a number of functional groups, including ∼3500 cm^{-1} the O−H stretching, ∼2900 cm^{-1} the C−H stretching, 1850-1700 cm^{-1} the C=O stretching, ∼1073 cm^{-1} the C(=O)−O stretching, and ∼780 cm^{-1} the CH_2 rocking. These vibration modes were assigned by comparing the obtained IR spectra to the reported assignment for EC or PC pure solvents [143, 144], and thus it is concluded that some solvent molecules remain trapped in the SEI layer, or that the decomposition products generated by electrolyte decomposition maintain these functional groups. For example, the strong absorption bands observed between 1750-1800 cm^{-1} may arise from ring-opening decomposition of EC or PC, in which the solid product deposited on the surface keeps the C=O or C(=O)−O moieties [11].

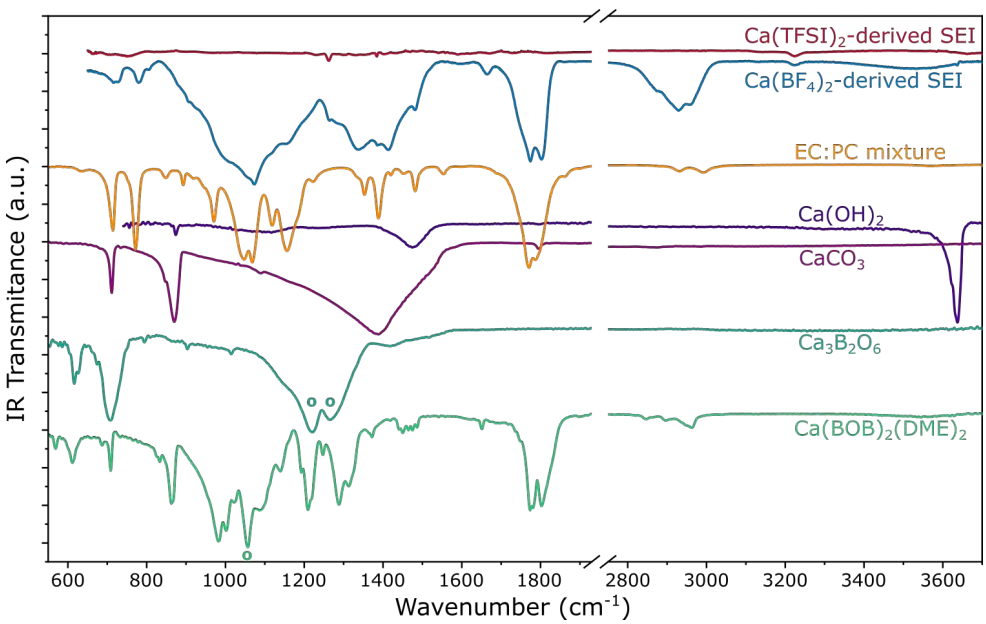

Figure 4.11: IR spectra of the surface layer deposited in $Ca(TFSI)_2$ and $Ca(BF_4)_2$ based electrolytes, compared to some reference compounds. The bands marked with ° indicate vibrations of the $[BO_3]$ or $[BO_4]$ moieties.

Table 4.1: Fundamental vibration modes of $[BO_3]$ and $[BO_4]$ groups.

Mode	$[BO_3]$		$[BO_4]$	
ν_1 symmetric str.	~950 cm^{-1}	IR inactive	< 950 cm^{-1}	IR inactive
ν_2 out-of-plane bend.	~750 cm^{-1}	IR active	< 600 cm^{-1}	IR inactive - doubly degenerated
ν_3 asymmetric str.	~1250 cm^{-1}	IR active - doubly degenerated	~1000 cm^{-1}	IR active - triply degenerated
ν_4 in-plane bend.	~600 cm^{-1}	IR active - doubly degenerated	~600 cm^{-1}	IR active - triply degenerated

As it was previously established that the SEI produced in the $Ca(BF_4)_2$ based electrolyte contains significant amounts of boron in oxygenated environment, the spectra of two model compounds were used as reference: $Ca(BOB)_2(DME)_2$, and $Ca_3B_2O_6$, containing tetragonal or trigonal boron moieties, respectively (Figure 4.11). Previous spectroscopic analysis of $[BO_3]$ trigonal and $[BO_4]$ tetrahedral groups established that both structures present four fundamental vibration modes (Table 4.1) [145]. The ν_3, being IR active and intense, will serve as a probe for the coordination environment for boron. It is located at ~1000 cm^{-1} for $[BO_4]$ groups (band at 1089 cm^{-1} for $Ca(DME)_2(BOB)_2$) and ~1250 cm^{-1} for isolated $[BO_3]$ groups (band at 1219 and 1269 cm^{-1} in $Ca_3B_2O_6$). In the IR spectrum of the SEI layer produced in $Ca(BF_4)_2$, the band located at ~1336 cm^{-1} is assigned to B−O stretching, in what is hypothesised as $[BO_3]$ coordination. This hypothesis will be corroborated later by complementary techniques as EELS. The higher wavenumber of this mode, when compared to the model calcium borate $Ca_3B_2O_6$, suggest that the $[BO_3]$ moieties are not isolated, like in the case of $Ca_3B_2O_6$, but rather are part of a bigger molecule producing stronger B−O links.

While FTIR spectra obtained by diffuse reflectance provide an average contribution of different compounds present in a relatively large area of analysis (typically few mm^2), synchrotron FTIR-microspectroscopy can resolve the different contributions from different regions of the deposit with a spatial resolution of 50 μm × 50 μm. Figure 4.12a shows the IR spectra measured at two different points, A and B, across the surface of the $Ca(BF_4)_2$-derived SEI. Clearly different compounds are present in different proportions in these two

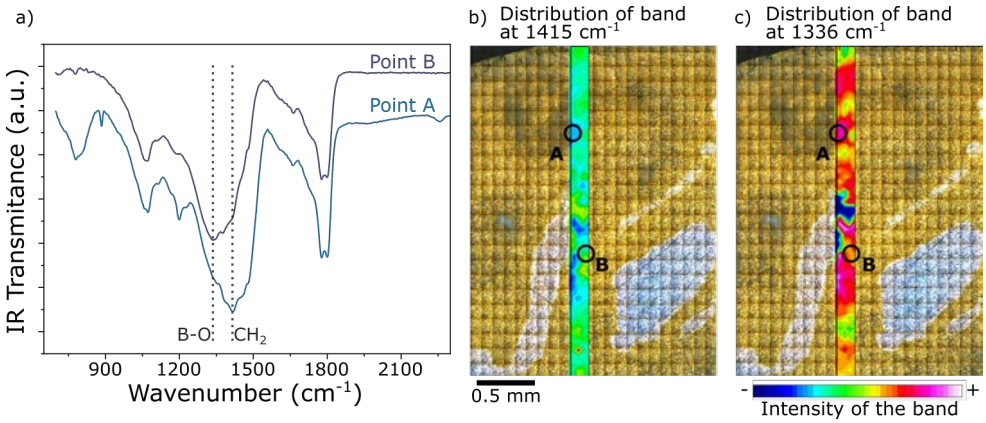

Figure 4.12: FTIR-microspectroscopy analysis of the $Ca(BF_4)_2$-derived SEI. a) IR spectra of regions A and B marked in panel **b)** and **c)**. **b) and c)** Optical image of the working electrode covered with the surface layer (top view), showing the distribution of the two analysed bands across the surface.

points, and their distribution is not homogenous across the surface, as shown in Figure 4.12b and 4.12c. In the IR spectrum measured at point A, the band centered at 1415 cm^{-1} has been attributed to a CH_2 bending vibration, with other vibrations typical from this group observed at 1191 and 775 cm^{-1}. On the other hand, the IR spectrum recorded at point B shows a band centered at 1336 cm^{-1} which was attributed, as mentioned before, to the B−O vibration in $[BO_3]$ groups. The spatial distribution of the two components, displayed in Figure 4.12b and 4.12c, shows a high inhomogeneity in the μm range, which is expected to impact the cycling behaviour when such a passivation layer covers the surface of the electrode.

The deposits were also studied by EELS and the normalized spectra of B K-edge, Ca $L_{2,3}$ edge, O K-edge are presented in Figure 4.13, together with the spectra of some reference compounds. In the case of the $Ca(TFSI)_2$-derived deposit, the presence of calcium and oxygen is clearly visible in the spectrum. The position and shape of the Ca $L_{2,3}$ edge is similar to the other calcium compounds (*e.g.* CaB_2O_4, CaF_2), but the exact chemical environment of Ca cannot be determined due to the low sensitivity of the Ca edge to the Ca coordination (as demonstrated in Figure 4.13b).

In the case of the $Ca(BF_4)_2$ based electrolyte, the EELS measurements were performed in the two different areas observed by TEM (SEI1 and SEI2 in Figure 4.9). Figure 4.13a shows the EELS spectra on the B K-edge for the *SEI1* structure, together with the spectra of BPO_4 and $Ca(BF_4)_2$ as refer-

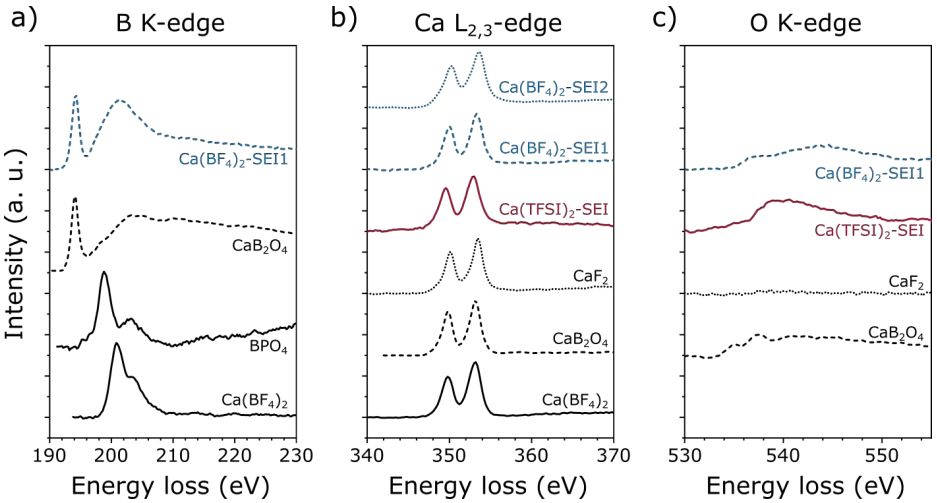

Figure 4.13: Normalized EELS spectra of the deposited films in 0.45 M $Ca(BF_4)_2$ and 0.45 M $Ca(TFSI)_2$ electrolytes in EC:PC, compared to reference compounds. a) B K-edge, **b)** Ca $L_{2,3}$-edge, and **c)** O K-edge regions.

ences for tetra-coordinated boron and CaB_2O_4 as reference for tri-coordinated boron. In the case of $Ca(BF_4)_2$, in the B K-edge the main peak σ^* appears at 200.8 eV, in agreement with previous studies on metal-BF_4 compounds [146]. Similar peak positions were observed for BPO_4 with the most prominent contribution σ^* at 198.9 eV and a second peak at 203.2 eV. In contrast with CaB_2O_4, in which the main component π^* and a broader σ^* appeared at 194.2 and 203 eV, respectively. The peaks position and shape of these two references are in agreement with previous EELS studies on minerals with boron in trigonal and tetrahedral coordination, respectively [147, 148]. The B K-edge obtained on SEI1 is composed of a primary π^* peak at 194.3 eV and followed by a broader σ^* peak at 201.3 eV. These signatures correspond in position and shape to the signal of a boron in a BO_3 coordination environment confirming the FTIR analyses.

4.3.3 Mechanisms of SEI formation

It was observed that the surface layer produced using the $Ca(TFSI)_2$ based electrolyte is composed mainly by calcium carbonate and other carbonaceous species, produced by solvent decomposition. Remarkably, little anion decomposition is observed, even when previous reports on the electrochemical stability of TFSI suggest that it would decompose at potentials above the calcium redox potential [149]. In contrast, the surface layer in the $Ca(BF_4)_2$

based electrolyte was found to be composed by CaF_2 and borates, produced by anion decomposition.

The difference between solvent-derived and anion-derived surface layers is hypothesised to be the result of differences in the cation solvation shell in the electrolyte. Indeed, as studied in Chapter 3 (Physicochemical Properties, page 64), the Ca^{2+} solvation shell in a 0.45 M $Ca(TFSI)_2$ in EC:PC electrolyte will be composed entirely by solvent molecules, while the same composition using $Ca(BF_4)_2$ salt results in some degree of BF_4^- anions in contact with the cation. Upon negative polarization of the WE, cations will migrate to the surface carrying their solvation shell with them and depleting the surface of negatively charged species (*e.g.* free anions). When the potential of the electrode reaches a sufficiently negative value, the nearby solvents will decompose reductively, and the products will precipitate in the surface. In the case of carbonate solvents, this decomposition results in calcium carbonate and alkoxides which cover entirely the surface and block further electrochemical reactions [150].

In the case of the $Ca(BF_4)_2$ based electrolyte, it was observed that a significant fraction of ion-pairs persists in solution. As the ion pairs are still positively charged ($[Ca{-}BF_4]^+$) they will still tend to accumulate in the surface of the WE upon polarization, leading to a substantial concentration of anions at the interface. The BF_4^- anion is not expected to be directly susceptible to reduction, but it can suffer from a nucleophilic attack of a nearby generated alkoxide groups, as shown in Figure 4.14. The nucleophilic substitution is further facilitated by the formation of solid CaF_2 which precipitate at the surface of the electrode favouring complete anion decomposition.

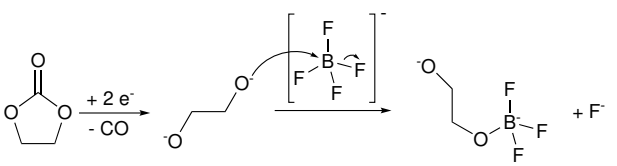

Figure 4.14: Possible decomposition pathway of a BF_4^- electrolyte upon reduction in the surface of a Ca metal electrode.

4.3.4 Decoupling SEI composition and electrolyte formulation

The passivation layers formed in TFSI or BF_4^--based electrolytes were found to differ significantly in composition, the former contains mostly carbonates, whereas the latter contains mostly borates, CaF_2 and organic (polymeric)

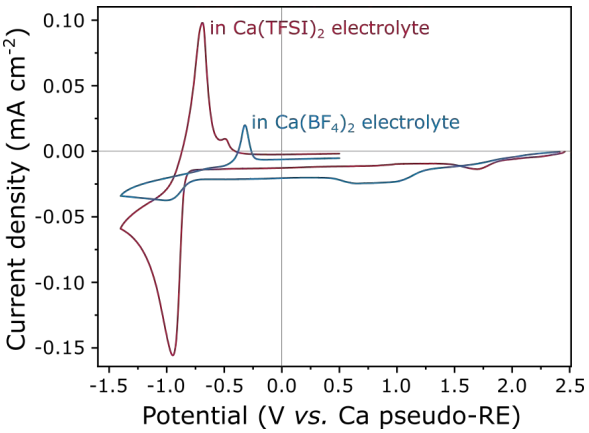

Figure 4.15: Cyclic voltammograms of pre-passivated stainless-steel electrodes previously covered with a borate containing passivation layer. Cycling at 0.1 mV s^{-1} using 0.45 M in EC:PC electrolytes based on either $Ca(TFSI)_2$ (red curve) or $Ca(BF_4)_2$ (blue curve) at 100 °C. CE: Ca metal, RE: Ca metal.

species. As aforementioned, TFSI-based electrolyte does not allow for Ca plating and stripping which can only be achieved when $Ca(BF_4)_2$ salt is used (Figure 4.8).

In order to ascertain the role of the passivation layer, a pre-passivation protocol was established, in which a stainless-steel electrode was cycled at 0.1 mV s^{-1} between 0.1 and -1.4 V *vs.* Ca metal for 10 cycles, in a 0.45 M $Ca(BF_4)_2$ in EC:PC electrolyte. The cycling was performed at 100 °C using three-electrode cells with calcium disks as reference and counter electrodes. After the 10 cycles, the cells were disassembled, the electrodes were washed thoroughly using dimethyl carbonate and dried under vacuum before the cell were reassembled using the same three electrodes. This passivation protocol covered the stainless steel working electrode by a borate containing passivation layer as described in the previous section. Figure 4.15 shows the electrochemical plating/stripping curves using such pre-passivated substrates, which were transferred to new cells and cycled in a 0.45 M $Ca(TFSI)_2$ in EC:PC electrolyte. After pre-passivation, not only Ca plating and stripping can be observed in TFSI-based electrolyte but a remarkable increase in the charge associated with Ca stripping (220 *vs.* 28 mC cm^{-2}) and decrease of the polarization (i_{pa}-i_{pc} = 250 *vs.* 670 mV) are observed in the 0.45 M $Ca(TFSI)_2$ in EC:PC (red curve) electrolyte when compared to the one employing BF_4^- (blue curve).

This difference in reaction kinetics is attributed to the different solvation environment of calcium cations in the two electrolytes. As described in Chapter 3, the TFSI based electrolyte is expected to present much lower degree of ion pairing than the corresponding one employing BF_4^-. As the solvation shell in the former case will be composed entirely by solvent molecules, the desolvation of the cation (a required step prior to metal plating) will be less penalized energetically resulting in faster kinetics. This difference in plating kinetics is further supported by the difference in binding energy between Ca^{2+} and a solvent molecule and between Ca^{2+} and an anion (binging energy of Ca^{2+}-EC = 380 kJ mol^{-1} and Ca^{2+}-TFSI = 1162 kJ mol^{-1} reported in Ref. [106]). This experiment highlights the importance to optimize the electrolyte formulation, not only to produce ionically conductive surface layers, but also to minimize the desolvation energy of the divalent cations in solution.

4.4 SEI-forming additives

Given the previous results that suggest that the presence of a borate compound is responsible for the Ca^{2+} migration, a possible strategy to promote the borate-containing SEI layers is the addition of a boron-based additive. As has been studied before, SEI-forming additives must readily decompose upon reduction forming suitable decomposition products that enhance the overall performance of the SEI [151].

Trifluoroborate complexes ($BF_3 \cdot X$, X = cyclic or linear carbonate) were employed recently as additives for LIBs in $Li[Ni_xCo_yMn_zO_2]$ || graphite cells [152]. Higher capacity retention and lower cell impedance were reported when the additives were used with the 1 M $LiPF_6$ in EC:EMC (3:7 wt.%) electrolyte. While the SEI formed on the graphite electrode was not fully characterized, elemental analysis after cycling evidenced up to 8 at.% of boron, suggesting the presence of the trifluoroborate complex decomposition products in the SEI.

In this section, the use of a trifluoroborate complexes as additives in calcium-metal battery electrolytes is reported. Initially the use of commercial trifluoroborate-diethyletherate ($BF_3 \cdot DE$) is presented, and the influence of the additive content and of cycling conditions is evaluated to find the optimal operation parameters for the Ca plating/stripping. A second, related family of additives, using carbonate molecules instead of diethylether, is presented and preliminary results in their preparation and electrochemical characterization

are reported.

4.4.1 General comparison between $Ca(BF_4)_2$, $Ca(TFSI)_2$ and $Ca(TFSI)_2 + BF_3 \cdot$ diethylether electrolytes

Cyclic voltamogramms of a 0.4 M $Ca(TFSI)_2$ in EC:PC electrolyte, with and without the addition of 2wt.% of $BF_3 \cdot DE$, are shown in Figure 4.16. For the sake of comparison, the cyclic voltammogram measured in a 0.45 M $Ca(BF_4)_2$ in EC:PC electrolyte is also shown. As discussed before, without a pre-passivation step, the use of $Ca(TFSI)_2$ electrolyte results in the absence of any significant redox features given the blocking nature of the surface layer formed on the working electrode. By contrast, using an electrolyte containing $Ca(BF_4)_2$, a reduction wave can be observed with an onset potential at about -0.07 V *vs.* Ca^{2+}/Ca. This reduction process, ascribed to Ca plating, is at least partially reversible and the associated oxidation peak (Ca stripping) has an onset potential at *ca.* 0.14 V *vs.* Ca^{2+}/Ca.

By adding 2wt.% of $BF_3 \cdot DE$ to the $Ca(TFSI)_2$-based electrolyte, some intense reduction processes can be observed (orange trace in Figure 4.16). In the first cycle, sharp reduction peaks are present between 2.6 and 1.2 V *vs.* Ca^{2+}/Ca, attributed to decomposition of electrolyte components, promoted by the BF_3 additive, possibly involving gas evolution, which would explain the spikes in the reduction current. This electrolyte decomposition process continues during the entire cycling, generating a residual reduction current (similar to the observed before for $Ca(BF_4)_2$) which acts as a *background* for further

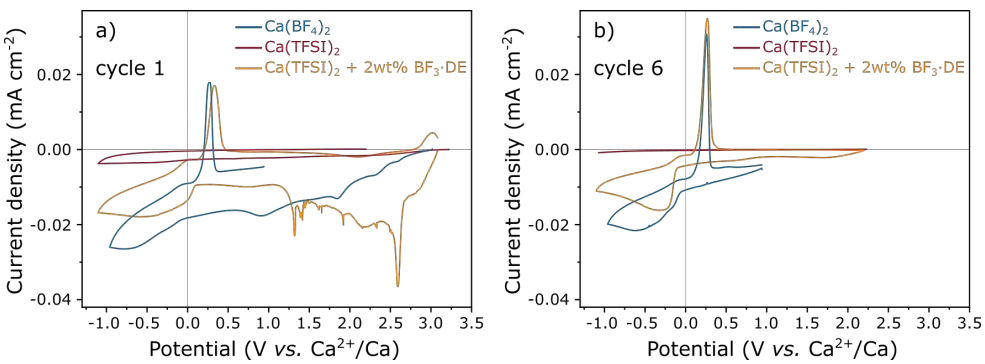

Figure 4.16: Cyclic voltammograms of 0.45 M $Ca(BF_4)_2$ and 0.4 M $Ca(TFSI)_2$ (with and without $BF_3 \cdot DE$ additive) in EC:PC electrolytes, over a SS electrode. a) 1st cycle, and **b)** 6th cycle. Measurements done at 100 °C and 0.1 mV s^{-1}. RE: Ag wire (calibrated with Fc^+/Fc), and CE: Ca metal.

reduction or oxidation processes. Compared to the case of $Ca(BF_4)_2$ electrolyte, the $Ca(TFSI)_2$ + $BF_3 \cdot DE$ system shows significantly lower residual reduction current, implying that the electrolyte reduction is more efficiently suppressed after the first cycles.

A second important reduction event starts at potentials slightly above 0 V *vs.* Ca^{2+}/Ca which involves more electrolyte reduction concomitant with calcium metal plating. The observation of Ca metal plating occurring at potentials above Ca^{2+}/Ca is ascribed to the low reproducibility of the Ag RE potential, as has been observed before. More details about the Ag RE calibration and possible shift during plating are presented in Chapter 6 - Experimental methods, page 122 or further down in this Chapter (page 93). In oxidation, a sharp peak is observed, corresponding to calcium metal stripping from the working electrode, comparable to the one observed in the $Ca(BF_4)_2$ electrolyte.

4.4.2 Optimization of additive content and cycling protocol

In order to better understand the impact of $BF_3 \cdot DE$ on Ca plating and stripping, several weight contents of the additive were tested. CVs obtained with 0.1, 0.5, 2, 4, or 8wt.% of $BF_3 \cdot DE$ are shown in Figure 4.17. Upon the first cathodic scan, a sharp reduction peak is observed at about 2.6 V *vs.* Ca^{2+}/Ca followed by broader reduction waves at lower potentials. The overall charge passed through the cell in the first cathodic scan (between OCV and -1.0 V *vs.* Ca^{2+}/Ca), increases with the amount of additive in solution with about -340, -400, -700, -1680 and -3320 mC for 0.1, 0.5, 2, 4, and 8 wt.% of $BF_3 \cdot DE$ respectively. Upon the first anodic scan, clear Ca stripping peaks were only observed with 0.5 and 2 wt.% $BF_3 \cdot DE$ solutions. For electrolytes containing 2 wt.% or more, a residual reduction current can be seen after the Ca stripping peak above 0.5 V *vs.* Ca^{2+}/Ca.

Upon cycling, the residual reduction current significantly decreased, indicating the formation of an effective passivation layer and/or the consumption of the additive in solution. In the meantime, the Ca stripping peaks evolved differently depending on the initial additive content. The stripping current decreased significantly after six cycles in the solution containing 0.5 wt.% $BF_3 \cdot DE$ (Figure 4.17b). Further cycling resulted in featureless CV curves pointing at the formation of fully blocking passivation layers, similar to the 0.1 wt.% $BF_3 \cdot DE$ (Figure 4.17a) or the pure $Ca(TFSI)_2$ electrolytes. For higher additive content (2 wt.% and above) an increase in the stripping capacity

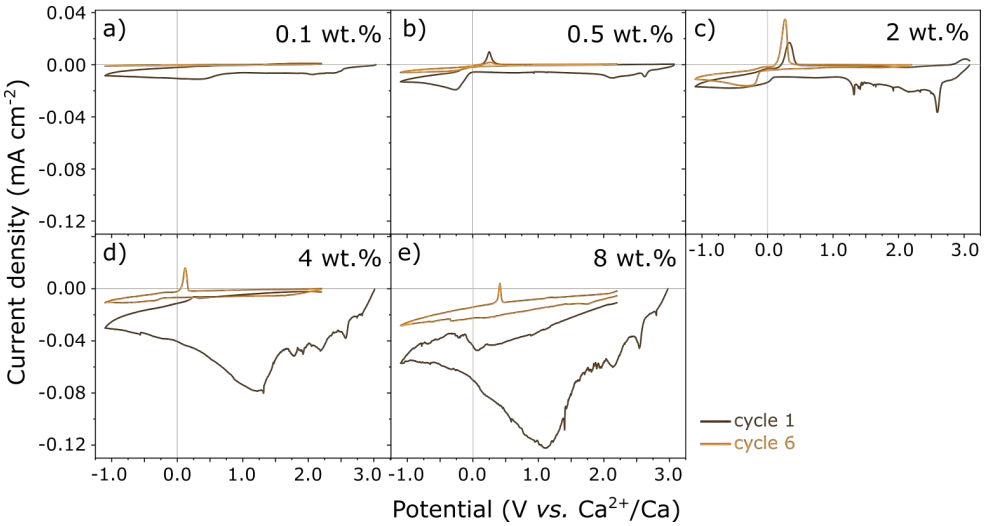

Figure 4.17: Cyclic voltammetry of a 0.4 M Ca(TFSI)$_2$ in EC:PC electrolyte with the addition of $BF_3 \cdot DE$ at different weight percentages. Cycling at 100 °C and 0.1 mV s^{-1} using Ca as CE and Ag as RE (calibrated against Fc$^+$/Fc). cycle 1: dark brown, and cycle 6: orange.

was recorded upon the first few cycles. Overall, the electrolyte containing 2 wt.% of $BF_3 \cdot DE$ was found to present the highest and most stable calcium stripping charge upon cycling and was selected as optimal concentration.

Another parameter that is expected to influence the SEI formation during reduction is the lower cutoff voltage during the CV, therefore different cutoff voltages on reduction were evaluated (-0.7, -1.1 and -1.5 V *vs.* Ca^{2+}/Ca, Figure 4.18a). The first effect observed by setting a more negative cutoff is that the residual reduction current decreases. This might be attributed to a time effect, as polarizing the cell towards lower voltage values increases the total time that the working electrode is held at reductive potentials, requiring less cycles to complete irreversible parasitic reduction processes such as SEI formation in order to achieve full electrode coverage.

Additionally, the cutoff voltage on reduction was found to impact the amount of calcium metal deposited per cycle. As a part of the current associated with the reduction wave is consumed in SEI formation, we estimate the amount of calcium deposited on each cycle by integrating the corresponding oxidation peak, which is supposed to correspond only to calcium stripping. For the first three cycles, rather similar stripping charge were recorded regardless of the cutoff voltage (between 20 and 27 mC, Figure 4.18b). However, a significant

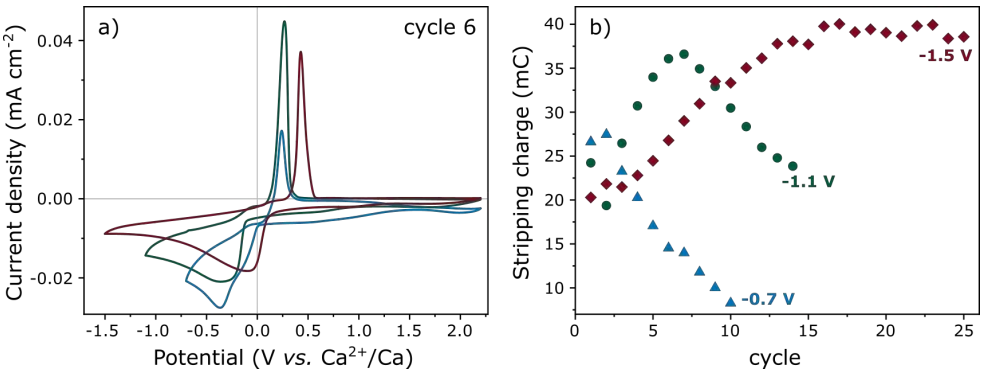

Figure 4.18: Effect of the reduction cutoff voltage in the cycling of a 0.4 M Ca(TFSI)$_2$ in EC:PC electrolyte containing 2 wt.% of $BF_3 \cdot$ DE. a) sixth cycle of the CV down to different reduction cutoff voltages, measured at 100 °C and 0.1 mV s^{-1} using SS as WE, Ca as CE, and Ag as RE (calibrated against Fc$^+$/Fc). **b)** Evolution of the stripping charge upon cycling depending on the reduction cutoff voltage.

drop of the stripping charge was observed for the cell cycling down to -0.7 V *vs.* Ca^{2+}/Ca while an increase was observed for -1.1 and -1.5 V *vs.* Ca^{2+}/Ca. Eventually, the charge decreases also for the cell cycling down to -1.1 V *vs.* Ca^{2+}/Ca with the highest obtainable charge being around 37 mC at the 7th cycle. When the cutoff voltage is set to -1.5 V *vs.* Ca^{2+}/Ca, the charge per cycle continuously increases until reaching a constant 40 mC at cycle 15 and above.

While the origins of the stripping charge decay observed for the cycling at -0.7 and -1.1 V *vs.* Ca^{2+}/Ca remain unclear, three possible reasons (or combination of these) can be foreseen:

1. Considering the poor reliability of the silver pseudo-reference electrode, any significant change in the electrolyte could result in a potential shift which could affect Ca plating. Even when the potential of the reference electrode was calibrated prior to the measurements (as described in the Methods section), an overall shift of the CV curves was observed in some cases during cycling (Figure 4.19), explaining, for example, why the plating begins at potentials higher than 0 V in the orange trace of Figure 4.16a.
2. Any increased overpotential for Ca plating during cycling would eventually result in limited Ca electrodeposition (depending on the lower cutoff voltage).
3. Applying a more negative potential to the working electrode promotes

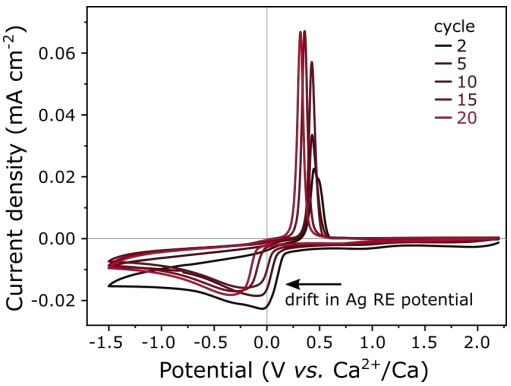

Figure 4.19: Evidence of the drift in the potential of the Ag wire used as reference electrode. CVs of a $Ca(TFSI)_2$ electrolyte in EC:PC containing 2wt.% of $BF_3 \cdot DE$ measured at 100 °C and 0.1 mV s^{-1}, and using SS as WE, Ca as CE, and Ag as RE. The potential of the reference electrode was calibrated with Fc^+/Fc prior to the measurement to convert it to Ca^{2+}/Ca scale.

the formation of a better-performing SEI layer which is able to sustain more cycles of Ca plating and stripping. Deeper studies are underway in order to characterize the SEI layer formed at different potentials, but preliminary results suggest that the additive promotes the decomposition of the carbonate solvent at reducing potentials, producing borate-containing solid layers that resemble the SEI formed in $Ca(BF_4)_2$ electrolyte.

4.4.3 $BF_3 \cdot$ carbonates as SEI forming additives

It has been shown that the addition of a commercial BF_3-adduct allows the reversible plating and stripping of Ca from a previously inactive $Ca(TFSI)_2$ electrolyte solution. It is believed that this effect is the result of the formation of a Ca^{2+}-conductive layer on the surface of the working electrode, possibly containing borate species in a polymeric matrix. However, the purity of the commercial adduct was observed to vary significantly between sources and between batches, which can impact the reproducibility of the experiments. Additionally, the $BF_3 \cdot DE$ is a volatile liquid which readily dissociates and releases $BF_{3(g)}$, posing a difficulty to its safe handling.

Alternatively, crystalline solids are obtained when BF_3 is complexed by a carbonate molecule, such as EC or PC. Previous reports on their preparation and use as additives in LIBs show improvement in the rate stability of LIB materials [152–154]. In this section, preliminary results on the prepa-

ration, characterization and electrochemical performance of some of these BF_3-carbonate complexes are presented.

4.4.3.1 Synthesis of the adducts

The materials were obtained following a previously reported method [152] and in the same fluorine line employed for the anhydrous synthesis of $Ca(BF_4)_2$ shown in Chapter 2, page 25. The reaction vessels consisted in a FEP tube (6 mm inner diameter, 21 cm long; V = 5.9 mL) equipped with a PTFE valve. The reaction vessels were passivated with F_2 prior to use. Typically, ∼170 mg (∼1.9 mmol) of the corresponding liquid carbonate (or lactone) were loaded in the reaction vessel inside a nitrogen-filled glovebox. The reaction vessel was then connected to the vacuum line, cooled down in a liquid-nitrogen bath and evacuated to remove the inert gas inside.

Stepwise additions of ∼0.4 mmol of BF_3 were condensed into the FEP reaction vessel using a liquid-nitrogen bath. The reaction vessel was warmed up slowly after each addition to allow complete reaction and to follow its evolution (Figure 4.20). In all cases, the initially clear solution turns into a cloudy suspension after the initial addition steps. The fraction of solid in the reactor increases as the addition continues. A complete consumption of the BF_3 after each addition was evidenced by a negligible vapour pressure (< 5 torr) inside the reactor.

After the equivalent point was reached, the reactor was left overnight with a slight overpressure of BF_3 (∼50 torr, 0.02 mmol). The vessel was then evacuated, transferred to a glovebox and the solid product was slightly ground with a metallic rod. A final addition of ∼0.4 mmol of BF_3 was done and the

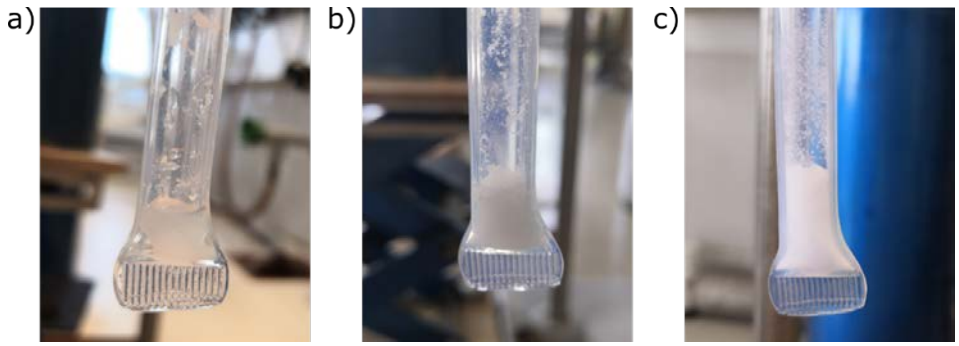

Figure 4.20: Evolution of the reaction between DMC and BF_3. Reaction vessel after the addition of **a)** 0.4eq. of BF_3, b) 0.8eq. of BF_3, and **c)** 1eq. of BF_3.

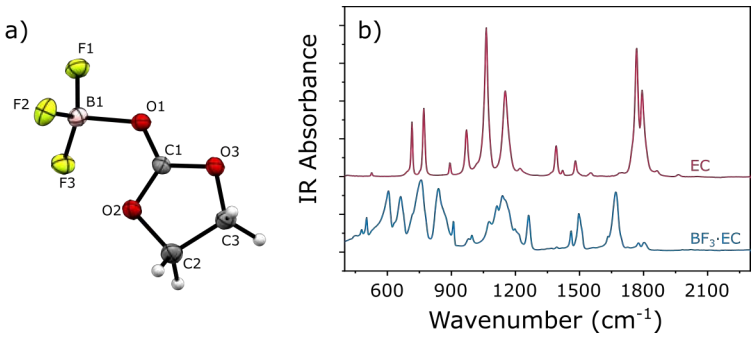

Figure 4.21: Characterization of the prepared $BF_3 \cdot EC$ adduct. **a)** Structure obtained by single-crystal XRD. Ellipsoids are drawn for a probability of 50%. C, grey; F, light green; O, red; B, pink. **b)** IR spectra of the pure EC and the obtained solid $BF_3 \cdot EC$ adduct

reaction was left for 24 h to ensure completeness. The vessels were then fully evacuated at -20 °C to avoid the decomposition of the solid complex and transferred to the glovebox. The white solid was recovered in all cases and stored until further analysis.

4.4.3.2 Characterization

Before the last grinding step, crystals of good quality were collected and analysed by single-crystal XRD at 150 K and under a protective nitrogen flow. Special care was taken to avoid any exposure to oxygen or water from the atmosphere, as it would provoke the decomposition of the product. The refined molecular structure of the adduct is presented in Figure 4.21a, confirming the formation of the desired adduct. The refining parameters are presented in Annex 2 and agree with the previously reported orthorhombic crystal structure (CCDC 1972338) [152].

The solid product was analysed by ATR IR inside the glovebox and the IR spectrum obtained is shown in Figure 4.21b, together with the spectrum of pure EC. Compared to the IR spectra reported previously in the literature [152], the one presented here shows much lower presence of unreacted EC which allows better interpretation.

The C=O stretching vibration of the adduct shows a redshift of 127 cm^{-1} units from the original 1795 cm^{-1} position of the pure EC. This important displacement is the result of the bonding of the BF_3 trough the carbonyl oxygen, which produces a decrease in the electronic density in the C=O double

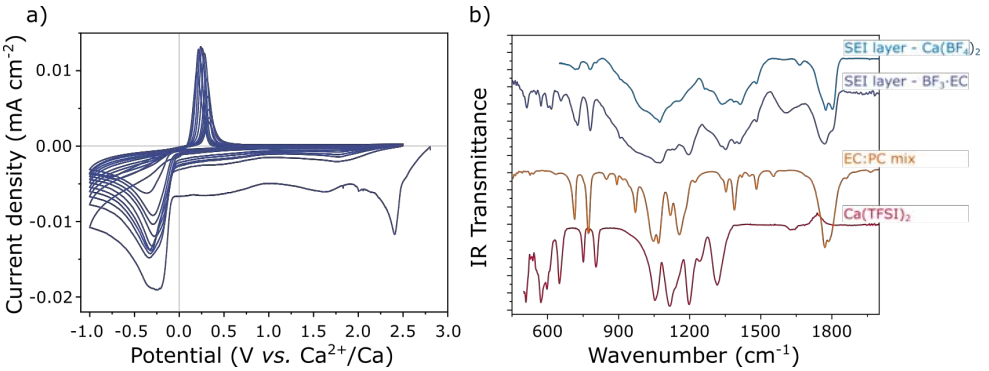

Figure 4.22: Electrochemical behaviour of a 0.4 M Ca(TFSI)$_2$ in EC:PC electrolyte after the addition of 1 wt.% BF$_3$ · EC a) CV over a SS working electrode, at 100 °C and 0.1 mV s^{-1}, and using Ca as CE and Ag wire as RE (calibrated with Fc$^+$/Fc). **b)** IR spectrum of the deposit surface layer on the working electrode after cycling, compared to the surface layer produced in the Ca(BF$_4$)$_2$ based electrolyte (without additive).

bond and a subsequent bond elongation, from 1.188(3) Å for pure EC to 1.2500(16) Å in BF$_3$ · EC [155]. The vibrational modes associated with the BF$_3$O− group were assigned by comparison with other similar BF$_3$ adducts [152, 156], and to the reported BF$_{3(g)}$, which only present three active bands located at 482, 719, and 1504 cm^{-1} [157, 158]. The bands located at 603, 775 and 1136 cm^{-1} are attributed to vibrations involving the terminal BF$_3$, and the band at 840 cm^{-1} to the stretching of the B−O bond.

4.4.3.3 Electrochemical behaviour

The behaviour of BF$_3$ · EC as additive for calcium plating was tested using similar conditions than previously for BF$_3$ · DE, that is, cycling at 0.1 mV s^{-1} and 100 °C down to -1 V *vs.* Ca^{2+}/Ca (-4.2 V *vs.* Ag wire) using a concentration of 1 wt.%. The CV obtained for a 0.4 M solution of Ca(TFSI)$_2$ in EC:PC containing BF$_3$ · EC is shown in Figure 4.22a. Compared to the CV obtained using the commercial additive (BF$_3$ · DE), the reduction process presents far less noise, which would be related to a lower production of gas bubbles. However, the charge density for both plating and stripping is lower than the previous case, which suggests that the concentration and cycling conditions for this additive would need to be further optimized.

After cycling, the SS working electrode was recovered, washed and analysed by IR spectroscopy. Figure 4.22b shows the obtained spectrum, compared to the individual components of the electrolyte solution (EC:PC mixture and solid

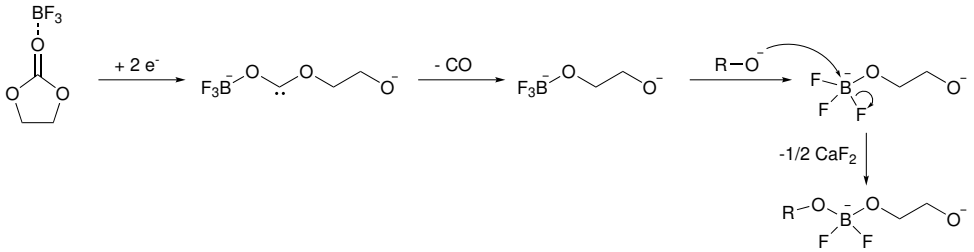

Figure 4.23: Proposed mechanism for the formation of cross-linked boron polymers by BF_3-promoted EC decomposition.

$Ca(TFSI)_2$). Remarkably, the SEI formed in the $Ca(TFSI)_2$ electrolyte after the addition of the $BF_3 \cdot EC$ additive highly resembles the one produced in the $Ca(BF_4)_2$ electrolyte (without additives) described in Section 4.3 and shown in Figure 4.22 for comparison. This finding suggest that the SEI produced in this case is composed by similar boron-containing polymers, although the profile of the band between 1250-1550 cm^{-1} presents a different shape. As the B−O vibrations are expected to lie in this range, it is possible that the exact molecular structure of the boron polymers formed in this case is different than the one produced in the $Ca(BF_4)_2$ electrolyte.

Regarding the mechanism for the SEI formation, it is expected that the bonding to such a strong Lewis acid, like BF_3, would promote the reductive ring opening of the EC molecules (Figure 4.23). This effect has been observed, for example, in the favourable reduction of solvent or anions participating in the solvation shell of a metal cation (which also behaves as a Lewis acid) [159]. After the ring opening, the boron centre can be further attacked by a nucleophilic group, *e.g.* an alkoxide produced by EC or PC decomposition [150, 160], releasing F^- which precipitates as CaF_2.

BF_3 is not the only Lewis acid which is expected to behave this way, other electron acceptors can promote the reductive decomposition of solvent molecules and influence the formation of the SEI layer. For example, *tris*(pentafluorophenyl)borane (TPFPB) has been extensively studied as additive in LIB electrolytes [161], where it enhances the solubility of LiF (an undesired SEI product). However, on the light of the present results, we believe that TPFPB can also bind to the carbonate solvents and promote their decomposition, affecting substantially the SEI, far beyond the simple LiF dissolution.

4.5 Summary and Conclusions

Given the very low redox potential of a metallic calcium electrode, it will tend to reduce the electrolyte which is put in contact with. The reduction of the electrolyte solution (composed by solvent + salt + additives) can result in two different scenarios: *i)* formation of soluble and/or gaseous products, like is probably the case for $Ca(TFAB)_2$ based electrolytes, in which the surface of the electrode is not passivated and a continuous reduction of the electrolyte occurs; and *ii)* formation of insoluble products which accumulate on the working electrode forming a surface layer, which is the case of both $Ca(TFSI)_2$ and $Ca(BF_4)_2$ based electrolytes.

If the surface layer generated is not ionically conductive, further electrochemical reactions are completely blocked. This is the case of the $Ca(TFSI)_2$-derived passivation layer, composed mainly of $CaCO_3$ and other inorganic species - product of the carbonate solvent decomposition. On the contrary, if the surface layer is ionically conductive, calcium plating and stripping can be achieved with higher or lower rate depending on its conductivity. This is the case of the $Ca(BF_4)_2$ based electrolyte, where Ca^{2+} migration is aided by the presence of some borate polymer - product of anion decomposition.

Remarkably, the origin of the surface layer components (either anion or solvent decomposition) appears to be linked to the solvation shell of the cations in solution. This relation between cation solvation shell and SEI composition on the metal has gained much attention recently and opens a way for SEI-engineering through solvation shell manipulation, that has been so far unexplored in the field of lithium-ion batteries.

It was shown, additionally, that if a suitable SEI layer is pre-formed by electrochemical means, for example, it could be transferred to other electrolytes and allow metal plating and stripping. In this case, the reaction kinetics are governed by the desolvation energy barrier of the cation. Unfortunately, the passivation layer formed in this study was not enough to prevent further electrolyte decomposition, and the electrochemical response diminishes quickly after few cycles. Further optimization of the passivation protocol is needed to produce more stable, and more homogeneous, SEI layers that can be easily transferred between different electrolyte solutions. Alternatively, other treatment methods can be developed to produce borate-containing artificial SEI layers which may allow Ca^{2+} migration.

Lastly, a family of BF_3-adducts was proposed as additives for calcium-metal

batteries, as they promoted the formation of borate polymers on the metal electrode. Although this kind of additives has been previously suggested to increase the cycle life of lithium-ion batteries, their role in the SEI formation was never elucidated. This results pave the way for other Lewis acid molecules to be considered as SEI-forming additives in calcium and other battery chemistries.

5

Conclusions and Perspectives

The formulation of electrolytes for divalent metal batteries, *i.e.* the mixture of salt, solvent and additives, was studied from three complementary points of view: development of new salts, optimization of macroscopic properties, and electrochemical compatibility with Ca and Mg metal electrodes.

From the point of view of the salt, it was evidenced that the BF_4^- anion displays a particular tendency to hydrolysis in the presence of Ca^{2+} (and presumably Mg^{2+}), especially at elevated temperatures. This impedes the preparation of dry electrolytes by simple thermal methods and results in significant contamination from soluble hydrolysis products. Therefore, several anhydrous synthesis routes were explored to produce battery-grade Ca-salts. The methods employed can easily be extended to other calcium salts or the magnesium analogues and thereby provide a broader range of possibilities for electrolyte development.

Furthermore, tailoring the salt concentration allowed optimization of the electrolytes' ionic conductivity. Maxima are obtained, for divalent cations in EC, PC, or DMF electrolytes, for concentrations of *c.a.* 0.5 M. Further increasing the salt concentration causes a decrease in the ionic conductivity attributed to a combination of increased electrolyte viscosity and tendency to form ion pairs. The formation of ion pairs in the electrolyte was studied by Raman spectroscopy and Walden plot analysis, evidencing the fundamental role of the solvent's donor number and relative permittivity in the formation of contact ion pairs (CIPs) and solvent-separated ion pairs (SSIPs). While high donor number solvents bind more strongly to the cation and prevent CIP formation, a high relative permittivity is required to effectively shield the cation charge and decrease the probability to form SSIPs. Further studies are needed to understand the evolution of these parameters at different temperatures, particularly in solvents with low relative permittivity, as ethers or glymes, where

an unexplained decrease in the ionic conductivity was observed upon heating.

The concept of ionicity, normally understood as the fraction of ions available to transport charge, needs to be further studied for divalent cation electrolytes. Given that the ion pairs in these systems are globally charged species, they will contribute to the mass and charge transport from one electrode to the opposite during battery charge or discharge. This is in stark contrast to monovalent systems, where a high proportion of free ions are often targeted and for which ion pairs are neutral and strongly undermine ionic conductivity. The contribution of both forms of ion pairs (CIPs and SSIPs) needs to be taken into account, for example, when measurements of cation transference numbers are attempted.

Two effects of the solvation shell of the cation in the operation of negative electrodes for Ca batteries were clearly evidenced. First, decreasing the interaction energy of the cation with the ligands of its solvation shell produces an increase in the kinetics of the reaction occurring at the surface of the electrode, this reaction being either metal plating or cation intercalation, as evidenced by a decrease in polarization and an increase in peak current density during cyclic voltammetry. Second, it was observed that the nature of the solvating molecules and their tendency to decompose will impact the formation of surface layers, particularly at the anode. A direct link between the composition of the cation solvation shell and the SEI formed was presented.

Finally, the formation of passivation layers, derived from electrolyte decomposition, over calcium electrodes was studied. It was evidenced that a borate-rich passivation layer allows for ionic conduction and is beneficial for metal plating and stripping. This borate-rich layer may be produced by anion decomposition, or by including a suitable SEI-forming additive, as demonstrated herein. Although its exact chemical composition is not fully elucidated, it is suggested to be composed by a trigonal boron-crosslinked polymer.

Although in this study the SEI layer was formed *in situ* by electrochemical methods, the possibility of applying an ionically conductive boron polymer as artificial coating for Ca or Mg metal anodes is envisioned. For this purpose, a suitable boron polymeric matrix needs to be developed and its divalent cation conductivity optimized. If successful, the application of such an artificial SEI would promote the use of calcium and magnesium metal anodes in rechargeable batteries.

6

Experimental Methods

In this chapter, a brief introduction on each experimental technique employed in this thesis is presented. Instead of a detailed description of the apparatus employed, the focus is set on the physical or chemical phenomena governing each technique and the information it can provide, or more specifically, the information that was obtained from each one in this thesis. A summary of them is reported in Table 6.1.

Table 6.1: Summary of the experimental techniques employed in this thesis.

Technique		**Used to characterize:**
Spectroscopies	Infrared (IR) & Raman	New salts and additives, and composition of the SEI layers
	X-ray Photoelectron (XPS)	Composition of the SEI layers
	Nuclear Magnetic Resonance (NMR)	New salts and additives, and concentration of BF_4^- in solution
	Electron energy-loss (EELS)	Composition of the SEI layers
Transmission electron microscopy (TEM)		Morphology of SEI layers
X-ray diffraction (XRD)		New salts and additives
Elemental analysis (EA)		New salts and additives
Mass Spectrometry (MS)		New salts and additives

Technique		Target:
Electrochemical	Karl-Fischer coulometric titration	Water determination in electrolytes or salts
	Ionic conductivity determination	Properties of electrolytes
	Conventional techniques	Oxidation/reduction stability of electrolytes, metal plating evidence
Density and viscosity determination		Properties of electrolytes

A more extensive description is provided to techniques that played a significant role throughout the thesis, like IR and Raman, or to the ones where non-standard setups were used. Some details about data manipulation are also provided when needed. At the end of each section, the exact experimental parameters and equipment models used for data acquisition are presented.

6.1 Spectroscopic techniques

6.1.1 Vibrational Spectroscopy

Infrared (IR) spectroscopy measures a sample's absorption of electromagnetic radiation in the IR range of the spectrum (100 - 13000 cm^{-1}; or 12 meV - 1.6 eV). In turn, Raman spectroscopy measures the scattering of light (in the same IR range) when a sample is irradiated by a high intensity laser. In this energy region, excitations between different vibrational states are observed, and thus an absorption/scattering event (*i.e.* a peak in the respective spectrum) can be correlated with a determined vibration mode of the molecule or material.

When studying small molecules, it is useful to consider the symmetry aspects governing its vibration modes. For example, let's consider a trigonal planar BF_3 molecule. As each atom, in principle, can move in the three spatial dimensions x, y, and z, the system has a total of 12 degrees of freedom. However, some of this motions will result in the translation or rotation of the entire molecule, and so they are not observed in the energy region studied by IR or Raman. Then, only four fundamental vibration modes are expected (Figure 6.1), with the Mulliken symbols: $A_1^{'} + 2E^{'} + A_2^{''}$ [162, 163].

Given the selection rules for IR and Raman, not all vibrations will be visible

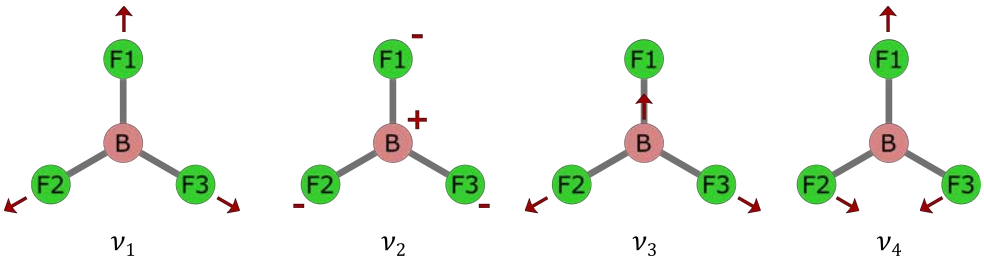

Figure 6.1: Fundamental vibrational modes of the BF_3 isolated molecule. Arrows indicate movement of atoms in the plane, while - and + signs indicate movement in or out of the plane.

by both techniques. The intensity of a band in IR is proportional to the change in polarization of the molecule caused by the vibration involved. As consequence, ν_1 is completely inactive, as the polarization of the molecule remains as zero. In turn, a band in a Raman spectrum is proportional to the change in polarizability of the molecule produced by the vibration. In this case, ν_1 is Raman inactive, as the vibration does not involve any change of bond lengths.

As a result of the symmetry of such system, a bending in the F2-B-F3 bond, as depicted in ν_1 mode in Figure 6.1 is equivalent to a bending of the F1-B-F2. However, if the F1 atom is replaced by other atom or groups of atoms, these two vibrations are not equivalent, and a splitting in the respective IR or Raman band is observed. A similar case would be presented, hypothetically, if the molecule coordinated a cation by one or two fluorine atoms, cause a distinctive splitting in the vibration associated with such atoms. This type of analysis was used in this thesis in some instances, to assign different vibrations bands observed in IR of compounds containing BF_4^- anions or $[BO_3]$ or $[BO_4]$ moieties.

For big molecules, however, the symmetry analysis becomes too complex to be convenient. In these cases, the bands in IR and Raman spectra are attributed to a particular bond stretching or bending. For example, in the spectrum of ketones, aldehydes and similar, it is common to observe the C=O bond stretching at 1650-1800 cm^{-1} depending on the structure of the rest of the molecule [164]. Other relevant bond vibration frequencies, useful for the interpretation of IR spectra of this thesis, are listed in Table 6.2.

Table 6.2: Typical frequency ranges observed for some relevant bond vibrations in IR and Raman spectroscopy.

Vibration	Typical frequency range (cm^{-1})[a]
O−H str.	3600-3700
C−H str. (aliphatic)	2850-3000
C−O−C str. (ethers)	1100
C−O str. (esters)	1100-1300
C=O str. (very strong)	1650-1800
C=C str. (weak or absent)	1650
C≡C str.	2000-2500
$-CH_3$ bend. (assymetric)	1475
$-CH_3$ bend. (ssymetric)	1380
CH_2 bend. (scissoring)	1465
CH_2 bend. (rocking)	720
CH_2 bend. (wagging)	1305
CH_2 bend. (twisting)	1300
H−O−H bend. (assymetric)	1645
B−O str.	1310-1380

[a] taken from ref. [164]

IR spectroscopy was employed in this thesis as a qualitative tool to assess the molecular structure of new products, to evaluate the coordination mode of different anions in solid and liquid samples, and to characterize the decomposition products formed on the surface of a working electrode after electrochemical tests. Complementarily, Raman spectroscopy was chosen for quantitative analysis. In this case, the obtained spectra were fitted to a series of Voigt peaks as illustrated in Figure 6.2. A Voigt peak, which is a convolution of a Gaussian and a Lorentzian function, was chosen as it gives the best description of the experimental peak broadening [165].

The area obtained for each band is proportional to the concentration of the corresponding chemical species and to the Raman activity (RA) of the vibration mode as: Area $= RA * c_i$. As mentioned before, the intensity (activity) of a vibration mode in Raman is a function of the polarizability change of the molecule as a result of the vibration, and can be calculated by DFT methods,

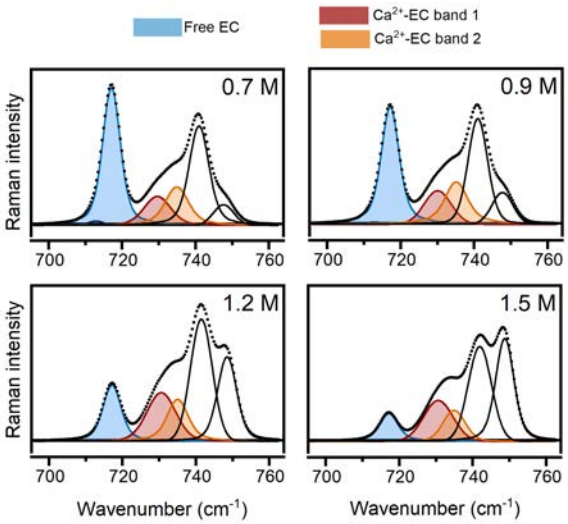

Figure 6.2: Example of Raman peak fitting. Raman spectra of $Ca(TFSI)_2$ electrolytes in EC, at different salt concentrations. The experimental data (scatters) were fitted by a series of Voigt peaks attributed to the vibration modes of different species in solution

allowing the quantification of the different species in the sample based on the Raman spectrum [106]. The Raman activity of a particular mode, additionally, is expected to be different if the molecule is *free* or if it is coordinated to a cation in solution, as the coordination will affect substantially the electron density of the different bonds, and thus, their polarizability. A parameter introduced in this thesis to account for such polarizability change is denoted θ ($= RA_{\text{coord}} \,/\, RA_{\text{free}}$). A summary of the values of θ used in this thesis is presented in Table 6.3, there were either taken from previous reports or calculated by Dr. Rafael Barros Neves de Araújo from Chalmers University of Technology.

Table 6.3: Summary of Raman Activity parameters used for quantification.

Electrolyte	Band	Band location (cm^{-1})		Raman shift (cm^{-1})	θ
		free species	coord. species		
$Ca(TFSI)_2$ in PC	PC C=O def.	712	720	8	2.2[a]
			725	13	
	TFSI breathing	740	748	8	1.0[b]
$Ca(TFSI)_2$ in EC	EC C=O def.	717	730	13	–
			735	18	

Electrolyte	Band	Band location (cm^{-1}) *free* species	Band location (cm^{-1}) coord. species	Raman shift (cm^{-1})	θ
	EC ring def.	894	907	13	1.4[c]
	TFSI breathing	741	748	7	1.0[b]
$Ca(TFSI)_2$ in DMF	DMF O=C−N bend.	658	670 676	18 24	0.9[a]
$Ca(TFSI)_2$ in FEC	FEC ring def.	905	925	20	1.1[a]
$Mg(TFSI)_2$ in EC	EC C=O def.	712	735	23	–
	EC ring def.	894	909	15	1.4[c]
	TFSI breathing	740	745	5	1.0[b]

[a] calculated by DFT methods.
[b] calculated from data taken from Ref. [130]
[c] assumed

Experimental conditions:

Two different setups were used to acquire IR spectra: *i)* for powder or liquid samples, a Jasco FT/IR-4700 Spectrometer was used with a universal ATR Pro One accessory (equipped with a diamond crystal) for the range 500-4000 cm^{-1} at a resolution of 2 cm^{-1}. Spectra were averaged over 64 consecutive measurements; *ii)* for analysis of surfaces, a Vertex 70 Spectrometer was employed, using a praying mantis diffuse reflectance accessory (HARRICK - DRP-ASC) to prevent any air exposure (Figure 6.3). To improve the spatial resolution of the FTIR instrument, a Vector 70 spectrometer was coupled to a Hyperion 3000 microscope to perform Synchrotron-based FTIR microspectroscopy measurements at the MIRAS beamline of the ALBA synchrotron light source (Barcelona, Spain). The microscope is equipped with a liquid N_2 cooled HgCdTe 50 μm MCT detector and uses a 36X Schwarzschild objec-

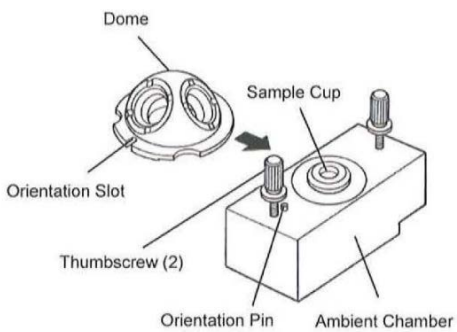

Figure 6.3: Ambient chamber used for IR measurements of the SS and Ca surfaces without air exposure.

tive (NA=0.52). The spectra were obtained in trans-reflection mode, using a masking aperture size of 50 μm x 50 μm. Raster scanning maps were collected in the mid-IR range (700-4000 cm^{-1}) at a spectral resolution of 4 cm^{-1} with 256 co-added scans per spectrum.

Regarding Raman, spectra were recorded using a Bruker MultiRAM FT-Raman spectrometer with a spectral resolution of 2 cm^{-1} using a Nd:YAG laser (1064 nm, 500 mW) as the excitation source. Data were typically averaged over 500 scans and recorded at 40 °C for the carbonate-based electrolytes and 25 °C for the DMF-based electrolytes. All bands in the resulting spectra were fitted as Voigt functions, typically with a unity Gaussian/Lorentzian mix by width, using Origin Software.

6.1.2 X-ray Photoelectron Spectroscopy

X-ray Photoelectron Spectroscopy (XPS) is a surface analytical technique that provides quantitative measurements of the elemental composition, stoichiometry, and chemical state of the present elements (*i.e.* their oxidation state and chemical bonds). In XPS, a beam of X-rays with energy $h\nu$ is pointed at the sample, causing some electrons to be ejected from the core levels of the atoms in the material (Figure 6.4). The kinetic energy of the electrons ejected (so called photoelectrons) correspond to the difference between the energy of the incoming X-rays and their original binding energy in the corresponding core shell. Plotting of the number of electrons detected (counts) as function of their binding energy results in a series of peaks in the XPS spectrum, which position varies depending on the chemical element and its chemical environment. For example, a clear difference is observed between the fluorine atoms in a $-CF_3$ group and the fluorine atoms in an inorganic crystal, as CaF_2.

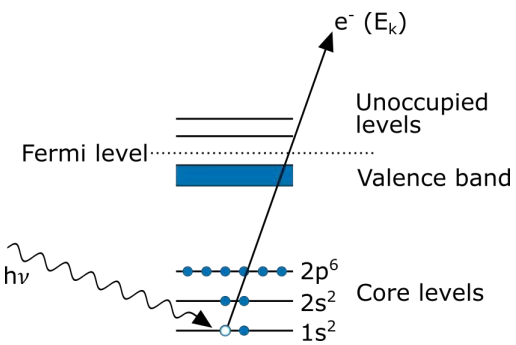

Figure 6.4: Scheme of the XPS process.

Given the short inelastic-mean-free-path of the photoelectron in the sample (∼10 Å), XPS is a surface-sensitive technique, providing little information about the bulk of the material.

Here, XPS was used to analyse the surface of the SEI layers formed in Ca and Mg electrodes after negative polarization in different electrolyte solutions. Previous to the analysis, the electrodes were washed several times by immersing them in DMC and drying them under vacuum. The samples were stored in a Ar-filled glovebox and transferred to the XPS chamber without exposure to air. The XPS experiments were performed in collaboration with Dr. Rémi Dedryvère from the Institut des Sciences Analytiques et de Physico-Chimie pour l'Environnement et les Matériaux (IPREM) in France. A Thermo Scientific Escalab 250 Xi spectrometer was employed, using a focused monochromatic radiation at two different photon energies: Al Kα (hν = 1486.6 eV) and Ag Lα (hν = 2984.2 eV). The analysed area of the samples was an ellipse with dimension of 450 × 900 μm^2. The binding energy scale was calibrated from the hydrocarbon contamination using the C 1s peak at 285.0 eV.

6.1.3 Nuclear Magnetic Resonance Spectroscopy

Nuclear Magnetic Resonance (NMR) spectroscopy is an analytic technique that probes the chemical environment of an atomic nuclei by studying the interaction between the nuclear magnetic momentum and an externally applied magnetic field. NMR experiments typically consist in three steps: *i)* alignment of the magnetic nuclear spins in an applied, constant magnetic field, *ii)* perturbation of this alignment of the nuclear spins by an oscillating magnetic field, referred as radio-frequency pulse, and *iii)* Detection of the electromagnetic waves emitted by the nuclei as a result of this perturbation [166].

Fourier transformation of the time-domain response results in the typical representation in frequency-domain, with the so-called chemical shift (δ [ppm]) in the x axis of NMR spectra (ppm = Hz/MHz). The moving electrons around the atom nuclei result in a shielding of the externally applied magnetic field. As this shielding is strongly dependent on the chemical environment of the atom, NMR spectroscopy is a suitable technique to investigate the molecular structure of an analyte.

NMR spectroscopy was employed in this thesis in two instances. Initially, it is used to characterize the synthesized salts by different synthetic routes. In

this case, ∼50 mg of the solid product were dissolved in 0.6 mL of $(CD_3)_2OS$. The ^1H, ^{13}C, ^{11}B, ^{19}F spectra were acquired on a Bruker Avance III 400 MHz NMR spectrometer. ^1H and ^{13}C NMR spectra were calibrated using the residual internal $(CH_3)_2OS$ (δ_H 2.54, δ_C 39.52) [167].

Quantitative NMR (qNMR) measurements were performed in order to determine the number of solvent molecules in the crystal structure of some of the salts prepared. To do so, a precise amount of EC was mixed with the salt in the $(CD_3)_2SO$ solution, and the ^1H was acquire for sufficient time (2.5 s) to ensure complete recovery of the signal (Figure 6.5).

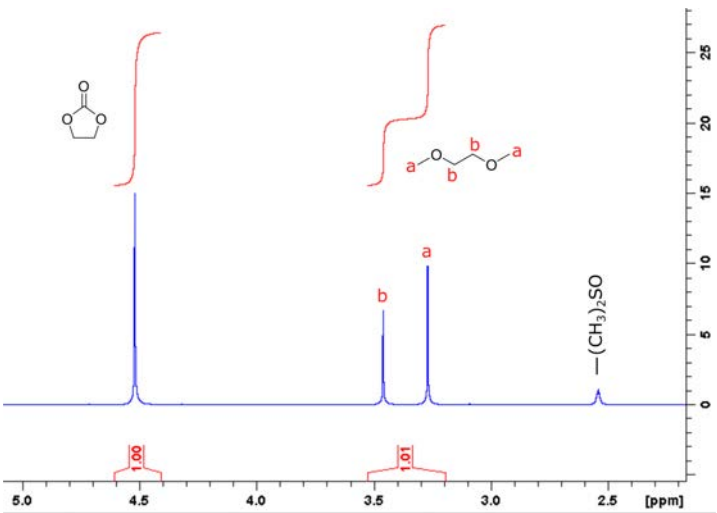

Figure 6.5: Example the determination of DME in a solid compound by means of ^1H qNMR.

The amount of DME in the original solid sample was calculated using the relation:

$$\frac{I_{EC}}{I_{DME}} = \frac{H_{EC}c_{EC}}{H_{DME}c_{DME}} = \frac{H_{EC}n_{EC}}{H_{DME}n_{DME}} \tag{6.1}$$

Where I_i is the area of a signal attributed to a molecule i, H_i is the number of protons in its chemical structure, and c_i is its molar concentration. Given that both compounds are in the same solution, the ratio between concentrations is equivalent to the ratio between the number of moles of each compound, n_i.

The same procedure was used to determine the concentration of $Ca(BF_4)_2$ electrolytes, employing LiBOB as internal standard and measuring the ^{11}B spectra. In this case, the T1 relaxation time measured was 11.5 ms for the BOB anion and 53.9 ms for the BF_4^- anion. The acquisition time for the

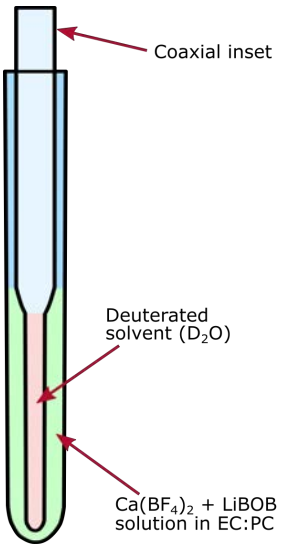

Figure 6.6: Setup for the NMR analysis of $Ca(BF_4)_2$ electrolytes. The deuterated solvent is put in a coaxial inset to avoid direct contact with the sample.

quantification was set to 0.5 s to allow a complete recovery of the signal. To avoid the mixture with a deuterated solvent, which may affect the properties of the $Ca(BF_4)_2$ electrolyte, a NMR tube coaxial inset was used, as shown in Figure 6.6. As a deuterated solvent is needed for locking of the magnetic field (locking of the field is necessary to avoid drifts during the measurement), the coaxial inset was filled with a D_2O.

6.1.4 Electron energy-loss spectroscopy

Electron energy-loss spectroscopy (EELS) measures the energy distribution of electrons that have interacted with a specimen and lost energy due to inelastic scattering. The difference between the energy of the incident beam and the collected electrons, denoted energy-loss, provides information about the electronic or vibrational states of the atoms in the material [168].

One of the prominent inelastic scattering effects that can give rise to a loss in the energy of the incoming electrons is the electronic excitation from a core-shell electron of an atom in the sample, a similar phenomenon that the one depicted for XPS in Figure 6.4. In this sense, EELS provide comparable information to X-ray absorption spectroscopy (XAS) and XPS. Also in this sense, EELS provide chemical composition and chemical bonding information, as atoms of different elements differ in their electronic states.

In this thesis, EELS was used to study the surface layers formed on the working electrode after electrochemical test. The EELS spectra were collected

together with the TEM images, so that the sample preparation and handling was the same (see details in Section 6.2. The measurements were performed using a TECNAI F20-S-Twin operating at 200 kV and equipped with an electron energy loss Spectrometer (EELS) GIF Tridiem in post column. The acquisitions of the energy-loss near-edge structures (ELNES) were performed in diffraction or scanning transmission electron microscopy (STEM) modes. The reported measurements were performed using an energy resolution of 1-1.2 eV and determined by measuring the full-width at half maximum of the zero-loss peak. The following conditions were used to acquire the EELS spectra: a dispersion of 0.2 eV/ch, a convergence angle of 5.8 mrad and a collection angle of 21.7 mrad, respectively. For the core loss of the B and the Ca K-edges, the background was subtracted considering a power-law function [169]. The multiple scatterings were removed using the Fourier-ratio method and energy correction was performed with respect to the C K-edge of amorphous carbon, whose main feature is at ∼285 eV. To limit the irradiation effect and give reliable results, the TEM/EELS investigations were done in low dose mode and using specific tunings determined after a prior irradiation study on the samples. The tuning and the analyses were also performed on different areas to avoid unnecessary irradiation on the area of interest.

6.2 Transmission electron microscopy

A transmission electron microscope (TEM) is a type of microscope in which an electron beam is focussed onto a sample, producing a highly magnified image from the transmitted beam. The shorter wavelength of the electron beam, compared to the visible light, allows imagining with much higher spatial resolution than the optical microscopes. Additional to transmission, the electron beam can also be diffracted by the material in the sample, giving rise to an electron diffraction pattern. Thanks to the ability to focus the electron beam in very narrow areas, the crystalline structure can be studied with extreme spatial resolution (∼10 nm^3) [170].

Both features, imagining and diffraction, were employed in this thesis to study the deposited surface layer on top of a working electrode after electrochemical treatments, as has been previously used in to study similar cases for lithium batteries [171].

The observation by TEM of the surface layer deposited on top of a metallic electrolyte is not straightforward, as the sample is required to be thin enough

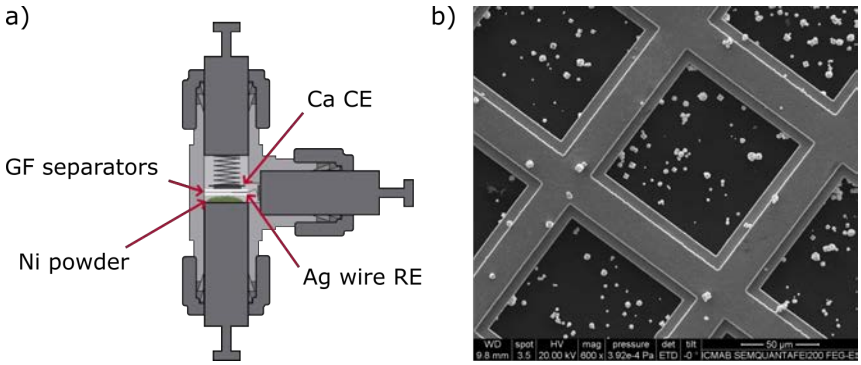

Figure 6.7: Use of Ni powder as WE in a Swagelok cell. a) Scheme showing the construction of the Swagelok cell containing Ni powder as WE, and **b)** Scanning electron microscopy image of the $\sim$ 2 μm Ni particles in the TEM grid for observation.

to allow the electron beam to cross it. To circumvent this issue, the passivation layer was grown on top of a metallic powder which is used as working electrode (WE) in the electrochemical experiments. This allowed the study of the edge of the particles, in which the formation of this passivation layer is clearly observed. Ni powder provided the best compromise between particle size and inertness against alloying with Ca. Typically, ~40 mg were placed on the SS plunger of a Swagelok cell (see Figure 6.7a and Section 6.7.3 - Electrochemical methods, page 120) without additional binders or additives. The integrity of the electrode and the electrical contact between the particles were sustained only by the pressure delivered by the spring inside the Swagelok cell.

After electrochemical treatment, the powder was recovered by disassembling the cell inside an Ar-filled glovebox and carefully collecting it with a spatula. The powder was then rinsed several times with dimethyl carbonate (DMC), dispersed and placed over copper TEM grids with plain carbon film (Figure 6.7). The transfer between the argon filled glove box and the TEM was performed without air exposure according to the procedure described by Dupont et al [172]. The microstructural and chemical characterizations of the electrodes were performed using a TECNAI F20-S-Twin operating at 200 kV and equipped with an electron energy loss Spectrometer (EELS) GIF Tridiem in post column.

6.3 X-ray diffraction

X-ray diffraction (XRD) allows the determination of the underlying crystal structure of a material. In general, it enables verification of the crystallinity and structure of a sample with little information of its chemical nature. Fitting XRD patterns allow calculation of the material lattice parameters, the orientation of a crystal (or grain), stress in crystalline regions, and secondary phases in the sample.

In this thesis, the X-ray diffraction of powdered samples (pXRD) allowed the determination of the purity of the different solid materials prepared. When different crystalline phases were present, the weight fraction of each was determined by fitting the obtained powder diffractograms using a Rietveld method implemented in the program FullProf. pXRD patterns were acquired on a Bruker D8 Advance A25 diffractometer in a Debye Scherrer configuration equipped with Mo Kα_1 radiation source (λ = 0.7093 Å) and a Johansson monochromator. Borosilicate glass capillaries with 0.5 mm diameter were used as sample holders and rotated during the data collection.

When crystals of enough size and good quality were obtained, they were selected from the mother liquor under a microscope and quickly transferred to a single-crystal diffractometer, where a flow of cold $N_{2(g)}$ at 150 K protected them from atmospheric H_2O. The single-crystal diffraction (scXRD) data was collected using a Cu Kα radiation source and under the cold nitrogen stream. Data collection and processing was performed with CrysAlisPro software, including an empirical absorption correction using spherical harmonics, implemented in the SCALE3 ABSPACK scaling algorithm, and an analytical numeric absorption correction using a multifaceted crystal model [173]. Crystal structures were solved and refined by full-matrix least-squares minimisation with SHELXL [174] (v. 2018/3) within Olex2 [175] (v. 1.3) software.Unlike pXRD, scXRD allows the absolute determination of atomic positions inside a crystal lattice. Then, scXRD was used in this thesis to confirm the molecular structure of newly synthesised additives, and to determine the crystal packing of the prepared calcium solvate salts.

6.4 Elemental analysis

The elemental analysis essays were performed as a service of the Serveis Cientificotècnics de la Universitat de Barcelona (CCiTUB).

The Ca and B content of the prepared salts were determined by inductively coupled plasma optical emission spectrometry (ICP-OES) in a Perkin Elmer Optima 8300 apparatus, operated under standard conditions. In a typical run, 0.05 g of the powdered sample were digested in a HNO_3 + H_2O_2 mixture at 220 °C in a PTFE reactor heated by a Milestone Ethos One microwave oven. The digested solution was diluted 1/10 with deionized water before the ICP-OES analysis.

The Li, Na, and/or K trace content was determined by inductively coupled plasma mass spectrometry (ICP-MS) in a Perkin Elmer Nexion 350d instrument. The sample was digested as described before, and diluted 1/100 before analysis.

The H and C content was determined by combustion in a EA Flash 200 analyser from Thermo Fisher Scientific following the standard operation conditions. Approximately 1000 µg of the sample were mixed with vanadium and tin pentoxide to promote the complete combustion.

6.5 Thermal analysis methods

Thermogravimetric analysis (TGA) and differential scanning calorimetry (DSC) probe the properties of a material upon heating or cooling. In a TGA measurement, the change in the sample's weight is recorded as the temperature is increased at a constant rate, and under the flow of a suitable gas (either N_2, Ar, or air). If a weight loss is detected, the evolved products can be carried by the flowing gas to a secondary analytic equipment for its identification. TGA was used in this thesis as a probe for thermally activated reactions occurring in the material, such as decomposition or release of solvent molecules from the crystalline structure.

Differential Scanning Calorimetry (DSC) is a technique in which the heat flow into or out of a material is measured as function of temperature or time, while the sample is heated or cooled. In contrast to the TGA essay, it is not restricted to reactions involving a weight loss, so phase transition reactions (as crystallization, melting, etc.) can be detected and their reaction enthalpy measured.

TGA/DSC essays were performed simultaneously in a NETZSCH TGA/STA 449 F5 Jupiter, typically using ∼10 mg of sample in an alumina crucible. The temperature was ramped at either 5 or 10 °C min^{-1} from room temperature to 500 °C with a constant Ar flow of 10 mL min^{-1}. The evolved gases

were analysed by mass spectrometry with electron ionisation (MS-EI) using a quadrupole MS NETZSCH QMS 403 Aëolos Quadro.

6.6 Mass spectrometry

Mass spectrometry (MS) is an analytic technique that aims to identify a compound from the molecular or atomic mass of its constituents. The basic principle of MS is to generate ions from either inorganic or organic compounds by any suitable method, to separate these ions by their mass-to-charge ratio (m/z) and to detect them qualitatively and quantitatively by their respective m/z.

A mass spectrometer consists of *i)* an ion source, which ionize the molecules in the sample by impacting energetic electrons, ions or photons, or by other physical means; *ii)* a mass analyser, which separates the generated ions by means of electric or magnetic fields or combinations of them; and *iii)* a detector which counts the ions previously sorted. There is a large variety of ionization techniques that can be employed, varying in field of application and the results expected [176]. Here, only two examples are presented, to illustrate their basic principle of operation and the difference in the mass spectrum obtained buy each of them.

Electron Ionization (EI) is a hard ionization technique in which a beam of electrons with high kinetic energy (∼70 eV) is shot at the sample in a diluted gas phase. In the collision, if the energy transferred between the electrons and the gas molecules (M) exceeds the ionization energy, a positive radical cation will be generated:

$$\mathrm{M} + \mathrm{e}^- \longrightarrow \mathrm{M}^{+\bullet} + 2\,\mathrm{e}^-$$

This positive radical cation is called the molecular ion, as it has the same molecular weight as the original molecules. In practice, however, as the kinetic energy of the electrons far exceeds the ionization energy of the molecules (ranging around 10-20 eV), the collision will promote bond cleavage and fragmentation of the original molecules. As a result, an EI mass spectrum will show a forest of peaks with different molecular weights depending on the fragments generated. Also, as the EI promotes ejection of electrons from the gas molecules, it produces almost exclusively positively charges ions, although some particular exceptions exist.

Electrospray Ionization (ESI), in contrast, is a soft ionization technique. In

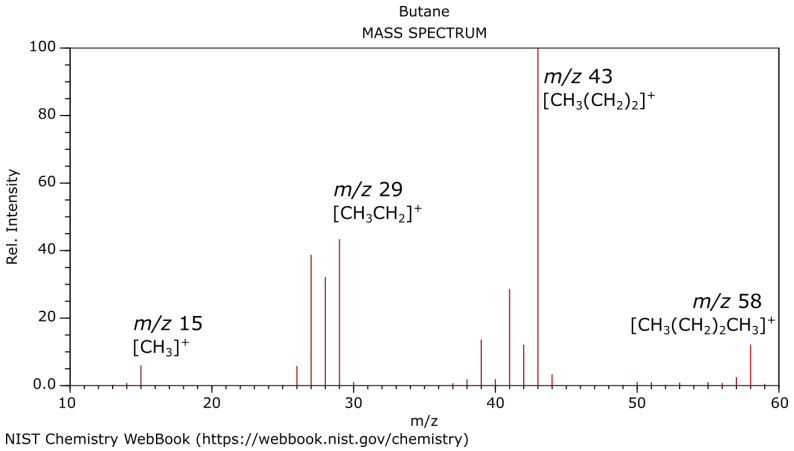

Figure 6.8: Example of a MS spectrum with the assignments of the most relevant peaks. Butane MS-EI obtained from NIST Chemistry WebBook.

ESI, a solution of the analyte in a volatile solvent is injected into a fine capillary under a high-voltage bias. The capillary generates a fine aerosol of electrostatically charged droplets which, after evaporation of the solvent, produce isolated ions that are transferred to the mass analyser and detector. In ESI, little fragmentation is expected and thus the mass spectrum displays in most cases only the molecular ion. This allows the identification of chemical compounds by their molecular weights.

An example of the MS spectrum is shown in Figure 6.8 for butane, generated using EI. The most relevant fragments are labeled, together with their respective assignments. If a ESI mode were used, a single peak at *m/z* 58 would be observed, corresponding with the molecular weight of the molecule. The identification of each peak can be done considering the relative abundance of isotopes of the different elements in the molecule. For example, any ion or ion fragment containing boron shows two contiguous peaks with an 80:20 intensity ratio, given the proportion of ^{10}B:^{11}B in naturally occurring boron.

MS was employed in two instances in this thesis. First, an EI-MS was coupled to the TGA apparatus to analyse the evolved gases during the thermal decomposition of the $Ca(BF_4)_2$ salt, using a quadrupole mass spectrometer NETZSCH QMS 403 Aëolos Quadro. Second, a ESI-MS was employed to detect the presence of boron-containing impurities in a $Ca(BF_4)_2$ solution in EC:PC, or to corroborate the structure of the synthesized $Ca(TFAB)_2$ (see Section 2.4 on Chapter 2). In both case the sample was dissolved/diluted in acetone or THF and then injected into a LC/MSD-TOF equipment from

Agilent Technologies. The capillary was polarized at 4000 V and a flow of 7 L min^{-1} of a drying gas at 325 °C was used.

6.7 Electrochemical methods

6.7.1 Karl-Fisher Coulometric Titration

The Karl Fisher (KF) Coulometric titration allows the fast and reliable determination of water in a liquid or solid sample. It relies in the chemical reaction between iodine and monomethyl sulphide in methanol solution and in the presence of trace amounts of water:

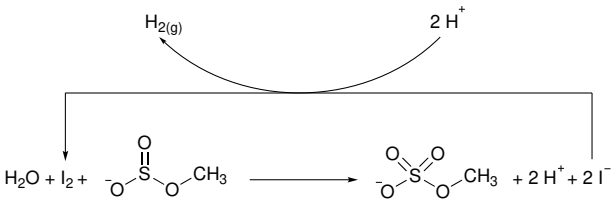

An organic base, typically pyridine or imidazole, is added to the solution to neutralize the generated acids and buffer the pH. In this reaction, I_2 serves as titrant, which is constantly regenerated by oxidation of I^- on the surface of a platinum electrode. The endpoint is detected by an indicator electrode when a small excess of iodine persists in solution. By measuring the total amount of charge required for this process, the amount of water can be calculated.

Given that the water determination relies on an electrochemical reaction, any redox species susceptible to react with iodine or iodide in solution may act as an interference. This is the case of Fe^{III}, Cu^{II}, or ascorbic acid, for example, which will react with I_2 simulating a higher content of water [177]. Another sources of interference are reactions which produce or consume water. For example, boric acid and other boron compounds react with methanol by esterification, releasing water:

$$H_3BO_3 + 3\,CH_3OH \longrightarrow B(OCH_3)_3 + 3\,H_2O$$

In this thesis, the water content of the electrolyte solutions was measured using a Metrohm 899 Karl-Fisher Coulometer, filled with a commercial CombiCoulomat solution by Merck Chemicals. The coulometer is installed inside the glovebox to perform the measurements without exposure of the sample to the atmosphere.

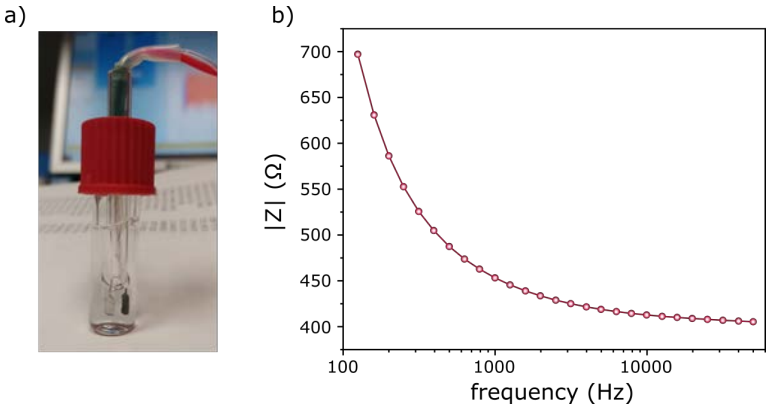

Figure 6.9: Experimental determination of ionic conductivity of a liquid electrolyte. a) conductivity cell employed for the measurements, consisting in two platinum electrodes separated by a fixed distance and immersed in a liquid electrolyte. **b)** Example of the impedance response measured in the cell at different frequencies.

6.7.2 Ionic conductivity determination

Ionic conductivity of solids and liquids can be obtained by measuring the complex impedance response of two parallel electrodes immersed in the solution of interest. A picture of the conductivity cell employed in this thesis is shown in Figure 6.9a. An alternating potential wave was applied between the two parallel platinum electrodes, with frequencies ranging from 50 kHz to 125 Hz, obtaining the impedance modulus response shown in Figure 6.9b.

The ionic conductivity was, then, calculated as the inverse of the impedance limit at high frequency, multiplied by a cell constant: $\sigma = K_{cell} \left(\lim_{f \to \infty} |Z|\right)^{-1}$. The cell constant, in turn, was determined by calibration of the conductivity cell with two conductivity standards provided by Mettler-Toledo. The measurements were performed using a FRA-based Multiplexed Conductivity Meter MCM 10 (BioLogic Science Instruments) from 0 to 120 °C (5 °C steps with 30 min equilibration time).

6.7.3 Conventional electrochemical tests

6.7.3.1 Electrochemical cell

The electrochemical test (cyclic voltammetry, electrochemical impedance spectroscopy, galvanostatic, and potentiostatic tests) were performed in air-tight three-electrode Swagelok cells (Figure 6.10), as described previously [178].

Briefly, a Swagelok cell is composed of three metallic plungers, stainless steel

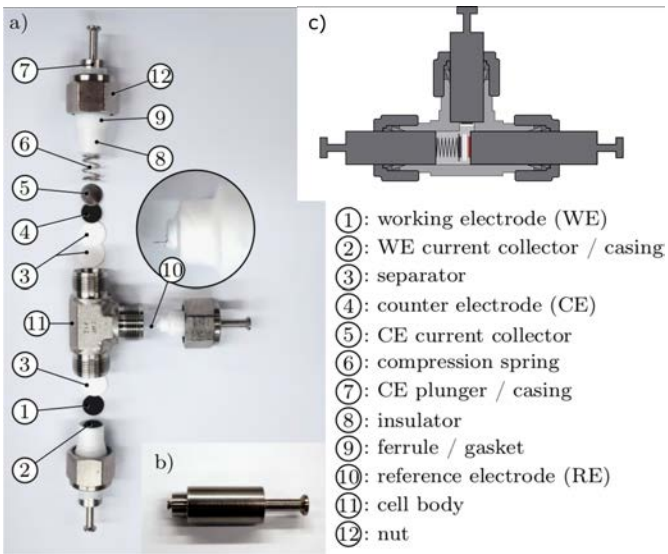

Figure 6.10: Description of the cells for electrochemical experiments a) exploded view of a 3-electrode Swagelok cell; **b)** reference electrode plunger including a groove to attach a metallic wire or mesh; **c)** organization of the electrodes in the closed cell. Figure modified from ref. [178] under the terms of the CC-BY-NC-ND licence.

(SS) 316 is preferred, that act as electrodes/current collectors inside a SS tube union tee of ½ in diameter. Air-tightness is guaranteed by the use of PTFE ferrules in the connection between the tee and the respective nut. As the body of the cell is metallic, the electrodes need to be electrically insulated by covering them with PTFE tape or other similar polymeric film. Several disks of a porous, inert material (glass fibre in our case), soaked in the electrolyte under study, were placed between the working and the counter electrode to act as separators. PTFE showed good resistance to electrolytes based on carbonates, like EC or PC, but can suffer from swelling in ethers or glymes, causing problems with the tightness. Therefore, it is necessary to be careful when choosing the isolating material. Additionally, if any of the electrodes reaches very low potentials, PTFE can decompose forming a black deposit, a problem that was more evidently observed when using glymes as solvents [179].

The assembly of the cells where performed inside an Ar-filled glovebox with H_2O and O_2 contents below 1 ppm. For the assembly of the cells, either a SS, Ni, or Ca disk was placed on top of the metallic rode acting as working electrode (WE); a metal powder can also be used. Two or three glass fibre disks were placed on top and 300-500 μL of electrolyte were added. A Ca disk

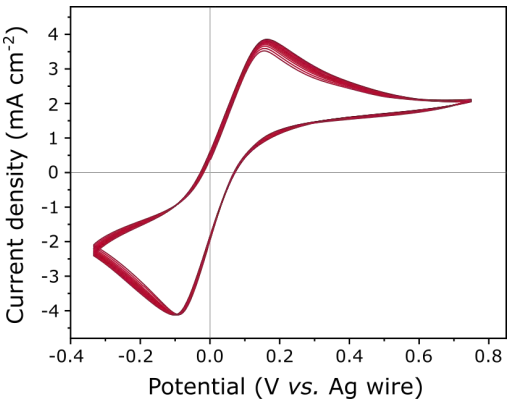

Figure 6.11: Calibration of a Ag QRE using Fc^+/Fc redox couple. CV of a 0.4 M $Ca(TFSI)_2$ electrolyte in EC:PC containing 5 mM Fc over a SS electrode. The potential of the Ag wire was determined as -0.13 V *vs.* Fc^+/Fc, and therefore it is located at +3.1 V *vs.* Ca^{2+}/Ca

was placed on top, followed by a spring which held all the stack together, and the SS plunger.

The reference electrode (RE) presents a significant challenge in such a cell, as the available space is too little to employ a bulky non-aqueous RE. A piece of Ca was used in some experiments, but it resulted in a non-reliable and non-stable potential, as it has been shown before [130]. An alternative miniaturized RE was constructed based on a previous RE miniaturization concept [180]. A piece of Ag wire was attached to a SS plunger with a tailored designed groove. A layer of Ag_2S was then grown on top of the wire by immersing the electrodes in a 5 wt.% $(NH_4)_2S$ solution [181]. In some instances, a neat Ag wire was also used as reference electrode (or quasi-reference electrode). In all cases the potential was calibrated by adding ferrocene (Fc) to the electrolyte and measuring the Fc^+/Fc redox potential against the QRE (Figure 6.11).

6.7.3.2 Testing protocols

The electrochemical stability of the electrolytes was measured by linear sweep voltammetry (LSC) or cyclic voltammetry (CV). In both techniques, the potential of the WE is swept at a constant rate between the initial OCV towards a positive or negative cut-off potential (compared to a static RE). The current is recorded as function of the applied potential, an increase in the recorded current indicates the occurrence of a redox reaction at the WE. By convention, a positive current is associated with an oxidation reaction while a negative

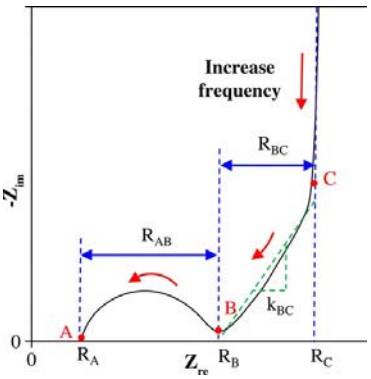

Figure 6.12: Example of a Nyquist plot of EIS measurements in electrochemical systems. Reproduced with permission from Ref. [182]

current is associated to a reduction reaction. In CV, additionally, the potential swept is reversed once the cut-off potential is reached, and the process is continued for several cycles.

To analyse the formation of passivation layers, Swagelok cells using Ni powder, Ni disks or Ca disks as WE were assembled, using Ag wire as RE and Ca metal as CE (see subsection 6.7.3 above). A LSV was performed at 0.1 mV/s from OCV down to -1 V *vs.* Ca^{2+}/Ca, followed by a potentionstatic period of 48h at such potential. During this process a continuous Ca plating occurs, concomitant with some electrolyte decomposition and passivation layer formation. After the 48 h of polarization, a second LSV was performed from -1 V *vs.* Ca^{2+}/Ca at 0.1 mV/s up to the original OCV to remove all the metallic Ca from the Ni substrate, leaving only the passivation layer. The WE was recovered, washed several times with dimethylcarbonate (DMC), let dry naturally and store inside the glovebox until analysis.

Electrochemical impedance spectroscopy (EIS) measures the dielectric properties of a material by the analysis of the response to a small perturbation from its equilibrium point, and provides information about electrode interfaces; structure and reactions taking place, as well as and bulk transport properties. EIS is performed by applying a sinusoidal potential ($V_{(t)}$) of a fixed frequency and small amplitude to the WE, and recording the current response ($I_{(t)}$), from which the complex impedance can be calculated as $Z = V_{(t)} \,/\, I_{(t)} = Z' + iZ''$. Measurements of impedance for varied frequencies gives an electrochemical impedance spectrum, usually presented as a Nyquist plot, in which $-Z''$ is plotted against Z' (Figure 6.12) [182].

A detailed analysis of the impedance response requires the fitting of the experimental data to a suitable model [183]. Qualitatively, however, the arc in

the semicircle (R_{AB} in Figure 6.12) can be related to the total impedance of the (electro)chemical process.

In order for the impedance data to be reliable, it must fulfil the conditions of linearity, causality, and stability [184]. In that sense, Kramers-Kronig (KK) relations can be applied to corroborate that the data does not contain non-linear or non-stable components. As any circuit consisting in passive and distributed elements (*e.g.* resistors and capacitors) satisfy KK relations, it follows that any set of experimental data that can be satisfactorily reproduced by a series of R | C components also satisfies the KK relations [185]. This relation was used here to test the compliance of the obtained EIS data to linearity and stability conditions.

6.8 Viscosity and density determination

The density of solvents and electrolyte solutions was determined using a DMA 4500 density meter from Anton Paar. It is based in a U-shaped glass tube which is filled with the liquid or gas to be analysed. The glass tube is made vibrate by piezo elements into an undammed oscillation frequency, and optical pickups determine the period of oscillation, τ. The density of the sample is calculated by the relation:

$$\rho = C_1\tau^2 - C_2 \tag{6.2}$$

Where C_1 and C_2 are instrument constants that are determined by calibration using at two reference fluids with known densities. The measuring cell can be thermalized with an accuracy of 0.02 °C, and the density can be measured with an uncertainty below 0.0001 g cm^{-3}.

The viscosity was measured using a Lovis 2000 M/ME rolling-ball viscometer from Anton Paar. In this apparatus, the time required for a metal ball to roll from one end of a fluid-filled tube to the other is directly related to the dynamic viscosity of the fluid as:

$$\eta = (\rho_B - \rho)\, gR^2 \sin(\theta)\frac{t}{d} \tag{6.3}$$

Where t is the time for the ball to travel a distance d, θ is the angle of inclination of the filled tube, R is the radius of the ball, and g is the acceleration due to gravity. ρ_B and ρ are the density of the ball and the fluid respectively. Stainless-steel balls with density 7.68 g cm^{-3} and 1.5 mm of diameter were used, together with glass tubes of either 1.59 or 1.8 mm inner diameter. A high ball/tube diameter ratio is preferred to guarantee a laminar flow regime

and a linear relation of Equation 6.3 [186]. Similar to the density case, the measuring tube was thermalized with an accuracy of 0.02 °C, and the obtained viscosity had an uncertainty on less than 0.5%. The density of the solution used in Equation 6.3 was obtained experimentally for each temperature under study.

6.8.1 Viscosity and density model

The VFT model is widely used to describe the transport properties of viscous liquids. It is derived from the classical Arrhenius-model in which the transport (or other property) is controlled by an energetic barrier denoted as activation energy - E_a. In the Arrhenius model this activation energy is assumed to be constant, while in the VFT model it is directly proportional to the temperature. The fitting parameters in the VFT model do not have, a priori, a physical meaning. Some authors have suggested an entropy-related basis, while others decant for the free-volume theory.

In this thesis, the conductivity and viscosity of electrolytes were analysed in the light of the free-volume model, in which the free-volume in a material (solid or liquid) expands linearly as temperature increases. The free-volume fraction, then, governs the conductivity and viscosity of the solution as follows.

The ionic conductivity of an electrolyte is defined as the sum over all the charge species of their concentration multiplied by their mobility and their charge. The mobility of the ion in the electrolyte can be related to diffusion coefficient by the Nerst-Einstein Equation, obtaining:

$$\sigma = \sum_i c_i \, \mu_i \, q_i = \sum_i \frac{c_i \, q_i^2 \, e_0 \, D_i}{k_B \, T} \tag{6.4}$$

In the light of the free-volume model, the diffusion coefficient is related to the free-volume available to allow the movement of the ion, as:

$$D \propto \sqrt{T} \, \exp\left(-\frac{\gamma \, V_f^*}{V_f}\right) \tag{6.5}$$

Where V_f is the fraction of free volume in the electrolyte, while V_f^* is the critical free-volume needed next to a given ion to allow its movement to an adjacent position. The parameter γ is included to account for some overlapping of free-volume spheres around the moving ion. The free volume is assumed to expand linearly with temperature, with a thermal expansion coefficient α:

$$V_f = \alpha \, (T \, - \, T_{0,\sigma} \,) \tag{6.6}$$

Where $T_{0,\sigma}$ is called Vogel temperature, and represents the temperature where the free-volume vanishes. Substituting Equations 6.6 and 6.5 into Equation 6.4 results in:

$$\sigma = \frac{A\,c\,q^2\,e_0}{\sqrt{T}}\,\exp\left(-\frac{E_\sigma}{T\,-\,T_{0,\sigma}}\right);\ \text{where}\ E_\sigma = \frac{\gamma\,V_f^*}{\alpha} \tag{6.7}$$

Rearranging and grouping all constants into a single one, the VFT equation for conductivity is obtained:

$$\text{VFT:}\quad \ln\left(\sigma\,\sqrt{T}\right) = \ln A\,-\,\frac{E_\sigma}{T\,-\,T_{0,\sigma}} \tag{6.8}$$

Following the same argument, The VFT equation for viscosity starting form the Nerst-Einstein equation relating diffusion coefficient and viscosity:

$$D = \frac{k_B\,T}{6\,\pi\,r\,\eta} \tag{6.9}$$

Where r is the radius of the moving species and η is the viscosity of the solution. Rearranging, and including Equations 6.5 and 6.6:

$$\frac{1}{\eta} = \frac{6\,\pi\,r\,\eta}{k_B\,T} = \frac{B}{\sqrt{T}}\,\exp\left(-\frac{\gamma\,V_f^*}{V_f}\right) \tag{6.10}$$

$$\text{VFT:}\quad \ln\left(\frac{\eta}{\sqrt{T}}\right) = -\ln B\,+\,\frac{E_\sigma}{T\,-\,T_{0,\sigma}} \tag{6.11}$$

7

Scientific Output

7.1 Publications

7.1.1 Publications in the scope of this thesis

R. Dugas, J.D. Forero-Saboya, and A. Ponrouch. Methods and Protocols for Reliable Electrochemical Testing in Post-Li Batteries (Na, K, Mg, and Ca). *Chemistry of Materials* 31, 8613-8628 (**2019**).

J.D. Forero-Saboya, E. Marchante, R.B. Araujo, D. Monti, P. Johansson, and A. Ponrouch. Cation Solvation and Physicochemical Properties of Ca Battery Electrolytes. *The Journal of Physical Chemistry C* 123, 29524-29532 (**2019**).

J. Forero-Saboya, C. Davoisne, R. Dedryvère, I. Yousef, P. Canepa, and A. Ponrouch. Understanding the nature of the passivation layer enabling reversible calcium plating. *Energy & Environmental Science* 13, 3423-3431 (**2020**).

J.D. Forero-Saboya, M. Lozinšek, and A. Ponrouch. Towards dry and contaminant free $Ca(BF_4)_2$-based electrolytes for Ca plating. *Journal of Power Sources Advances* 6, 100032 (**2020**).

J. Forero-Saboya, C. Bodin, and A. Ponrouch. A boron-based electrolyte additive for calcium electrodeposition. *Electrochemistry Communications* 124, 106936 (**2021**).

J.D. Forero-Saboya$^{=}$, D.S. Tchitchekova$^{=}$, P. Johansson, M.R. Palacín, and A. Ponrouch. Interfaces and Interphases in Ca and Mg Batteries. *Advanced Materials Interfaces* 2101578 (**2021**).

7.1.2 Publications out of the scope of this thesis

J.D. Forero-Saboya and A. Ponrouch. 5. Testing protocols for Na-ion batteries. In N. Tapia-Ruiz and A.R. Armstrong. 2021 roadmap for sodium-ion batteries. *Journal of Physics: Energy* 3, 031503 (**2021**).

A. Black, C. Frontera, A. Torres, M. Recio-Polo, P. Rozier, J.D. Forero-Saboya, F. Fauth, E. Urones-Garrote, M.E. Arroyo-de Dompablo, and M.R. Palacín. Elucidation of the redox activity of $Ca_2MnO_{3.5}$ and CaV_2O_4 in calcium batteries using operando XRD: charge compensation mechanism and reversibility. *Energy Storage Materials* 2101578 (**2022**).

7.2 Presentations at International Congresses

Poster presentation "Study of SEI Components Enabling Calcium Plating and Stripping" at the 2019 Spring Meeting of the European Materials Research Society (E-MRS). Nice 2019.

Oral presentation "Study of SEI Components Enabling Calcium Plating and Stripping" at The Electrochemical Conference on Energy and the Environment (ECEE) from The Electrochemical Society. Glasgow 2019.

Oral presentation "On the Parameters Affecting Calcium Plating and Stripping from Organic Electrolytes – Cases of Electrolyte Optimization" at the 239th Electrochemical Society Meeting. Online 2021.

Oral presentation "Considerations of $Ca(BF_4)_2$ preparation for calcium battery electrolytes" at the 27th Annual Meeting of the Slovenian Chemical Society. Portorož-Portorose 2021.

Bibliography

(1) *World Energy Transitions Outlook: 1.5°C Pathway, International Renewable Energy*; International Renewable Energy Agency (IRENA), 2021.

(2) Raj, A.; Steingart, D. *Journal of The Electrochemical Society* **2018**, *165*, B3130–B3136, DOI: 10.1149/2.0181808jes.

(3) Schmidt, O.; Melchior, S.; Hawkes, A.; Staffell, I. *Joule* **2019**, *3*, 81–100, DOI: 10.1016/j.joule.2018.12.008.

(4) Muratori, M.; Alexander, M.; Arent, D.; Bazilian, M.; Cazzola, P.; Dede, E. M.; Farrell, J.; Gearhart, C.; Greene, D.; Jenn, A.; Keyser, M.; Lipman, T.; Narumanchi, S.; Pesaran, A.; Sioshansi, R.; Suomalainen, E.; Tal, G.; Walkowicz, K.; Ward, J. *Progress in Energy* **2021**, *3*, 022002, DOI: 10.1088/2516-1083/abe0ad.

(5) Sutherland, B. R. *Joule* **2019**, *3*, 1–3, DOI: 10.1016/j.joule.2018.12.022.

(6) Ziegler, M. S.; Trancik, J. E. *Energy & Environmental Science* **2021**, *14*, 1635–1651, DOI: 10.1039/D0EE02681F.

(7) Xu, K. *Chemical Reviews* **2004**, *104*, 4303–4418, DOI: 10.1021/cr030203g.

(8) An, S. J.; Li, J.; Daniel, C.; Mohanty, D.; Nagpure, S.; Wood, D. L. *Carbon* **2016**, *105*, 52–76, DOI: 10.1016/j.carbon.2016.04.008.

(9) Nie, M.; Chalasani, D.; Abraham, D. P.; Chen, Y.; Bose, A.; Lucht, B. L. *The Journal of Physical Chemistry C* **2013**, *117*, 1257–1267, DOI: 10.1021/jp3118055.

(10) Peled, E.; Menkin, S. *Journal of The Electrochemical Society* **2017**, *164*, A1703–A1719, DOI: 10.1149/2.1441707jes.

(11) Gireaud, L.; Grugeon, S.; Laruelle, S.; Pilard, S.; Tarascon, J.-M. *Journal of The Electrochemical Society* **2005**, *152*, A850, DOI: 10.1149/1.1872673.

(12) Zhuang, G. V.; Xu, K.; Yang, H.; Jow, T. R.; Ross, P. N. *The Journal of Physical Chemistry B* **2005**, *109*, 17567–17573, DOI: 10.1021/jp052474w.

(13) Pinson, M. B.; Bazant, M. Z. *Journal of The Electrochemical Society* **2013**, *160*, A243–A250, DOI: 10.1149/2.044302jes.

(14) Vetter, J.; Novák, P.; Wagner, M.; Veit, C.; Möller, K.-C.; Besenhard, J.; Winter, M.; Wohlfahrt-Mehrens, M.; Vogler, C.; Hammouche, A. *Journal of Power Sources* **2005**, *147*, 269–281, DOI: 10.1016/j.jpowsour.2005.01.006.

(15) Heiskanen, S. K.; Kim, J.; Lucht, B. L. *Joule* **2019**, *3*, 2322–2333, DOI: 10.1016/j.joule.2019.08.018.

(16) Michan, A. L.; Parimalam, B. S.; Leskes, M.; Kerber, R. N.; Yoon, T.; Grey, C. P.; Lucht, B. L. *Chemistry of Materials* **2016**, *28*, 8149–8159, DOI: 10.1021/acs.chemmater.6b02282.

(17) Nie, M.; Demeaux, J.; Young, B. T.; Heskett, D. R.; Chen, Y.; Bose, A.; Woicik, J. C.; Lucht, B. L. *Journal of The Electrochemical Society* **2015**, *162*, A7008–A7014, DOI: 10.1149/2.0021513jes.

(18) He, M.; Guo, R.; Hobold, G. M.; Gao, H.; Gallant, B. M. *Proceedings of the National Academy of Sciences* **2020**, *117*, 73–79, DOI: 10.1073/pnas.1911017116.

(19) Obrovac, M. N.; Christensen, L. *Electrochemical and Solid-State Letters* **2004**, *7*, A93, DOI: 10.1149/1.1652421.

(20) Zhang, W.-J. *Journal of Power Sources* **2011**, *196*, 13–24, DOI: 10.1016/j.jpowsour.2010.07.020.

(21) Cheng, X.-B.; Zhang, R.; Zhao, C.-Z.; Zhang, Q. *Chemical Reviews* **2017**, *117*, 10403–10473, DOI: 10.1021/acs.chemrev.7b00115.

(22) Porz, L.; Swamy, T.; Sheldon, B. W.; Rettenwander, D.; Frömling, T.; Thaman, H. L.; Berendts, S.; Uecker, R.; Carter, W. C.; Chiang, Y.-M. *Advanced Energy Materials* **2017**, *7*, 1701003, DOI: 10.1002/aenm.201701003.

(23) Bai, P.; Li, J.; Brushett, F. R.; Bazant, M. Z. *Energy & Environmental Science* **2016**, *9*, 3221–3229, DOI: 10.1039/C6EE01674J.

(24) Greenwood, N. N.; Earnshaw, A., *Chemistry of the Elements*; Elsevier: 1997, DOI: 10.1016/C2009-0-30414-6.

(25) Aurbach, D.; Lu, Z.; Schechter, A.; Gofer, Y.; Gizbar, H.; Turgeman, R.; Cohen, Y.; Moshkovich, M.; Levi, E. *Nature* **2000**, *407*, 724–727, DOI: 10.1038/35037553.

(26) Lipson, A. L.; Han, S.-D.; Pan, B.; See, K. A.; Gewirth, A. A.; Liao, C.; Vaughey, J. T.; Ingram, B. J. *Journal of The Electrochemical Society* **2016**, *163*, A2253–A2257, DOI: 10.1149/2.0451610jes.

(27) Yoo, H. D.; Shterenberg, I.; Gofer, Y.; Gershinsky, G.; Pour, N.; Aurbach, D. *Energy & Environmental Science* **2013**, *6*, 2265, DOI: 10.1039/c3ee40871j.

(28) Monti, D.; Ponrouch, A.; Araujo, R. B.; Barde, F.; Johansson, P.; Palacín, M. R. *Frontiers in Chemistry* **2019**, *7*, 79, DOI: 10.3389/fchem.2019.00079.

(29) Dompablo, M. E. A.-d.; Ponrouch, A.; Johansson, P.; Palacín, M. R. *Chemical Reviews* **2020**, *120*, 6331–6357, DOI: 10.1021/acs.chemrev.9b00339.

(30) Palacin, M. *ECS Meeting Abstracts* **2020**, *MA2020-02*, 19–19, DOI: 10.1149/MA2020-02119mtgabs.

(31) Iton, Z. W. B.; See, K. A. *Chemistry of Materials* **2022**, *34*, 881–898, DOI: 10.1021/acs.chemmater.1c04178.

(32) Canepa, P.; Gautam, G. S.; Hannah, D. C.; Malik, R.; Liu, M.; Gallagher, K. G.; Persson, K. A.; Ceder, G. *Chemical Reviews* **2017**, *117*, 4287–4341, DOI: 10.1021/acs.chemrev.6b00614.

(33) Torres, A.; Casals, J. L.; Dompablo, M. E. A.-d. *Chemistry of Materials* **2021**, *33*, 2488–2497, DOI: 10.1021/acs.chemmater.0c04741.

(34) Verrelli, R.; Black, A.; Dugas, R.; Tchitchekova, D.; Ponrouch, A.; Palacin, M. R. *Journal of The Electrochemical Society* **2020**, *167*, 070532, DOI: 10.1149/1945-7111/ab7a82.

(35) Palacin, M.; Black, A.; Tchitchekova, D. S.; Johansson, P.; Araujo, R. B.; Aren, F.; Dompablo, E. A.-d.; Torres, A.; Tortajada, J.; Luque, J.; Wuersig, A.; Bremes, H. G. *ECS Meeting Abstracts* **2020**, *MA2020-02*, 449–449, DOI: 10.1149/MA2020-022449mtgabs.

(36) Shannon, R. D. *Acta Crystallographica Section A* **1976**, *32*, 751–767, DOI: 10.1107/S0567739476001551.

(37) Poizot, P.; Gaubicher, J.; Renault, S.; Dubois, L.; Liang, Y.; Yao, Y. *Chemical Reviews* **2020**, *120*, 6490–6557, DOI: 10.1021/acs.chemrev.9b00482.

(38) Sano, H.; Senoh, H.; Yao, M.; Sakaebe, H.; Kiyobayashi, T. *Chemistry Letters* **2012**, *41*, 1594–1596, DOI: 10.1246/cl.2012.1594.

(39) Dong, H.; Tutusaus, O.; Liang, Y.; Zhang, Y.; Lebens-Higgins, Z.; Yang, W.; Mohtadi, R.; Yao, Y. *Nature Energy* **2020**, *5*, 1043–1050, DOI: 10.1038/s41560-020-00734-0.

(40) Gaddum, L. W.; French, H. E. *Journal of the American Chemical Society* **1927**, *49*, 1295–1299, DOI: 10.1021/ja01404a020.

(41) Muldoon, J.; Bucur, C. B.; Gregory, T. *Chemical Reviews* **2014**, *114*, 11683–11720, DOI: 10.1021/cr500049y.

(42) Gizbar, H.; Vestfrid, Y.; Chusid, O.; Gofer, Y.; Gottlieb, H. E.; Marks, V.; Aurbach, D. *Organometallics* **2004**, *23*, 3826–3831, DOI: 10.1021/om049949a.

(43) Vestfried, Y.; Chusid, O.; Goffer, Y.; Aped, P.; Aurbach, D. *Organometallics* **2007**, *26*, 3130–3137, DOI: 10.1021/om061076s.

(44) See, K. A.; Chapman, K. W.; Zhu, L.; Wiaderek, K. M.; Borkiewicz, O. J.; Barile, C. J.; Chupas, P. J.; Gewirth, A. A. *Journal of the American Chemical Society* **2016**, *138*, 328–337, DOI: 10.1021/jacs.5b10987.

(45) Mizuno, F.; Singh, N.; Arthur, T. S.; Fanson, P. T.; Ramanathan, M.; Benmayza, A.; Prakash, J.; Liu, Y. S.; Glans, P. A.; Guo, J. *Frontiers in Energy Research* **2014**, *2*, 46, DOI: 10.3389/fenrg.2014.00046.

(46) Ta, K.; See, K. A.; Gewirth, A. A. *The Journal of Physical Chemistry C* **2018**, *122*, 13790–13796, DOI: 10.1021/acs.jpcc.8b00835.

(47) Attias, R.; Dlugatch, B.; Chae, M. S.; Goffer, Y.; Aurbach, D. *Electrochemistry Communications* **2021**, *124*, 106952, DOI: 10.1016/j.elecom.2021.106952.

(48) Canepa, P.; Gautam, G. S.; Malik, R.; Jayaraman, S.; Rong, Z.; Zavadil, K. R.; Persson, K.; Ceder, G. *Chemistry of Materials* **2015**, *27*, 3317–3325, DOI: 10.1021/acs.chemmater.5b00389.

(49) Drews, J.; Jankowski, P.; Häcker, J.; Li, Z.; Danner, T.; Lastra, J. M. G.; Vegge, T.; Wagner, N.; Friedrich, K. A.; Zhao-Karger, Z.; Fichtner, M.; Latz, A. *ChemSusChem* **2021**, *14*, 4820–4835, DOI: 10.1002/cssc.202101498.

(50) Hahn, N. T.; Self, J.; Han, K. S.; Murugesan, V.; Mueller, K. T.; Persson, K. A.; Zavadil, K. R. *The Journal of Physical Chemistry B* **2021**, *125*, 3644–3652, DOI: 10.1021/acs.jpcb.1c00263.

(51) Arthur, T. S.; Glans, P.-A.; Singh, N.; Tutusaus, O.; Nie, K.; Liu, Y.-S.; Mizuno, F.; Guo, J.; Alsem, D. H.; Salmon, N. J.; Mohtadi, R. *Chemistry of Materials* **2017**, *29*, 7183–7188, DOI: 10.1021/acs.chemmater.7b01189.

(52) Rajput, N. N.; Qu, X.; Sa, N.; Burrell, A. K.; Persson, K. A. *Journal of the American Chemical Society* **2015**, *137*, 3411–3420, DOI: 10.1021/jacs.5b01004.

(53) Tutusaus, O.; Mohtadi, R.; Arthur, T. S.; Mizuno, F.; Nelson, E. G.; Sevryugina, Y. V. *Angewandte Chemie International Edition* **2015**, *54*, 7900–7904, DOI: 10.1002/anie.201412202.

(54) Jay, R.; Tomich, A. W.; Zhang, J.; Zhao, Y.; Gorostiza, A. D.; Lavallo, V.; Guo, J. *ACS Applied Materials and Interfaces* **2019**, *11*, 11414–11420, DOI: 10.1021/acsami.9b00037.

(55) Tutusaus, O.; Mohtadi, R.; Singh, N.; Arthur, T. S.; Mizuno, F. *ACS Energy Letters* **2017**, *2*, 224–229, DOI: 10.1021/acsenergylett.6b00549.

(56) Shterenberg, I.; Salama, M.; Yoo, H. D.; Gofer, Y.; Park, J.-B.; Sun, Y.-K.; Aurbach, D. *Journal of The Electrochemical Society* **2015**, *162*, A7118–A7128, DOI: 10.1149/2.0161513jes.

(57) Wang, H.; Feng, X.; Chen, Y.; Liu, Y. S.; Han, K. S.; Zhou, M.; Engelhard, M. H.; Murugesan, V.; Assary, R. S.; Liu, T. L.; Henderson, W.; Nie, Z.; Gu, M.; Xiao, J.; Wang, C.; Persson, K.; Mei, D.; Zhang, J. G.; Mueller, K. T.; Guo, J.; Zavadil, K.; Shao, Y.; Liu, J. *ACS Energy Letters* **2020**, *5*, 200–206, DOI: 10.1021/acsenergylett.9b02211.

(58) Zhao-Karger, Z.; Bardaji, M. E. G.; Fuhr, O.; Fichtner, M. *Journal of Materials Chemistry A* **2017**, *5*, 10815–10820, DOI: 10.1039/C7TA02237A.

(59) Tang, K.; Du, A.; Dong, S.; Cui, Z.; Liu, X.; Lu, C.; Zhao, J.; Zhou, X.; Cui, G. *Advanced Materials* **2020**, *32*, 1–7, DOI: 10.1002/adma.201904987.

(60) Jankowski, P.; Li, Z.; Zhao-Karger, Z.; Diemant, T.; Fichtner, M.; Vegge, T.; Lastra, J. M. G. *Energy Storage Materials* **2022**, *45*, 1133–1143, DOI: 10.1016/j.ensm.2021.11.012.

(61) Aurbach, D.; Skaletsky, R.; Gofer, Y. *Journal of The Electrochemical Society* **1991**, *138*, 3536–3545, DOI: 10.1149/1.2085455.

(62) Ponrouch, A.; Frontera, C.; Bardé, F.; Palacín, M. R. *Nature Materials* **2016**, *15*, 169–172, DOI: 10.1038/nmat4462.

(63) Wang, D.; Gao, X.; Chen, Y.; Jin, L.; Kuss, C.; Bruce, P. G. *Nature Materials* **2018**, *17*, 16–20, DOI: 10.1038/nmat5036.

(64) Pu, S. D.; Gong, C.; Gao, X.; Ning, Z.; Yang, S.; Marie, J.-J.; Liu, B.; House, R. A.; Hartley, G. O.; Luo, J.; Bruce, P. G.; Robertson, A. W. *ACS Energy Letters* **2020**, *5*, 2283–2290, DOI: 10.1021/acsenergylett.0c01153.

(65) Kisu, K.; Kim, S.; Shinohara, T.; Zhao, K.; Züttel, A.; Orimo, S.-i. *Scientific Reports* **2021**, *11*, 7563, DOI: 10.1038/s41598-021-86938-0.

(66) Li, Z.; Fuhr, O.; Fichtner, M.; Zhao-Karger, Z. *Energy & Environmental Science* **2019**, *12*, 3496–3501, DOI: 10.1039/C9EE01699F.

(67) Shyamsunder, A.; Blanc, L. E.; Assoud, A.; Nazar, L. F. *ACS Energy Letters* **2019**, *4*, 2271–2276, DOI: 10.1021/acsenergylett.9b01550.

(68) Hahn, N. T.; Driscoll, D. M.; Yu, Z.; Sterbinsky, G. E.; Cheng, L.; Balasubramanian, M.; Zavadil, K. R. *ACS Applied Energy Materials* **2020**, *3*, 8437–8447, DOI: 10.1021/acsaem.0c01070.

(69) Melemed, A. M.; Skiba, D. A.; Gallant, B. M. *The Journal of Physical Chemistry C* **2022**, *126*, 892–902, DOI: 10.1021/acs.jpcc.1c09400.

(70) Hou, S.; Ji, X.; Gaskell, K.; Wang, P.-f.; Wang, L.; Xu, J.; Sun, R.; Borodin, O.; Wang, C. *Science* **2021**, *374*, 172–178, DOI: 10.1126/science.abg3954.

(71) Sock, O.; Lemoine, P.; Gross, M. *Electrochimica Acta* **1980**, *25*, 1025–1026, DOI: 10.1016/0013-4686(80)87009-5.

(72) Herlem, G.; Reybier, K.; Trokourey, A.; Fahys, B. *Journal of The Electrochemical Society* **2000**, *147*, 597, DOI: 10.1149/1.1393239.

(73) Ponrouch, A.; Palacin, M. *Current Opinion in Electrochemistry* **2018**, *9*, 1–7, DOI: 10.1016/j.coelec.2018.02.001.

(74) Jordan, T. H.; Dickens, B.; Schroeder, L. W.; Brown, W. E. *Acta Crystallographica Section B Structural Crystallography and Crystal Chemistry* **1975**, *31*, 669–672, DOI: 10.1107/S0567740875003597.

(75) Zachara, J.; Wišniewski, W. *Journal of Thermal Analysis* **1995**, *44*, 929–935, DOI: 10.1007/BF02547276.

(76) Itakura, T.; Sasai, R.; Itoh, H. *Bulletin of the Chemical Society of Japan* **2006**, *79*, 1303–1307, DOI: 10.1246/bcsj.79.1303.

(77) Korenowski, T. F.; Penland, J. L.; Ritzert, C. J. Waste Treatment of Fluoroborate Solutions, US4008162A, 1977.

(78) Wagman, D. D.; Evans, W. H.; Parker, V. B.; Schumm, R. H.; Halow, I.; Bailey, S. M.; Churney, K. L.; Nuttall, R. L. *Journal of Physical and Chemical Reference Data* **1982**, *11*, Suppl. No.2.

(79) Pape, R. D.; Ravez, J. *Comptes Rendus Hebdomadaires des Séances de l'Académie des Sciences* **1962**, *24*, 4171–4173.

(80) Brown, H. C.; Adams, R. M. *Journal of the American Chemical Society* **1942**, *64*, 2557–2563, DOI: 10.1021/ja01263a009.

(81) Bernhardt, E.; Berkei, M.; Willner, H.; Schürmann, M. *Zeitschrift für anorganische und allgemeine Chemie* **2003**, *629*, 677–685, DOI: 10.1002/zaac.200390115.

(82) Bernal, I.; Cetrullo, J.; Cai, J.; Geanangel, R. A.; Worrell, J. H. *Journal of the Chemical Society, Dalton Transactions* **1995**, 99–104, DOI: 10.1039/DT9950000099.

(83) Heimer, N. E.; Sesto, R. E. D.; Meng, Z.; Wilkes, J. S.; Carper, W. R. *Journal of Molecular Liquids* **2006**, *124*, 84–95, DOI: 10.1016/j.molliq.2005.08.004.

(84) Lipson, A. L.; Pan, B.; Lapidus, S. H.; Liao, C.; Vaughey, J. T.; Ingram, B. J. *Chemistry of Materials* **2015**, *27*, 8442–8447, DOI: 10.1021/acs.chemmater.5b04027.

(85) Keyzer, E. N.; Matthews, P. D.; Liu, Z.; Bond, A. D.; Grey, C. P.; Wright, D. S. *Chemical Communications* **2017**, *53*, 4573–4576, DOI: 10.1039/C7CC01938F.

(86) Haiges, R.; Christe, K. O. *Zeitschrift für anorganische und allgemeine Chemie* **2002**, *628*, 1717, DOI: 10.1002/1521-3749(200208)628:8<1717::AID-ZAAC1717>3.0.CO;2-C.

(87) Zinigrad, E.; Larush-Asraf, L.; Salitra, G.; Sprecher, M.; Aurbach, D. *Thermochimica Acta* **2007**, *457*, 64–69, DOI: 10.1016/j.tca.2007.03.001.

(88) Ramírez, A.; Lobkovsky, E.; Collum, D. B. *Journal of the American Chemical Society* **2003**, *125*, 15376–15387, DOI: 10.1021/ja030322d.

(89) Seo, D. M.; Boyle, P. D.; Allen, J. L.; Han, S.-D.; Jónsson, E.; Johansson, P.; Henderson, W. A. *The Journal of Physical Chemistry C* **2014**, *118*, 18377–18386, DOI: 10.1021/jp5046782.

(90) Weiss, A.; Zohner, K. *physica status solidi (b)* **1967**, *21*, 257–270, DOI: 10.1002/pssb.19670210125.

(91) Brunton, G. *Acta Crystallographica Section B Structural Crystallography and Crystal Chemistry* **1969**, *25*, 2161–2162, DOI: 10.1107/S0567740869005309.

(92) Hoard, J. L.; Blair, V. *Journal of the American Chemical Society* **1935**, *57*, 1985–1988, DOI: 10.1021/ja01313a067.

(93) Tiritiris, I.; Müller-Bunz, H.; Schleid, T. *Zeitschrift für anorganische und allgemeine Chemie* **2002**, *628*, 2212–2212, DOI: 10.1002/1521-3749(200209)628:9/10<2212::AID-ZAAC11112212>3.0.CO;2-6.

(94) Zavalij, P. Y.; Yang, S.; Whittingham, M. S. *Acta Crystallographica Section B Structural Science* **2004**, *60*, 716–724, DOI: 10.1107/S0108768104022153.

(95) Fukushima, K.; Chibahara, H. *Journal of Molecular Structure* **1993**, *291*, 145–150, DOI: 10.1016/0022-2860(93)85038-V.

(96) Nissinen, V. H.; Koshevoy, I. O.; Pakkanen, T. T. *Dalton Transactions* **2017**, *46*, 4452–4460, DOI: 10.1039/C7DT00193B.

(97) Harriss, M. G.; Milne, J. B. *Canadian Journal of Chemistry* **1971**, *49*, 3612–3616, DOI: 10.1139/v71-604.

(98) Yamaguchi, H.; Takahashi, H.; Kato, M.; Arai, J. *Journal of The Electrochemical Society* **2003**, *150*, A312, DOI: 10.1149/1.1545454.

(99) Christe, K. O.; Naumann, D. *Spectrochimica Acta Part A: Molecular Spectroscopy* **1973**, *29*, 2017–2024, DOI: 10.1016/0584-8539(73)80060-1.

(100) Redington, R. L. *Spectrochimica Acta Part A: Molecular Spectroscopy* **1975**, *31*, 1699–1705, DOI: 10.1016/0584-8539(75)80112-7.

(101) Walden, P. *Zeitschrift für Physikalische Chemie* **1906**, *55U*, 207–249, DOI: 10.1515/zpch-1906-5511.

(102) Chen, F.; Yang, Z.; Chen, Z.; Hu, J.; Chen, C.; Cai, J. *Journal of Molecular Liquids* **2015**, *209*, 683–692, DOI: 10.1016/j.molliq.2015.06.041.

(103) Allam, D. S.; Lee, W. H. *Journal of the Chemical Society A: Inorganic, Physical, Theoretical* **1966**, 5, DOI: 10.1039/j19660000005.

(104) Souquet, J.; Perera, W. *Solid State Ionics* **1990**, *40-41*, 595–604, DOI: 10.1016/0167-2738(90)90078-6.

(105) Cohen, M. H.; Turnbull, D. *The Journal of Chemical Physics* **1959**, *31*, 1164–1169, DOI: 10.1063/1.1730566.

(106) Forero-Saboya, J. D.; Marchante, E.; Araujo, R. B.; Monti, D.; Johansson, P.; Ponrouch, A. *Journal of Physical Chemistry C* **2019**, *123*, 29524–29532, DOI: 10.1021/acs.jpcc.9b07308.

(107) Barthel, J.; Gerber, R.; Gores, H.-J. *Berichte der Bunsengesellschaft für physikalische Chemie* **1984**, *88*, 616–622, DOI: 10.1002/bbpc.19840880709.

(108) Nilsson, V.; Bernin, D.; Brandell, D.; Edström, K.; Johansson, P. *ChemPhysChem* **2020**, *21*, 1166–1176, DOI: 10.1002/cphc.202000153.

(109) Chen, Y.; Jaegers, N. R.; Wang, H.; Han, K. S.; Hu, J. Z.; Mueller, K. T.; Murugesan, V. *The Journal of Physical Chemistry Letters* **2020**, *11*, 6443–6449, DOI: 10.1021/acs.jpclett.0c01447.

(110) Salama, M.; Shterenberg, I.; Gizbar, H.; Eliaz, N. N.; Kosa, M.; Keinan-Adamsky, K.; Afri, M.; Shimon, L. J. W.; Gottlieb, H. E.; Major, D. T.; Gofer, Y.; Aurbach, D. *The Journal of Physical Chemistry C* **2016**, *120*, 19586–19594, DOI: 10.1021/acs.jpcc.6b07733.

(111) Hahn, N. T.; Driscoll, D. M.; Yu, Z.; Sterbinsky, G. E.; Cheng, L.; Balasubramanian, M.; Zavadil, K. R. *ACS Applied Energy Materials* **2020**, *3*, 8437–8447, DOI: 10.1021/acsaem.0c01070.

(112) Han, K. S.; Hahn, N. T.; Zavadil, K. R.; Jaegers, N. R.; Chen, Y.; Hu, J. Z.; Murugesan, V.; Mueller, K. T. *The Journal of Physical Chemistry C* **2021**, *125*, 6005–6012, DOI: 10.1021/acs.jpcc.0c09830.

(113) Barthel, J.; Gores, H. J.; Schmeer, G. *Berichte der Bunsengesellschaft für physikalische Chemie* **1979**, *83*, 911–920, DOI: 10.1002/bbpc.19790830908.

(114) Logan, E. R.; Tonita, E. M.; Gering, K. L.; Li, J.; Ma, X.; Beaulieu, L. Y.; Dahn, J. R. *Journal of The Electrochemical Society* **2018**, *165*, A21–A30, DOI: 10.1149/2.0271802jes.

(115) Lee, S.-Y.; Ueno, K.; Angell, C. A. *The Journal of Physical Chemistry C* **2012**, *116*, 23915–23920, DOI: 10.1021/jp3067519.

(116) Schreiner, C.; Zugmann, S.; Hartl, R.; Gores, H. J. *Journal of Chemical & Engineering Data* **2010**, *55*, 1784–1788, DOI: 10.1021/je900878j.

(117) Seo, D. M.; Reininger, S.; Kutcher, M.; Redmond, K.; Euler, W. B.; Lucht, B. L. *The Journal of Physical Chemistry C* **2015**, *119*, 14038–14046, DOI: 10.1021/acs.jpcc.5b03694.

(118) Schreiner, C.; Zugmann, S.; Hartl, R.; Gores, H. J. *Journal of Chemical & Engineering Data* **2010**, *55*, 4372–4377, DOI: 10.1021/je1005505.

(119) Xu, W.; Cooper, E. I.; Angell, C. A. *The Journal of Physical Chemistry B* **2003**, *107*, 6170–6178, DOI: 10.1021/jp0275894.

(120) MacFarlane, D. R.; Forsyth, M.; Izgorodina, E. I.; Abbott, A. P.; Annat, G.; Fraser, K. *Physical Chemistry Chemical Physics* **2009**, *11*, 4962, DOI: 10.1039/b900201d.

(121) Noda, A.; Hayamizu, K.; Watanabe, M. *The Journal of Physical Chemistry B* **2001**, *105*, 4603–4610, DOI: 10.1021/jp004132q.

(122) Xu, W.; Angell, C. A. *Electrochemical and Solid-State Letters* **2001**, *4*, E1, DOI: 10.1149/1.1344281.

(123) Schindler, W.; Zerda, T. W.; Jonas, J. *The Journal of Chemical Physics* **1984**, *81*, 4306–4313, DOI: 10.1063/1.447440.

(124) Al-Jallo, H. N.; Al-Azawi, F. N. *Spectrochimica Acta Part A: Molecular Spectroscopy* **1978**, *34*, 819–823, DOI: 10.1016/0584-8539(78)80036-1.

(125) Angell, C. L. *Transactions of the Faraday Society* **1956**, *52*, 1178–1183, DOI: 10.1039/tf9565201178.

(126) Jankowski, P.; Grzegorzewska, K.; Szabłowska, A.; Piszcz, M.; Dranka, M.; Żukowska, G.; Kalita, M. *Electrochimica Acta* **2015**, *175*, 240–246, DOI: 10.1016/j.electacta.2015.03.028.

(127) Duluard, S.; Grondin, J.; Bruneel, J.-L.; Pianet, I.; Grélard, A.; Campet, G.; Delville, M.-H.; Lassègues, J.-C. *Journal of Raman Spectroscopy* **2008**, *39*, 627–632, DOI: 10.1002/jrs.1896.

(128) Lassègues, J.-C.; Grondin, J.; Aupetit, C.; Johansson, P. *The Journal of Physical Chemistry A* **2009**, *113*, 305–314, DOI: 10.1021/jp806124w.

(129) Laurence, C.; Gal, J.-F., *Lewis Basicity and Affinity Scales*; John Wiley & Sons, Ltd: 2009, DOI: 10.1002/9780470681909.

(130) Tchitchekova, D. S.; Monti, D.; Johansson, P.; Bardé, F.; Randon-Vitanova, A.; Palacín, M. R.; Ponrouch, A. *Journal of The Electrochemical Society* **2017**, *164*, A1384–A1392, DOI: 10.1149/2.0411707jes.

(131) Melemed, A. M.; Gallant, B. M. *Journal of The Electrochemical Society* **2020**, *167*, 140543, DOI: 10.1149/1945-7111/abc725.

(132) Wang, Z.; Li, Z.; Huang, J.; Zhang, J. *ECS Transactions* **2017**, *75*, 151–164, DOI: 10.1149/07520.0151ecst.

(133) Abe, T.; Fukuda, H.; Iriyama, Y.; Ogumi, Z. *Journal of The Electrochemical Society* **2004**, *151*, A1120, DOI: 10.1149/1.1763141.

(134) Ishihara, Y.; Miyazaki, K.; Fukutsuka, T.; Abe, T. *ECS Electrochemistry Letters* **2014**, *3*, A83–A86, DOI: 10.1149/2.0011408eel.

(135) Moškon, J.; Žuntar, J.; Talian, S. D.; Dominko, R.; Gaberšček, M. *Journal of The Electrochemical Society* **2020**, *167*, 140539, DOI: 10.1149/1945-7111/abc769.

(136) Bitenc, J.; Scafuri, A.; Pirnat, K.; Lozinšek, M.; Jerman, I.; Grdadolnik, J.; Fraisse, B.; Berthelot, R.; Stievano, L.; Dominko, R. *Batteries & Supercaps* **2021**, *4*, 214–220, DOI: 10.1002/batt.202000197.

(137) Cazaux, J. *Journal of Electron Spectroscopy and Related Phenomena* **2000**, *113*, 15–33, DOI: 10.1016/S0368-2048(00)00190-0.

(138) Stipp, S. L.; Hochella, M. F. *Geochimica et Cosmochimica Acta* **1991**, *55*, 1723–1736, DOI: 10.1016/0016-7037(91)90142-R.

(139) Järvinen, L.; Leiro, J.; Heinonen, M. *Surface and Interface Analysis* **2014**, *46*, 399–406, DOI: 10.1002/sia.5511.

(140) Hendrickson, D. N.; Hollander, J. M.; Jolly, W. L. *Inorganic Chemistry* **1970**, *9*, 612–615, DOI: 10.1021/ic50085a035.

(141) Freire, M. G.; Neves, C. M. S. S.; Marrucho, I. M.; Coutinho, J. A. P.; Fernandes, A. M. *The Journal of Physical Chemistry A* **2010**, *114*, 3744–3749, DOI: 10.1021/jp903292n.

(142) Forero-Saboya, J.; Davoisne, C.; Dedryvère, R.; Yousef, I.; Canepa, P.; Ponrouch, A. *Energy & Environmental Science* **2020**, *13*, 3423–3431, DOI: 10.1039/D0EE02347G.

(143) Fortunato, B.; Mirone, P.; Fini, G. *Spectrochimica Acta Part A: Molecular Spectroscopy* **1971**, *27*, 1917–1927, DOI: 10.1016/0584-8539(71)80245-3.

(144) Janz, G.; Ambrose, J.; Coutts, J.; Downey, J. *Spectrochimica Acta Part A: Molecular Spectroscopy* **1979**, *35*, 175–179, DOI: 10.1016/0584-8539(79)80181-6.

(145) Weir, C.; Schroeder, R. *Journal of Research of the National Bureau of Standards Section A: Physics and Chemistry* **1964**, *68A*, 465, DOI: 10.6028/jres.068A.045.

(146) Schwarz, W.; Mensching, L.; Hallmeier, K.; Szargan, R. *Chemical Physics* **1983**, *82*, 57–65, DOI: 10.1016/0301-0104(83)85347-6.

(147) Garvie, L. A. J.; Craven, A. J.; Brydson, R. *American Mineralogist* **1995**, *80*, 1132–1144, DOI: 10.2138/am-1995-11-1204.

(148) Sauer, H.; Brydson, R.; Rowley, P.; Engel, W.; Thomas, J. *Ultramicroscopy* **1993**, *49*, 198–209, DOI: 10.1016/0304-3991(93)90226-N.

(149) Yamijala, S. S. R. K. C.; Kwon, H.; Guo, J.; Wong, B. M. *ACS Applied Materials & Interfaces* **2021**, *13*, 13114–13122, DOI: 10.1021/acsami.0c21716.

(150) Young, J.; Smeu, M. *The Journal of Physical Chemistry Letters* **2018**, *9*, 3295–3300, DOI: 10.1021/acs.jpclett.8b01261.

(151) Jankowski, P.; Wieczorek, W.; Johansson, P. *Journal of Molecular Modeling* **2017**, *23*, 6, DOI: 10.1007/s00894-016-3180-0.

(152) Eisele, L.; Laszczynski, N.; Schneider, M.; Lucht, B.; Krossing, I. *Journal of The Electrochemical Society* **2020**, *167*, 060514, DOI: 10.1149/1945-7111/ab80ad.

(153) Nishida, T.; Kon, S. Electrtolyte Solution for Lithium Secondary Battery and Lithium Secondary Battery pat., JP2009021183A, 2009.

(154) Wang, Y.; Zhang, M.; Sacken, U. V.; Way, B. M. Boron trifluoride as an electrolyte additive for improving cycle life of non-aqueous rechargeable lithium batteries European pat., 0903798A1, 1999.

(155) Brown, C. J. *Acta Crystallographica* **1954**, *7*, 92–96, DOI: 10.1107/S0365110X54000175.

(156) Begun, G. M.; Palko, A. A. *The Journal of Chemical Physics* **1963**, *38*, 2112–2117, DOI: 10.1063/1.1733941.

(157) Brown, C.; Overend, J. *Spectrochimica Acta Part A: Molecular Spectroscopy* **1969**, *25*, 1535–1546, DOI: 10.1016/0584-8539(69)80137-6.

(158) Vanderryn, J. *The Journal of Chemical Physics* **1959**, *30*, 331–332, DOI: 10.1063/1.1729915.

(159) Rajput, N. N.; Seguin, T. J.; Wood, B. M.; Qu, X.; Persson, K. A. *Topics in Current Chemistry* **2018**, *376*, 19, DOI: 10.1007/s41061-018-0195-2.

(160) Liepinya, D.; Smeu, M. *Energy Material Advances* **2021**, *2021*, 1–13, DOI: 10.34133/2021/9769347.

(161) Chen, Z.; Amine, K. *Journal of The Electrochemical Society* **2006**, *153*, A1221, DOI: 10.1149/1.2194633.

(162) Anderson, T. F.; Lassettre, E. N.; Yost, D. M. *The Journal of Chemical Physics* **1936**, *4*, 703–707, DOI: 10.1063/1.1749772.

(163) Watson, J. K. *Journal of Molecular Spectroscopy* **1972**, *41*, 229–230, DOI: 10.1016/0022-2852(72)90136-1.

(164) Stuart, B. H., *Infrared spectroscopy : fundamentals and applications*; John Wiley & Sons, Ltd: 2004.

(165) Yuan, X.; Mayanovic, R. A. *Applied Spectroscopy* **2017**, *71*, 2325–2338, DOI: 10.1177/0003702817721527.

(166) Blümich, B., *Essential NMR : for Scientists and Engineers*; Springer: 2005, pp 15–55, DOI: 10.1007/b138660.

(167) Fulmer, G. R.; Miller, A. J. M.; Sherden, N. H.; Gottlieb, H. E.; Nudelman, A.; Stoltz, B. M.; Bercaw, J. E.; Goldberg, K. I. *Organometallics* **2010**, *29*, 2176–2179, DOI: 10.1021/om100106e.

(168) Egerton, R. F. *Reports on Progress in Physics* **2009**, *72*, 016502, DOI: 10.1088/0034-4885/72/1/016502.

(169) Egerton, R., *Electron Energy-Loss Spectroscopy in the Electron Microscope*, Second Edi; Springer US: 1996, p 485, DOI: 10.1007/978-1-4419-9583-4.

(170) Bendersky, L.; Gayle, F. *Journal of Research of the National Institute of Standards and Technology* **2001**, *106*, 997, DOI: 10.6028/jres.106.051.

(171) He, K. In *Reference Module in Earth Systems and Environmental Sciences*; Elsevier: 2021, DOI: https://doi.org/10.1016/B978-0-12-819723-3.00084-6.

(172) Dupont, L.; Laffont, L.; Grugeon, S.; Laruelle, S.; Bodenez, V.; Tarascon, J.-M. *ECS Transactions* **2007**, *3*, 139–153, DOI: 10.1149/1.2793588.

(173) Clark, R. C.; Reid, J. S. *Acta Crystallographica Section A Foundations of Crystallography* **1995**, *51*, 887–897, DOI: 10.1107/S0108767395007367.

(174) Sheldrick, G. M. *Acta Crystallographica Section C Structural Chemistry* **2015**, *71*, 3–8, DOI: 10.1107/S2053229614024218.

(175) Dolomanov, O. V.; Bourhis, L. J.; Gildea, R. J.; Howard, J. A. K.; Puschmann, H. *Journal of Applied Crystallography* **2009**, *42*, 339–341, DOI: 10.1107/S0021889808042726.

(176) Gross, J. H., *Mass Spectrometry*; Springer International Publishing: 2017, DOI: 10.1007/978-3-319-54398-7.

(177) Bruttel, P.; Schlink, R., *Water Determination by Karl Fischer Titration*; Metrohm Ltd.: 2003.

(178) Dugas, R.; Forero-Saboya, J. D.; Ponrouch, A. *Chemistry of Materials* **2019**, *31*, 8613–8628, DOI: 10.1021/acs.chemmater.9b02776.

(179) Westman, K.; Dugas, R.; Jankowski, P.; Wieczorek, W.; Gachot, G.; Morcrette, M.; Irisarri, E.; Ponrouch, A.; Palacín, M. R.; Tarascon, J.-M.; Johansson, P. *ACS Applied Energy Materials* **2018**, *1*, 2671–2680, DOI: 10.1021/acsaem.8b00360.

(180) Ciobanu, M.; Wilburn, J. P.; Buss, N. I.; Ditavong, P.; Lowy, D. A. *Electroanalysis* **2002**, *14*, 989, DOI: 10.1002/1521-4109(200208)14:14<989::AID-ELAN989>3.0.CO;2-6.

(181) Ciobanu, M.; Wilburn, J. P.; Lowy, D. A. *Electroanalysis* **2004**, *16*, 1351–1358, DOI: 10.1002/elan.200302960.

(182) Mei, B.-A.; Munteshari, O.; Lau, J.; Dunn, B.; Pilon, L. *The Journal of Physical Chemistry C* **2018**, *122*, 194–206, DOI: 10.1021/acs.jpcc.7b10582.

(183) Ciucci, F. *Current Opinion in Electrochemistry* **2019**, *13*, 132–139, DOI: 10.1016/j.coelec.2018.12.003.

(184) Macdonald, D. D.; Sikora, E.; Engelhardt, G. *Electrochimica Acta* **1998**, *43*, 87–107, DOI: 10.1016/S0013-4686(97)00238-7.

(185) Agarwal, P.; Orazem, M. E.; Garcia-Rubio, L. H. *Journal of The Electrochemical Society* **1995**, *142*, 4159–4168, DOI: 10.1149/1.2048479.

(186) Hubbard, R.; Brown, G. *Industrial & Engineering Chemistry Analytical Edition* **1943**, *15*, 212–218, DOI: 10.1021/i560115a018.

A

Rietveld refinement of powder XRD data

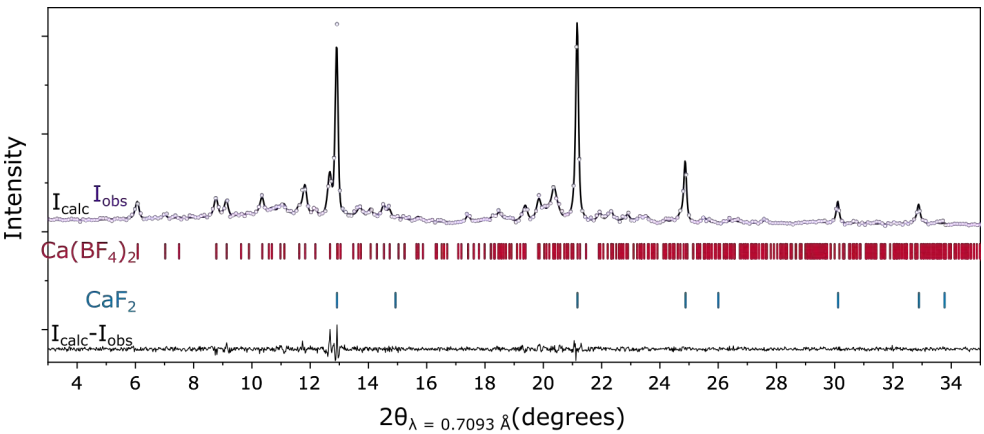

The purity of the $Ca(BF_4)_2$ salt produced by the anhydrous Synthesis A (see section 2.2.1 was estimated by fitting the obtained XRD powder pattern by a Rietveld refinement method using the two phases expected in the mixture: Phase 1 was $Ca(BF_4)_2$ with space group P_{bca}, and Phase 2 was CaF_2 with space group F_{m-3m}. The obtained parameters after refinement are:

Phase 1:

Name	x	y	z	occ.	Mult
Ca1	0.03442(147)	0.21571(197)	0.10266(79)	1.000(0)	8
B1	0.28797(775)	0.99751(1403)	0.93761(649)	1.000(0)	8
B2	0.43410(912)	0.24733(986)	0.14726(587)	1.000(0)	8
F1	0.19983(411)	0.09853(365)	0.99613(312)	1.000(0)	8
F2	0.86456(327)	0.41172(457)	0.13054(253)	1.000(0)	8

F3	0.80344(324)	0.09333(423)	0.12627(307)	1.000(0)	8
F4	0.14859(382)	0.42450(388)	0.01853(293)	1.000(0)	8
F5	0.39984(343)	0.47221(368)	0.17596(224)	1.000(0)	8
F6	0.44624(346)	0.28457(412)	0.06159(227)	1.000(0)	8
F7	0.25581(438)	0.27835(395)	0.17531(232)	1.000(0)	8
F8	0.49247(356)	0.26062(513)	0.22332(191)	1.000(0)	8

a	b	c
9.26885(160)	8.91169(158)	13.37312(212)

α	β	γ
90.00000(0)	90.00000(0)	90.00000(0)

Overall Scale Factor:	0.000036557(1650)
Asymmetry parameters:	0.03156(906)
	0.00369(231)
	0.00000(0)
	0.00000(0)
X and Y parameters:	0.48663(9114)
	0.06219(1219)

Phase 2:

Name	x	y	z	occ.	Mult
Ca1	0.00000(0)	0.00000(0)	0.00000(0)	0.021(0)	4
F1	0.25000(0)	0.25000(0)	0.25000(0)	0.042(0)	8

a	b	c
5.46184(52)	5.46184(52)	5.46184(52)

α	β	γ
90.00000(0)	90.00000(0)	90.00000(0)

Overall Scale Factor:	0.000595043(13400)

Asymmetry parameters:	0.04269(1680)
	0.00679(163)
	0.00000(0)
	0.00000(0)
X and Y parameters:	0.43203(3131)
	0.00247(9)

The global weighted χ^2 for the optimization was 1.35, while the weighted average R-factor was 2.83. The Bragg R-Factors, used to determine the weight fraction of each component in the mixture were found as:

Phase 1: $Ca(BF_4)_2$: Bragg R-factor: 3.92 Vol: 1104.634(0.324) Fract(%): 69.52(3.85) Rf-factor= 2.81 ATZ: 1709.498 Brindley: 1.0000

Phase 2: CaF_2: Bragg R-factor: 0.894 Vol: 162.936(0.027) Fract(%): 30.48(1.20) Rf-factor= 0.968 ATZ: 312.207 Brindley: 1.0000

B

Summary of data and structure refinement of scXRD

Compound	$Ca(BF_4)_2(DME)_2$	$Ca(BOB)_2(DME)_2$
Formula	$C_8H_{20}O_4F_8B_2Ca$	$C_{16}H_{20}O_{20}B_2Ca$
F_W	393.94	594.02
T(K)	150(2)	150(2)
Crystal system	Monoclinic	Monoclinic
Space group	$P2_1/n$	$C2/c$
Unit cell dimensions (Å)	$a = 8.78096(5)$	$a = 18.67580(5)$
	$b = 15.60290(9)$	$b = 9.78603(3)$
	$c = 12.69868(8)$	$c = 14.23106(4)$
Unit cell angles (°)	$\alpha = 90$	$\alpha = 90$
	$\beta = 106.9683(7)$	$\beta = 106.9375(3)$
	$\gamma = 90$	$\gamma = 90$
V (Å^3)	1664.086(18)	2488.076(13)
Z	4	4
D_{calc} (g cm^{-3})	1.572	1.586
Radiation type	Cu K_α	Cu K_α
λ (Å)	1.54184	1.54184
Absorption coefficient (mm^{-1})	4.162	3.041
F(000)	808	1224
2θ range (°)	4.614–76.159	4.951–76.150
Index ranges	$-11 \leq h \leq 11$	$-12 \leq h \leq 23$
	$-19 \leq k \leq 19$	$-11 \leq k \leq 10$
	$-15 \leq l \leq 15$	$-17 \leq l \leq 17$
Reflections collected	58775	96705
Independent reflns.	3478	2586
Reflns. with $[I > 2\sigma(I)]$	3427	2583
Data/restrains/parameters	3478/0/289	2586/0/218
Goodness-of-fit on F^2	1.088	1.035
R_1, wR_2 $[I > 2\sigma(I)]$	0.0242, 0.0657	0.0224, 0.0580
R_1, wR_2 (all data)	0.0245, 0.0659	0.0224, 0.0580
Extinction coefficient	0.0054(3)	0.00181(8)
Largest diff. peak and hole (e.Å^{-3})	0.227 and -0.234	0.270 and -0.244

Compound	$BF_3 \cdot EC$
Formula	$C_3H_4BF_3O_3$
M_W	155.87
T(K)	150.00(10)
Crystal system	Orthorhombic
Space group	P_{bca}
Unit cell dimensions (Å)	$a = 9.75295(18)$
	$b = 9.8988(2)$
	$c = 11.4112(2)$
Unit cell angles (°)	$\alpha = 90$
	$\beta = 90$
	$\gamma = 90$
V (Å^3)	1101.67(4)
Z	8
D_{calc} (g cm^{-3})	1.880
Radiation type	Cu K_α
λ (Å)	1.54184
Absorption coefficient (mm^{-1})	1.975
F(000)	624
2θ range (°)	7.3940–75.7310
Index ranges	-9$\leq h \leq$12
	-12$\leq k \leq$12
	-14$\leq l \leq$14
Reflections collected	6594
Independent reflns.	1063
Reflns. with $[I > 2\sigma(I)]$	994
Data/restrains/parameters	1063/0/108
Goodness-of-fit on F^2	1.040
R_1, wR_2 $[I > 2\sigma(I)]$	0.0328, 0.0862
R_1, wR_2 (all data)	0.0344, 0.0876
Extinction coefficient	0.0015(6)
Largest diff. peak and hole (e.Å^{-3})	0.208 and -0.258

C

VTF fitting parameters for viscosity and ionic conductivity of electrolytes in this study

$$\ln\left(\frac{\eta}{\sqrt{T}}\right) = -\ln B + \frac{E_\eta}{T - T_{0,\eta}}$$

		B	E_η		$T_{0,\eta}$
		(x10^{-3} mPa.s $K^{-0.5}$)	(K)	(kJ mol^{-1})	(K)
0.1 M electrolytes in PC	PC pure	1.82 ± 0.15	881.63 ± 38.19	7.33 ± 0.32	96.82 ± 4.72
	$Ca(TFSI)_2$	2.95 ± 0.07	735.12 ± 10.28	6.11 ± 0.08	120.14 ± 1.35
	$Ca(BF_4)_2$	3.43 ± 0.05	665.90 ± 5.25	5.54 ± 0.04	128.76 ± 0.71
	$Ca(Tf)_2$	2.32 ± 0.18	803.87 ± 32.03	6.68 ± 0.26	112.24 ± 4.02
	$Ca(FOD)_2$	2.68 ± 0.15	752.38 ± 22.57	6.25 ± 0.19	115.90 ± 2.99
	$Ca(TMHD)_2^*$	2.37 ± 0.18	770.50 ± 30.74	6.41 ± 0.26	111.02 ± 4.08
	$CaSO_4$	2.93 ± 0.09	738.14 ± 12.09	6.14 ± 0.10	113.21 ± 1.66

$$\ln\left(\frac{\eta}{\sqrt{T}}\right) = -\ln B + \frac{E_\eta}{T - T_{0,\eta}}$$

0.1 M $Ca(TFSI)_2$ electrolytes in:	B ($x10^{-3}$ mPa.s $K^{-0.5}$)	E_η (K)	E_η (kJ mol^{-1})	$T_{0,\eta}$ (K)
PC	2.95 ± 0.07	735.12 ± 10.28	6.11 ± 0.08	120.14 ± 1.35
EC	3.54 ± 0.13	735.03 ± 15.80	6.11 ± 0.13	115.22 ± 2.33
γBL	1.40 ± 0.36	1127.39 ± 144.05	9.37 ± 1.19	49.38 ± 17.11
DMF	1.10 ± 0.03	1067.81 ± 16.43	8.88 ± 0.14	25.68 ± 2.25
THF	1.50 ± 0.19	850.08 ± 68.07	7.07 ± 0.56	32.10 ± 10.84
G1	0.71 ± 0.08	1108.26 ± 74.68	9.21 ± 0.62	8.05 ± 10.02
G2	1.47 ± 0.13	868.61 ± 44.44	7.22 ± 0.37	77.88 ± 6.10
G3	6.49 ± 0.49	452.19 ± 21.87	3.76 ± 0.18	156.09 ± 3.44

$$\ln\left(\frac{\eta}{\sqrt{T}}\right) = -\ln B + \frac{E_\sigma}{T - T_{0,\sigma}}$$

$Ca(TFSI)_2$ electrolytes in PC		B	E_η		$T_{0,\eta}$
		(x10^{-3} mPa.s $K^{-0.5}$)	(K)	(kJ mol^{-1})	(K)
	0.10 M	2.95 ± 0.07	735.12 ± 10.28	6.11 ± 0.08	120.14 ± 1.35
	0.27 M	347.56 ± 23.52	793.29 ± 27.05	6.59 ± 0.22	118.85 ± 3.35
	0.42 M	326.26 ± 41.36	793.68 ± 47.68	6.59 ± 0.39	131.09 ± 5.52
	0.57 M	281.62 ± 15.99	792.94 ± 20.43	6.59 ± 0.17	138.15 ± 2.27
	0.70 M	238.31 ± 5.09	782.29 ± 7.42	6.50 ± 0.06	150.29 ± 0.81
	1.20 M	117.67 ± 7.19	773.09 ± 16.26	6.42 ± 0.13	183.26 ± 1.35
	1.50 M	79.91 ± 8.65	802.36 ± 26.63	6.67 ± 0.22	196.47 ± 1.96

$$\ln\left(\sigma\sqrt{T}\right) = \ln A + \frac{E_\sigma}{T - T_{0,\sigma}}$$

$Ca(TFSI)_2$ electrolytes in PC	A ($x10^{-3}$ S $K^{0.5}$ cm^{-1})	E_σ (K)	E_σ (kJ mol^{-1})	$T_{0,\sigma}$ (K)
0.10 M	2.85 ± 0.26	708.2 ± 39.4	5.9 ± 0.3	118.3 ± 5.3
0.27 M	3.32 ± 0.53	605.8 ± 59.2	5.04 ± 0.49	135.1 ± 8.8
0.42 M	3.52 ± 0.65	532.9 ± 62.3	4.43 ± 0.51	151.7 ± 9.5
0.57 M	2.74 ± 0.35	416.5 ± 39.3	3.46 ± 0.30	176.8 ± 5.9
0.70 M	3.72 ± 0.57	484.9 ± 44.6	4.03 ± 0.37	172.4 ± 6.4
1.20 M	6.61 ± 1.05	773.2 ± 46.8	6.42 ± 0.39	170.2 ± 4.3
1.50 M	4.56 ± 0.88	793.8 ± 50.4	6.60 ± 0.42	187.3 ± 3.9

$$\ln\left(\sigma\sqrt{T}\right) = \ln A + \frac{E_\sigma}{T - T_{0,\sigma}}$$

$Mg(TFSI)_2$ electrolytes in PC	A ($x10^{-3}$ S $K^{0.5}$ cm^{-1})	E_σ (K)	E_σ (kJ mol^{-1})	$T_{0,\sigma}$ (K)
0.10 M	1.25 ± 0.05	654.4 ± 16.1	5.44 ± 0.13	123.0 ± 2.2
0.30 M	2.78 ± 0.04	527.6 ± 4.4	4.38 ± 0.04	146.8 ± 0.6
0.50 M	3.59 ± 0.05	519.9 ± 4.4	4.32 ± 0.04	157.5 ± 0.6
0.70 M	4.10 ± 0.09	537.1 ± 6.5	4.46 ± 0.05	159.5 ± 0.8
0.90 M	4.49 ± 0.09	536.3 ± 5.7	4.46 ± 0.05	170.7 ± 0.6
1.20 M	4.68 ± 0.09	581.3 ± 4.8	4.83 ± 0.04	179.2 ± 0.5
1.50 M	4.52 ± 0.12	671.9 ± 6.1	5.59 ± 0.05	188.7 ± 0.4

$$\ln\left(\sigma\sqrt{T}\right) = \ln A + \frac{E_\sigma}{T - T_{0,\sigma}}$$

LiTFSI electrolytes in PC	A ($\times 10^{-3}$ S K$^{0.5}$ cm^{-1})	E_σ (K)	E_σ (kJ mol^{-1})	$T_{0,\sigma}$ (K)
0.10 M	0.93 ± 0.03	634.8 ± 10.3	5.28 ± 0.08	125.6 ± 1.4
0.30 M	2.23 ± 0.06	616.4 ± 9.6	5.12 ± 0.08	130.8 ± 1.3
0.50 M	2.98 ± 0.07	561.5 ± 8.0	4.67 ± 0.06	142.2 ± 1.1
0.70 M	3.59 ± 0.13	590.1 ± 11.9	4.91 ± 0.09	139.9 ± 1.6
0.90 M	3.44 ± 0.07	546.7 ± 6.5	4.55 ± 0.05	152.6 ± 0.9
1.20 M	3.94 ± 0.08	568.8 ± 6.6	4.73 ± 0.05	154.9 ± 0.8
1.50 M	4.25 ± 0.09	576.6 ± 6.2	4.79 ± 0.05	162.2 ± 0.7

D

Annex 4 - IR spectra

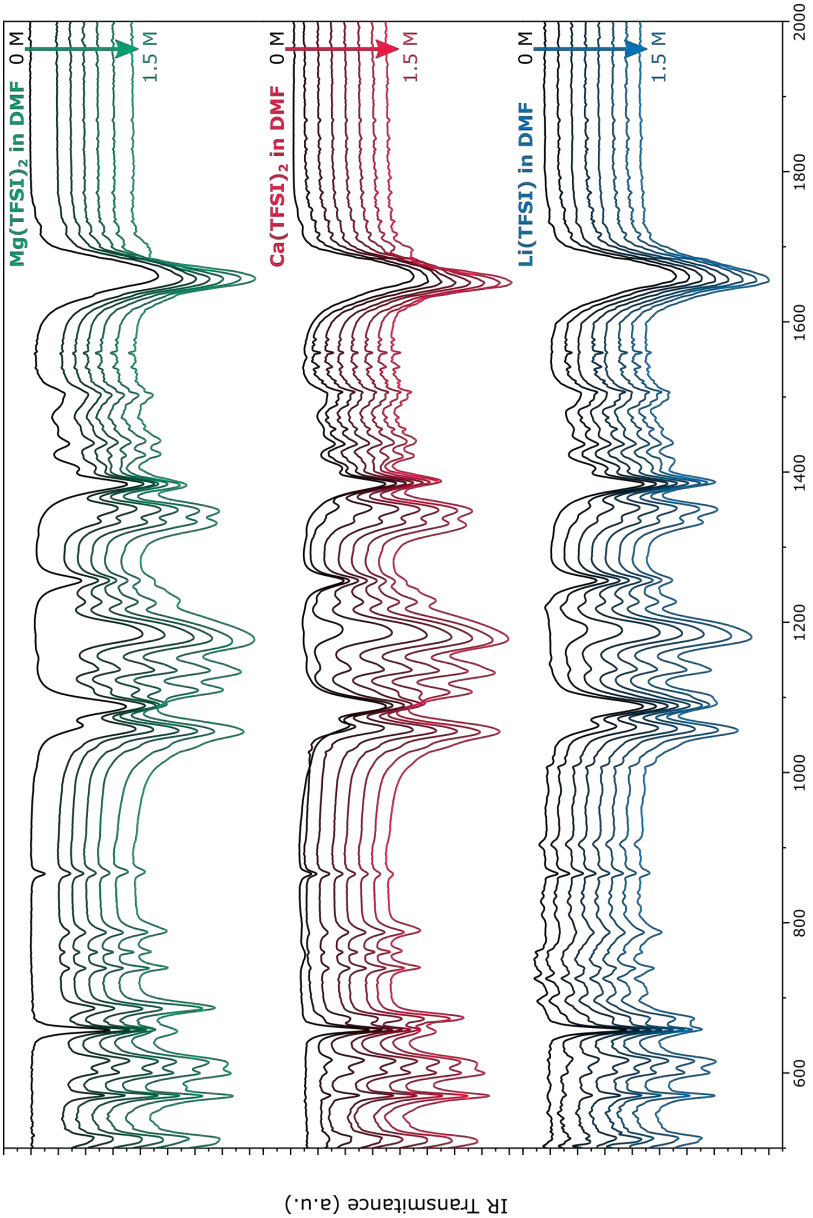

Figure: IR spectra of $Mg(TFSI)_2$, $Ca(TFSI)_2$ and LiTFSI electrolytes in DMF, with salt concentration ranging from 0-1.5 M

E

Annex 5 - Binding energy (eV) and atomic percentage (%) of the components observed in XPS spectra

Binding energy (eV) and atomic percentage (%) of the passivation layers formed over Ca and Mg electrodes in different electrolytes (0.45 M $Ca(TFSI)_2$ in EC:PC, 0.45 M $Ca(BF_4)_2$ in EC:PC, and 0.45 M $Mg(TFSI)_2$ in EC:PC). The surface layers were prepared by polarizing Ca or Mg metallic electrodes for 48 h at -1.4 V *vs.* Ca or Mg metal RE, accordingly. After polarization, the metal WE was taken from the Swagelok cell, rinsed with dimethylcarbonate (DMC) and dried under vacuum before transferring to the XPS chamber.

Peak	$Ca(TFSI)_2$		$Ca(BF_4)_2$		$Mg(TFSI)_2$		Chemical attribution
	BE (eV)	%	BE (eV)	%	BE (eV)	%	
C 1s	285.0	7.2	284.8	20.9	285.0	7.5	C−C, C−H
	286.7	5.6	286.4	11.4	286.7	3.6	C−O
	–	–	287.7	2.5	–	–	C=O
	288.4	2.7	–	–	289.4	2.9	C(=O)−O
	290.0	6.7	290.6	1.6	290.3	3.5	$CaCO_3$ or $MgCO_3$
	293.1	2.2	–	–	293.1	2.0	TFSI
O 1s	531.7	47.2	531.8	32.9	532.5	38.3	unresolved oxygen species

Ca $2p_{3/2}$	347.5	24.2	–	–	–	–	$CaCO_3$ + CaO (+ CaF_2 + $Ca(TFSI)_2$)
	–	–	348.0	6.9	–	–	CaF_2 + $CaCO_3$
Mg 2p	–	–	–	–	49.4	7.7	Mg metal
	–	–	–	–	50.9	26.7	other Mg species
F 1s	684.7	1.6	648.6	10.2	685.5	3.8	CaF_2 or MgF_2
	688.6	2.2	–	–	688.8	3.9	TFSI
N 1s	399.2	0.5	–	–	n.d.[a]	n.d.[a]	TFSI
S $2p_{3/2}$	169.0	2.0	–	–	169.4	2.2	TFSI
B 1s	–	–	191.9	13.6	–	–	borate environment

[a] not detected due to Mg Auger tail